

UNIVERSIDADE DE BRASÍLIA



MAGNETIC IONS-DOPED ZnO NANOCRYSTALS:
STUDY OF THE STRUCTURAL, ELECTRONIC, OPTICAL
AND MAGNETIC PROPERTIES

JESÚS ERNESTO RAMOS IBARRA

BRASÍLIA - D.F.
SEPTEMBER 2018

UNIVERSIDADE DE BRASÍLIA



PH.D. THESIS

MAGNETIC IONS-DOPED ZnO NANOCRYSTALS:
STUDY OF THE STRUCTURAL, ELECTRONIC, OPTICAL
AND MAGNETIC PROPERTIES

JESÚS ERNESTO RAMOS IBARRA

A DISSERTATION SUBMITTED AT THE UNIVERSITY OF BRASÍLIA
IN PARTIAL FULFILLMENT OF THE REQUIREMENTS FOR THE DEGREE OF
DOCTOR OF PHILOSOPHY
(EXPERIMENTAL PHYSICS)

BRASÍLIA - D.F.
SEPTEMBER 2018

**“MAGNETIC IONS-DOPED ZNO NANOCRYSTALS:
STUDY OF THE STRUCTURAL, ELECTRONIC,
OPTICAL AND MAGNETIC PROPERTIES.”**

Por

JESÚS ERNESTO RAMOS IBARRA.

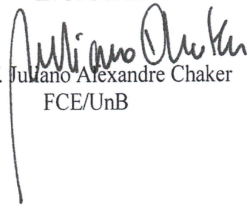
Tese submetida ao Instituto de Física da Universidade de Brasília como parte dos requisitos para a obtenção do grau de Doutor em Física.

Aprovada por:


Prof. José Antonio Huamani Coaquira
IF/UnB


Prof. Ricardo Gargano
IF/UnB


Prof. Márcio Daldin Teodoro
IF/UFSCAR


Prof. Juliano Alexandre Chaker
FCE/UnB

Prof. Dr. Geraldo Magela e Silva
Coordenador de Pós-Graduação
Instituto de Física

Ficha catalográfica elaborada automaticamente,
com os dados fornecidos pelo(a) autor(a)

Rm Ramos Ibarra, Jesús Ernesto
Magnetic ions-doped ZnO Nanocrystals: study of the
structural, electronic, optical and magnetic properties /
Jesús Ernesto Ramos Ibarra; orientador José Antonio Huamani
Coaquira. -- Brasília, 2018.
107 p.

Tese (Doutorado - Doutorado em Física) -- Universidade de
Brasília, 2018.

1. Zinc oxide. 2. Nanocrystals. 3. XPS. 4. XANES. 5.
EXAFS. I. Huamani Coaquira, José Antonio , orient. II. Título.

*To my dearest family for their endless love and,
in loving memory of my grandparents and my
dad...*

Acknowledgements

First all, I would like to express my gratitude to Dr. José A. H. Coaquira for his unfailing guidance, support, and patience over the past years. I have enjoyed working under his supervision and been guided to this point by his unwavering enthusiasm for the work.

I would like to express my appreciation and special recognition to Dr. Marcelo Sousa for his collaboration and support during the synthesis stage; to Dr. Santiago Figueroa at the Brazilian Synchrotron Light Laboratory (LNLS)—he taught me about X-ray absorption and gave me insightful comments and suggestions about my research during my stay at the LNLS and; to Dr. Marcio Daldin at The Federal University of São Carlos for allowing the use of the equipment of his laboratory.

I am also very grateful to the technical staff of the XAFS1 and XAFS2 beamlines and the chemistry laboratory staff at the LNLS for the support and commitment during the measurements.

I would like to thank Dr. Leticia Coelho and Dr. Geraldo da Silva who participated in the initial proposals to request beamtime; and to my colleagues, technicians, and the institute members of the University of Brasilia as well.

The generous financial support of the Brazilian agencies CAPES, FAPDF and CNPEM are gratefully acknowledged and,

Finally, the most important thanks of all go to my family, mum (Yolanda), my brothers and my uncles for all the encouragement they gave me and, especially, to my beautiful wife (Marly) and my son (Martín) for all their love and valuable support given to finish this thesis.

Abstract

As a consequence of the general miniaturization of devices, nanocrystalline materials have attracted a great deal of attention from researchers in various areas to study finite-size and surface effects. These effects yield new physical phenomena and enhanced properties with respect to their bulk counterpart. Among these materials, Zinc Oxide (ZnO) nanocrystals (NCs) have been one of the most intensively studied owing to the low processing temperature and full compatibility with the large scale integrated circuit fabrication. ZnO NCs are recognized as a promising material for applications in spintronics and to improving nanoscale optoelectronic devices, such as bandgap engineered solar cells, organic light emitting diodes, ultraviolet laser diodes, etc. From the fundamental point of view, the involvement of nanoscale effects has allowed further understanding and improvement of the properties of advanced magnetic and optical materials. Because of the intense focus on this material, the ZnO literature is vast and often contradictory; nevertheless, nowadays, the X-ray absorption techniques (i.e., XANES and EXAFS) available around the world are being used to decipher the real origin of the different structural properties; and optical and magnetic interactions in ZnO-based compounds. Due to the high selectivity on the absorber atom and their dependence on the local structure of the studied ions these techniques can offer valuable information.

In the present doctoral thesis, we have synthesized and performed a detailed study of Ni-, Co-, and Tb-doped ZnO NCs obtained via the sol-gel method. The NCs were characterized by conventional macroscopic techniques, such as X-ray diffraction (XRD), high-resolution transmission microscopy (HRTEM), X-ray photoelectron spectroscopy (XPS), photoluminescence (PL), electronic paramagnetic resonance (EPR), SQUID-based magnetometry; and element-specific advanced tools, such as X-ray absorption near-edge spectroscopy (XANES) and X-ray absorption fine structure (XAFS). Detailed analysis of the XRD patterns and HRTEM images indicate the formation of pure and doped ZnO NCs in the wurtzite structure, with circular- and elliptical-like shapes, and changes in the structural parameters with the dopant content—in consistency with the EXAFS data analysis. The experimental EXAFS signal measured at the Co K-edge showed features consistent with those displayed by the Zn K-edge of pure ZnO NCs providing clear evidence that Co ions are present in tetrahedral coordina-

tion. The EXAFS results at the Ni K- and Tb L3-edge suggest the modification of the Ni and Tb local environment in comparison to that observed for Zn and Co sites. Besides, XPS and XANES results indicated that Co and Ni ions assume predominantly the 2+ valence state and are mostly located in tetrahedral and octahedral sites, respectively. These results are in agreement with the analysis of EPR spectra and—in the case of Co—with the PL measurements, which exhibit a red emission band related to the internal transition of Co^{2+} ions in a tetrahedral crystal field. For Tb-doping was determined a mixed-valence state (3+/4+) and the PL measurements provided additional well-resolve narrow emissions characteristic of intra-ionic transitions of Tb^{3+} ions. The correlation of PL and EPR techniques permitted us to suggest that the electron trapped in an oxygen vacancy participate in the green emission of Co-doped ZnO samples. Finally, the magnetic measurements confirm the results obtained from the other techniques indicating that the magnetic moments are consistent with the presence of Co^{2+} , Ni^{2+} , and $\text{Tb}^{3+}/\text{Tb}^{4+}$ ions in the Co-, Ni-, and Tb-doped ZnO NCs, respectively. Moreover, the negative values of the Curie temperature (θ) determined for samples doped with Co and Tb indicate the occurrence of local antiferromagnetic interactions and the positive θ values in the Ni-doped samples suggests the occurrence of local ferromagnetic interactions.

Keywords: Zinc oxide, sol-gel, nanocrystals, intrinsic defects, magnetic properties, XPS, XANES, EXAFS.

Resumo

Como consequência da miniaturização geral dos dispositivos, os materiais nanocristalinos atraíram muita atenção de pesquisadores em várias áreas para estudar o tamanho finito e os efeitos de superfície. Estes efeitos geram novos fenômenos físicos e propriedades aprimoradas em relação à sua forma em "bulk". Entre esses materiais, os nanocristais (NCs) de óxido de zinco (ZnO) têm sido um dos mais intensamente estudados devido à baixa temperatura de processamento e total compatibilidade com a fabricação de circuitos integrados de larga escala. Os NCs de ZnO são reconhecidos como um material promissor para aplicações em spintrônica e para melhorar os dispositivos optoeletrônicos em nanoescala, tais como células solares, diodos emissores de luz orgânicos, diodos laser ultravioleta, etc. Desde o ponto de vista fundamental, o envolvimento dos efeitos em nanoescala permitiu maior compreensão e melhoria das propriedades dos materiais magnéticos e ópticos avançados. Devido ao intenso foco neste material, a literatura do ZnO é vasta e muitas vezes contraditória; no entanto, hoje em dia, as técnicas de absorção de raios-X (i.e., XANES e EXAFS) disponíveis em todo o mundo são usadas para decifrar a verdadeira origem das diferentes propriedades estruturais; e interações ópticas e magnéticas em compostos a base de ZnO. Devido à alta seletividade no átomo absorvedor e sua dependência da estrutura local dos íons estudados, essas técnicas podem oferecer informações valiosas.

Na presente tese de doutorado, foram sintetizados NCs de ZnO dopado com Ni, Co, e Tb, obtidos através do método sol-gel e caracterizados por técnicas convencionais, tais como difração de raios-X (XRD), microscopia de transmissão de alta resolução (HRTEM), espectroscopia fotoeletrônica de raios-X (XPS), fotoluminescência (PL), ressonância paramagnética eletrônica (EPR) e magnetometria baseada em SQUID; e técnicas avançadas com seletividade atômica, tais como espectroscopia de estrutura de absorção de raios-X próxima à borda (XANES) e espectroscopia da estrutura fina de absorção de raios-X estendida (XAFS). Análise detalhada dos padrões de XRD e imagens HRTEM indicam a formação de NCs de ZnO puro e dopado na estrutura wurtzita, com formas circulares e elípticas, e mudanças nos parâmetros de rede conforme o teor de dopante—em consistência com a análise de dados EXAFS. O sinal EXAFS medido na borda K do Co mostrou características consistentes com aquelas mostradas pela borda K do Zn nos NCs puros de ZnO, fornecendo evidência clara de

que o Co apresenta uma coordenação tetraédrica. Os resultados do EXAFS na borda K do Ni e na borda L3 do Tb sugerem a modificação do ambiente local do Ni e Tb em comparação àquele observado para os sítios de Zn e Co. Além disso, os resultados de XPS e XANES indicaram que o Co e Ni assumem predominantemente o estado de valência 2+ e estão localizados principalmente em sítios tetraédricos e octaédricos, respectivamente. Estes resultados estão de acordo com a análise dos espectros de EPR e—no caso do Co—com as medições de PL que exibem uma banda de emissão no vermelho relacionada com a transição interna dos íons Co^{2+} em um campo de cristal tetraédrico. Para a dopagem com Tb foi determinado um estado de valência mista (3+/4+) e as medições de PL forneceram emissões estreitas de resolução bem definida características de transições intra-iônicas dos íons Tb^{3+} . A correlação das técnicas de PL e EPR nos permitiu sugerir que o elétron preso em uma vacância de oxigênio participa na emissão no verde de amostras de ZnO dopadas com Co. Finalmente, as medições magnéticas confirmam os resultados obtidos com as outras técnicas, indicando que os momentos magnéticos são consistentes com a presença de íons Co^{2+} , Ni^{2+} e $\text{Tb}^{3+}/\text{Tb}^{4+}$ nos NCs de ZnO dopados com Co, Ni e Tb, respectivamente. Além disso, os valores negativos da temperatura de Curie (θ) determinados para as amostras dopadas com Co e Tb indicaram a ocorrência de interações locais antiferromagnéticas e os valores positivos de θ nas amostras dopadas com Ni indicaram a ocorrência de interações locais ferromagnéticas.

Palavras-chave: Óxido de zinco, sol-gel, nanocristais, defeitos intrínsecos, propriedades magnéticas, XPS, XANES, EXAFS.

Contents

Abstract	vii
Resumo	ix
1 Introduction	1
1.1 What We Cover in this Thesis	1
1.2 Thesis Structure	2
2 General Background	3
2.1 Properties of Zinc Oxide and its Applications	3
2.2 Transition Metal and Rare Earth Dopant Ions	6
2.3 Intrinsic Defects of Zinc Oxide	8
References	9
3 Synthesis and Experimental Techniques	13
3.1 Synthesis of ZnO Nanocrystals	13
3.1.1 Synthesis—The Sol-Gel Process	13
3.1.2 Preparation of the Precursor and Ethanolic Base	15
3.1.3 Samples Preparation	15
3.2 Structural Characterization	16
3.2.1 X-ray Diffraction	16
3.2.2 Transmission Electron Microscopy	17
3.2.3 X-ray Photoelectron Spectroscopy	18
3.3 X-ray Absorption Spectroscopy Using Synchrotron Radiation	19
3.3.1 XAFS1 and XAFS2 Beamlines at the LNLS	21
3.4 Photoluminescence Measurements	23
3.5 Electron Paramagnetic Resonance	24
3.6 SQUID-Based Magnetometry	24
References	26
4 Structural and Local Structural Properties of doped ZnO Nanocrystals	28
4.1 X-ray Diffraction Analysis	28
4.2 Microscopy Measurements	33

4.3	EXAFS Measurements	38
4.3.1	Zn K-edge Results	38
4.3.2	Ni K-, Co K-, and Tb L3-edge Results	40
	References	44
5	Electronic Structure—XPS and XANES Results	46
5.1	X-ray Photoelectron Spectroscopy	46
5.1.1	Survey Spectra	46
5.1.2	Zn2p Core-level	48
5.1.3	Ni2p and Co2p Core-levels	50
5.1.4	Tb 3d and 4d Core-levels	55
5.1.5	O1s Core-level	58
5.1.6	XPS Concentrations	59
5.2	XANES Measurements	60
5.2.1	Co K-edge Results	60
5.2.2	Ni K-edge Results	62
5.2.3	Tb L3-edge Results	63
	References	65
6	Point Defects and Emission Properties of Doped ZnO Nanocrystals	68
6.1	EPR study of the defects-related region	68
6.2	Photoluminescence Results	71
	References	77
7	Magnetic Properties of Doped ZnO Nanocrystals	79
7.1	Doping effects on EPR response	79
7.2	Magnetization as a Function of the Temperature	82
7.3	Magnetization as a Function of the Applied Magnetic Field	88
	References	94
8	Conclusions and Future Work	98
8.1	Conclusions	98
8.2	Future Work	100
Appendix A		101

List of Figures

2.1	Representation of the ZnO crystal structures: cubic rocksalt (RS), cubic zinc-blende (ZB), and hexagonal wurtzite (W). The yellow and blue spheres indicate the Zn and O ions, respectively.	4
2.2	(Left) The tetrahedral coordination of Zn^{2+} and O^{2-} ions in the wurtzite structure of ZnO and, (right) the tetrahedral and octahedral sites in hexagonal wurtzite structure of ZnO [4]	5
3.1	X-ray absorption spectrum: XANES and EXAFS regions	20
3.2	A typical XAFS station for Transmission and Fluorescence XAFS.	22
3.3	(Left) MPMS magnetometer of the Magnetic Characterization Laboratory of the Institute of Physics at the University of Brasilia and, (right) Schematics of the SQUID-based measurement system [21].	25
4.1	(Left) Rietveld refinement of the Ni-doped ZnO NCs and, (right) graphical behaviour of the structural parameters.	29
4.2	(Left) Rietveld refinement of the Co-doped ZnO NCs and, (right) graphical behaviour of the structural parameters.	30
4.3	(Left) Rietveld refinement of the Tb-doped ZnO NCs and, (right) graphical behaviour of the structural parameters.	31
4.4	(a) TEM (scale bar: 50 nm), (b, c) high-resolution TEM (scale bar: 5 nm) images of pure NCs and, (d) histogram with the fit to obtain the parameters of the sizes distribution.	35
4.5	High-resolution TEM (scale bar: 5 nm) images: (a) ZnO:Ni3 and, (b) ZnO:Ni10 samples.	36
4.6	High-resolution TEM (scale bar: 5 nm) images: (a) ZnO:Co3 and, (b) ZnO:Co10 samples.	36
4.7	(a) TEM (scale bar: 50 nm) and, (b) high-resolution TEM (scale bar: 5 nm) images of ZnO:Tb3 sample.	37
4.8	(a) TEM (scale bar: 50 nm) and, (b) high-resolution TEM (scale bar: 5 nm) images of ZnO:Tb10 sample.	37

4.9	(a) Zn K-edge EXAFS spectra of ZnO NCs and ZnO standard, (b) k^3 -weighted $\chi(k)$ signal and, (c) their respective Fourier transform magnitude spectra.	39
4.10	(a) Zn K-edge EXAFS spectra of Ni-doped ZnO NCs, (b) k^3 -weighted $\chi(k)$ signal and, (c) their respective Fourier transform magnitude spectra.	39
4.11	(a) Zn K-edge EXAFS spectra of Co-doped ZnO NCs, k^3 -weighted $\chi(k)$ signal and, (c) their respective Fourier transform magnitude spectra.	39
4.12	(a) Zn K-edge EXAFS spectra of Tb-doped ZnO NCs, (b) k^3 -weighted $\chi(k)$ signal and, (c) their respective Fourier transform magnitude spectra.	40
4.13	k^3 -weighted $\chi(k)$ signal (top panel) and their Fourier-transformed spectrum (bottom panel) including the real part of $\chi(R)$ for the pure ZnO NCs. Blue dots indicate experimental data and the red solid line is the best-fit curve.	41
4.14	k^3 -weighted $\chi(k)$ signal (top panel) and their Fourier-transformed spectrum (bottom panel) including the real part of $\chi(R)$ for the ZnO:Ni1 sample. Blue dots indicate experimental data and the red solid line is the best-fit curve.	41
4.15	k^3 -weighted $\chi(k)$ signal (top panel) and their Fourier-transformed Spectrum (bottom panel) including the real part of $\chi(R)$ for the ZnO:Co1 sample. Blue dots indicate experimental data and the red solid line is the best-fit curve.	42
4.16	k^3 -weighted $\chi(k)$ signal (top panel) and their Fourier-transformed spectrum (bottom panel) including the real part of $\chi(R)$ for the ZnO:Tb1 sample. Blue dots indicate experimental data and the red solid line is the best-fit curve.	42
4.17	k^2 -weighted $\chi(k)$ signals for the Ni-, Co-, and Tb-doped ZnO NCs at the (a) Ni K-edge, (b) Co K-edge and, (c) Tb L3-edge, respectively. Zn K-edge of pure ZnO is included as a reference.	43
5.1	XPS survey spectra of pure and Ni-, Co-, and Tb-doped ZnO NCs (1 and 10 mol%).	47
5.2	High-resolution XPS spectra of Zn2p core-level for pure and 10 mol% doped ZnO NCs.	48
5.3	High-resolution XPS spectra of Ni2p core-level of 1 and 10 mol% Ni-doped ZnO NCs.	51
5.4	Figure for better visualization of the Ni 2p _{3/2} XPS peak positions reported in the Table 5.2.	52
5.5	High-resolution XPS spectra of Co2p core-level of 1 and 10 mol% Co-doped ZnO NCs.	53
5.6	Figure for better visualization of the Co 2p _{3/2} XPS peak positions reported in the Table 5.3.	54

5.7	High-resolution XPS spectra of Tb3d core-level of 1 and 10 mol% Tb-doped ZnO NCs.	56
5.8	XPS spectrum of Tb4d core-level of ZnO:Tb10 sample.	58
5.9	O1s core-level XPS spectra of pure and doped ZnO NCs.	59
5.10	(a) Co K-edge XANES spectra for Co-doped ZnO NCs and, (b) Co K-edge XANES spectra of ZnO:Co1 sample and some reference compounds.	61
5.11	Pre-edge peak features of (a) 1 mol% Co doped ZnO, (b) CoO (Co ²⁺ , 6-fold coordination) and, (c) CoAl ₂ O ₄ (Co ²⁺ , 4-fold coordination)	62
5.12	(a) Ni K-edge XANES spectra of Ni-doped ZnO NCs and, (b) Ni K-edge XANES spectra of ZnO:Ni1 sample and some reference compounds.	63
5.13	(a) Tb L3-edge XANES spectra of Tb-doped ZnO NCs and, (b) Tb L3-edge XANES spectra of ZnO:Tb1 sample and some reference compounds.	64
5.14	The fit of the Tb L3-edge XANES spectrum of the ZnO:Tb10 sample. For the fit, one arctangent function and two Lorentzian functions (A and B) were used.	64
6.1	100 K EPR spectrum of pure ZnO NCs.	69
6.2	100 K EPR spectra of the defects-related region of ZnO NCs: (a) Pure and 1 mol% Co and Tb-doped samples and, (b) pure and 10 mol% Co and Tb-doped samples.	70
6.3	(a) Room temperature PL spectra of pure ZnO NCs and, (b) PL spectra of pure ZnO NCs obtained at different temperatures. The curves have been displaced on the y-axis for better visualization.	72
6.4	Room temperature PL spectra of 1 and 10 mol% Ni-doped ZnO NCs.	73
6.5	(a) Room temperature PL spectra of Co-doped ZnO NCs (1 and 10 mol%) and, (b) PL spectra of the pure and Co-doped ZnO NCs—for comparison.	74
6.6	(a) Room temperature PL spectra of Tb-doped ZnO NCs (1 and 10 mol%) and, (b) PL spectra of the pure and Co-doped ZnO NCs—for comparison.	76
7.1	100K EPR spectra of Co-doped ZnO NCs.	80
7.2	100K EPR spectra of Ni-doped ZnO NCs.	81
7.3	(Left) DC susceptibility (χ_{DC}) curves as a function of temperature (T) obtained by applying a constant magnetic field of $H = 5$ kOe for the Co-doped ZnO NCs and, (right) Graphical result of the calculated effective magnetic moments.	83
7.4	(Left) DC susceptibility (χ_{DC}) curves as a function of temperature (T) obtained by applying a constant magnetic field of $H = 5$ kOe for the Ni-doped ZnO NCs and, (right) Graphical result of the calculated effective magnetic moments.	83

7.5	(Left) DC susceptibility (χ_{DC}) curves as a function of temperature (T) obtained by applying a constant magnetic field of $H = 5$ kOe for the Tb-doped ZnO NCs and, (right) Graphical result of the calculated effective magnetic moments.	84
7.6	Enlargement of magnetization (M) versus applied magnetic field (H) curve of pure ZnO NCs obtained at 5K.	89
7.7	(Left) Magnetization (M) versus applied magnetic field (H) curve obtained at 300 K for the Co-doped ZnO NCs and, (right) Graphical result of the calculated effective magnetic moments.	89
7.8	(Left) Magnetization (M) versus applied magnetic field (H) curve obtained at 300 K for the Ni-doped ZnO NCs and, (right) Graphical result of the calculated effective magnetic moments.	90
7.9	(Left) Magnetization (M) versus applied magnetic field (H) curve obtained at 300 K for the Tb-doped ZnO NCs and, (right) Graphical result of the calculated effective magnetic moments.	90
7.10	Magnetization (M) versus applied magnetic field (H) curves obtained at 5K for the doped ZnO NCs.	92
7.11	Magnetization (M) versus applied magnetic field (H) curve fitted using the Brillouin function. Dots represent experimental data and straight line the fit result.	93
7.12	Results obtained for ZnO:Co ₃ sample thermal-treated at 400 °C in hydrogen atmosphere: (a) Magnetization versus magnetic applied field curve measured at 300 K, (b) X-ray diffraction patterns, (c) 100 K EPR measurements, and (d, e) HRTEM results.	94
A.1	XANES and EXAFS regions identified. $\mu(E)$ is shown with smooth background function ($\mu_0(E)$) and the edge-step ($\Delta\mu_0(E_0)$).	102
A.2	The different steps for extraction of the oscillatory part from the K absorption spectrum of powder ZnO recorded at XAFS1 beamline at LNLS, (a) raw X-ray absorption data and pre-edge and post edge lines, (b) normalized X-ray absorption data, (c) $\chi(k)$ vs. k data (k-weight = 0) and, (d) EXAFS $\chi(k)$ vs. k data (k-weight = 1, 2 and 3).	106

List of Tables

3.1	Synthesized samples	16
4.1	List of structural parameters of pure and doped ZnO NCs obtained from the XRD patterns refined with the Rietveld method.	32
4.2	List of structural parameters obtained from the EXAFS data analysis for Ni-, Co-, and Tb-doped ZnO NCs.	43
5.1	Summary of the results obtained from the XPS analysis of pure and doped ZnO NCs.	49
5.2	List of XPS peak positions (in eV) obtained for the Ni-doped ZnO NCs. Peak positions of other nickel compounds reported in the literature are included.	52
5.3	List of XPS peak positions (in eV) obtained for the Co-doped ZnO NCs. Peak positions of other cobalt compounds reported in the literature are included.	54
5.4	List of XPS peak positions (in eV) obtained for the Tb-doped ZnO NCs. Peak positions of some other terbium compounds reported in the literature are included for comparison.	57
5.5	Comparison between the nominal and experimental concentrations obtained via XPS measurements.	60
6.1	List of <i>g</i> -factors determined from the EPR spectra in the defects-related region for pure and doped ZnO NCs.	71
6.2	List of photoluminescence emissions determined from the deconvolution of PL spectra of pure and doped ZnO NCs.....	76
7.1	List of calculated <i>g</i> -factors of the different EPR lines in doped ZnO NCs.	82

7.2 List of parameters obtained from the fits of the susceptibility (χ_{DC}) vs. temperature (T) curves to the Curie–Weiss law. C is the Curie constant, μ_{eff} is the effective magnetic moment per dopant ion, θ is the Curie-Weiss temperature, and χ_0 is the temperature-independent susceptibility. The numbers in parentheses represent the estimated uncertainties. 85

7.3 List of parameters obtained from the fits of the magnetization(M) vs. applied magnetic field (H) measured at 300K. C is the Curie constant, μ_{eff} is the effective magnetic moment per dopant ion. The numbers in parentheses represent the uncertainties. 91

Chapter 1

Introduction

1.1 What We Cover in this Thesis

The research on optical and magnetic nanocrystals involves several aspects to consider, from the preparation procedures to the comprehension of the desired properties. Different experimental approaches for a complete characterization of the nanocrystals are fundamental to attain this purpose. Then, in this Ph.D. thesis, we face the study performed on various doped nanocrystals systems where a correlation of the structural, electronic and magnetic characterization methods leads to a better understanding of the nanocrystals properties. In this way, the aim of this Thesis was first to determine the structure and local crystalline structure of the nanocrystals. Then, to determine the oxidation states and coordination numbers and, once that matter is clarified, the experimental study of the modifications on the optical and magnetical properties induced by the doping. To this end, spectroscopic methods such as X-ray photoelectron (XPS), photoluminescence (PL) and electron paramagnetic resonance (EPR); and element-specific advanced tools, i.e., X-ray absorption near-edge spectroscopy (XANES) and extended X-ray absorption fine structure (EXAFS), have been applied in addition to standard characterization tools. EXAFS experiments have been performed at the Zn K-edge in the XAFS1 beamline and XANES experiments have been performed at the Ni K-, Co K-, and Tb L3-edge in the XAFS2 beamline at the Brazilian Synchrotron Light Laboratory (LNLS). These techniques are very useful to provide an atomic and shell-specific description and to examine the electronic state and local structure of the atoms composing the nanocrystals. Moreover, oxidation state, coordination number and some local parameters, which are also key parameters that control the optical and magnetic behavior in materials, may be directly determined by XANES and EXAFS. We intend to use the capabilities of the experimental X-ray absorption techniques for electronic and structural characterization of pure and doped ZnO nanocrystals systems, along with other complementary methods to obtain a well-detailed characterization of the different properties of the nanocrystals.

The fulfillment of the proposed objectives in the project implied, however, the synthesis and characterization of samples by using different experimental techniques. This study was done partially in collaboration with different researchers: Dr. Marcelo

Sousa (Faculty of Ceilândia, University of Brasilia); Dr. Marcio Daldin (Department of Physics, Federal University of São Carlos); Dr. Bożena Sikora (Institute of Physics, Polish Academy of Sciences); Dr. Pedro Rodriguez, Dr. Geraldo Magela, Dr. Letícia Nunes Coelho (Institute of Physics, University of Brasilia); and Dr. Santiago Figueroa (Brazilian Synchrotron Light Laboratory, LNLS) that also participated in some of the synchrotron radiation experiments.

1.2 Thesis Structure

This Thesis is organized as follows: In Chap. 1, an overall introduction and the objectives of the Thesis are included. In Chap. 2, a general background is presented, covering all essential aspects of zinc oxide properties and its applications when doped with Transition Metal and Rare Earth ions. Chap. 3 is devoted to describing the synthesis of the nanocrystals and the experimental techniques used in the present work and the analysis processes performed to study the structural, electronic, optical and magnetic properties of pure and Ni-, Co-, and Tb-doped ZnO nanocrystals (NCs) systems. In particular, we focus on the X-ray absorption spectroscopies that make use of synchrotron radiation. Hence, in Chap. 4, we describe the main structural results obtained from the analysis of X-ray diffraction (XRD), high-resolution transmission electron microscopy (HRTEM) and extended X-ray absorption fine structure (EXAFS) measurements. We demonstrate the formation of ZnO NCs and the evolution of the structural properties with the increase of dopant content. To continue this study, the XPS and XANES experimental results are described together in Chap. 5, in order to have an overall and accurate description of the oxidation states and local environment of the absorbers atoms. There, we analyzed the Ni K-, Co K-, and Tb L3-edge XANES results. Then, via measurements using electron paramagnetic resonance (EPR) and photoluminescence (PL) spectroscopies, we presented in Chap. 6 the study of the point defects and emission properties. Chap. 7 is dedicated to studying the magnetic response of the synthesized nanocrystals. Firstly, EPR measurements are presented and, then, we show the SQUID-based magnetometry results in order to determine the magnetic properties of the samples. Finally, in Chap. 8, we summarized the conclusions and future works related to this research.

Chapter 2

General Background

The purpose of this chapter is to summarize the properties, applications, point defects and some reasonably well-established results on ZnO compounds.

2.1 Properties of Zinc Oxide and its Applications

Zinc oxide (ZnO) is an II-VI inorganic compound semiconductor with a wide bandgap and large exciton binding energy of 60 meV. ZnO crystallizes in three forms (see Fig. 2.1): hexagonal wurtzite (space group: $P6_3mc$; lattice parameters $a = 3.249 \text{ \AA}$ and $c = 5.206 \text{ \AA}$), cubic zinc-blende (space group: $F\bar{4}3m$; lattice parameter $a = 4.47 \text{ \AA}$), and the rarely observed cubic rock salt ($Fm\bar{3}m$; $a = 4.28 \text{ \AA}$). The wurtzite structure is the most stable at ambient conditions whereas the zinc-blende form can be stabilized only by growing ZnO on cubic substrates. In both cases, the zinc and oxygen are tetrahedrally coordinated. Finally, the rocksalt (NaCl-type) structure is only observed at relatively high pressures of about 10 GPa. In the wurtzite structure, each anion is surrounded by four cations at the corners of a tetrahedron and vice versa. A schematic representation of the wurtzite ZnO structure is shown in Fig. 2.2. This tetrahedral coordination is typical of sp^3 covalent bonding nature, but these materials also have a substantial ionic character that tends to increase the bandgap beyond the one expected from the covalent bonding.

As mentioned above, the wurtzite structure has a hexagonal unit cell with lattice parameters $a = 3.296 \text{ \AA}$ and $c = 5.206 \text{ \AA}$ in the ratio of $c/a = \sqrt{8/3} = 1.633$ (in an ideal wurtzite structure) and belongs to the space group $P6_3mc$ in the Hermann–Mauguin notation. The structure is composed of two interpenetrating hexagonal close-packed (hcp) sublattices, each of which consists of one type of atom displaced with respect to each other along the threefold c -axis by the amount of $u = 3/8 = 0.375$ (in an ideal wurtzite structure) in fractional coordinates. The internal parameter u is defined as the length of the bond parallel to the c -axis (anion-cation bond length or the nearest-neighbor distance) divided by the c lattice parameter. The basal plane lattice parameter (the edge length of the basal plane hexagon) is universally depicted by a . The axial

lattice parameter (unit cell height), perpendicular to the basal plane, is universally described by c . Each sublattice includes four atoms per unit cell, and every atom of one kind (an atom of group II) is surrounded by four atoms of the other kind (an atom of group VI), or vice versa, which are coordinated at the edges of a tetrahedron. Because of the tetrahedral coordination of wurtzite and zinc-blende structures, the 4 nearest neighbors and 12 next-nearest neighbors have the same bond distance in both structures [1]. Besides, each ion has twelve next-nearest neighbors of the same type of ions. The Zn–O distance of the nearest neighbors is 1.992 Å in the direction parallel to the c -axis of the hexagonal unit cell and 1.973 Å in the other three directions of the tetrahedral arrangement. The tetrahedral arrangement between the nearest neighbors indicates the covalent bond between the zinc and oxygen atoms. The covalent radii of zinc and oxygen are reported to be 1.31 and 0.66 Å, respectively.

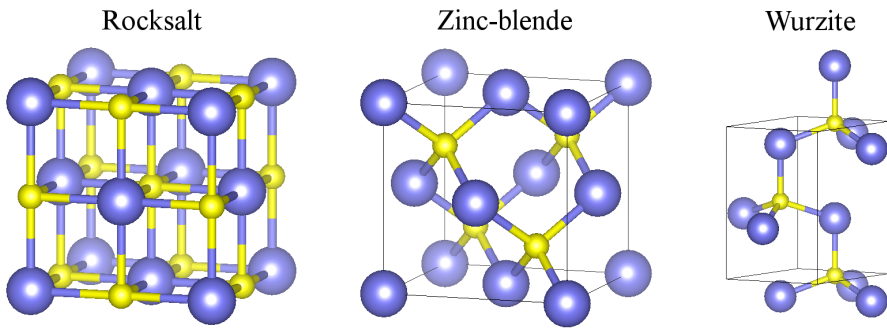


Fig. 2.1 Representation of the ZnO crystal structures: cubic rocksalt (RS), cubic zinc-blende (ZB), and hexagonal wurtzite (W). The yellow and blue spheres indicate the Zn and O ions, respectively.

Another way to describe the structure of ZnO is considering alternating planes composed of tetrahedrally coordinated O^{2-} and Zn^{2+} ions, stacked along the c -axis. In this structure, the oxygen forms a compact hexagonal stacking and zinc occupies half of the tetrahedral sites so that the resulting structure is not very compact; all the octahedral and half of the tetrahedral sites are not occupied which results in an easy incorporation of impurities or dopants in the crystalline lattice of this oxide [2]. The two interstitial sites—the tetrahedrally and the octahedrally coordinated—that exist in the hexagonal (wurtzite) ZnO structure are presented in Fig. 2.2.

The tetrahedral coordination in ZnO results in a noncentrosymmetric structure so that the center of gravity of the positive charges does not coincide with that of the negative charges which give rise to a polar axis and, consequently, to piezoelectric properties. In addition, the change in stoichiometry with the partial pressure of oxygen causes a change in the usual network parameters; at low oxygen pressures, the zinc atoms exceed the stoichiometric value, resulting in the formation of interstitial cations or oxygen vacancies [3]. In this semiconductor the n-type conductivity is a result of the excess of cations in interstitial positions. These characteristics may explain certain

particular ZnO properties, such as the semiconducting phenomena, photoconductivity, luminescence, catalytic and chemical properties.

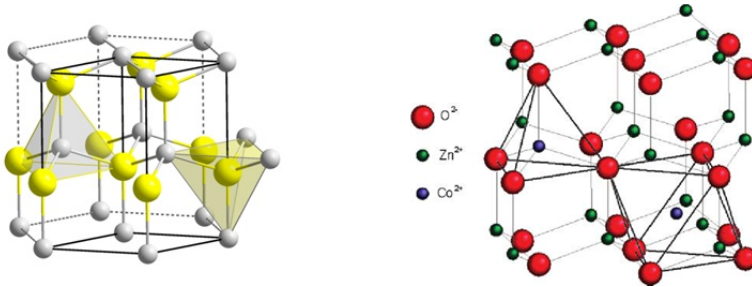


Fig. 2.2 (Left) The tetrahedral coordination of Zn^{2+} and O^{2-} ions in the wurtzite structure of ZnO and, (right) the tetrahedral and octahedral sites in hexagonal wurtzite structure of ZnO [4]

The high exciton binding energy (60 meV) of ZnO makes it a highly efficient photonic material, operable at room temperature [5]. It can also be used in the elaboration of advanced devices due to its high direct band gap (3.37 eV at 300 K [1]) which is much advantageous over indirect bandgap semiconductors as they do not involve a phonon transition to warrant conservation issues and has a major influence on physical properties of the material such as optical absorption, index of refraction, band structure, electrical conductivity and also makes ZnO an efficient emitter. It shows a high transparency for short wavelength applications from blue to UV spectral range and has been widely used in the manufacture of transparent thin film transistors, where a layer of light exposure protection is unnecessary since ZnO-based transistors are insensitive to visible light. The low absorbance of visible light and improved conductivity after doping puts ZnO in the category of the best transparent conducting materials and of great applicability for solar cells, transistors, nanogenerators, diodes, LED's of various colors (green, blue, red and white), UV photodetectors, UV blue laser diodes, flat panel displays, optical waveguides, transparent electrodes, and many more [5]. In addition, the larger surface to volume ratio of nanocrystalline ZnO makes it a good candidate for gas sensing as well as heterogeneous catalysis [6]. 1-D ZnO nanostructures (rods, fibers, tubes, wires, ribbons) are of special interest due to their unique catalytic, electronic, optical, thermal, and photonic properties intrinsically associated with their low dimensionality and quantum confinement effects [7]. Finally, ZnO doped with transition metals and rare earth ions has found applications in spintronics, non-volatile memory devices, optoelectronics, spin light-emitting diodes, sensors and photocatalysts [8].

2.2 Transition Metal and Rare Earth Dopant Ions

The transition metal (TM) elements belong to d-block, sorted under 3-12 of the periodic table with an incomplete d orbital. The exceptions are zinc, cadmium, and mercury, as they have a filled d shell with the electronic configuration of $d^{10}s^2$. Typically 3d electrons have small total magnetic moments per atom due to quenched orbital momentum. These elements behave as paramagnetic (PM) since their filled d sub-shells prevent the d–d bonding [9]. However, their substitution or alloying with other transition metals with incomplete d shell in a crystalline compound may result in different magnetic and optical properties. Thus, intentional transition-metal doping of ZnO with Fe, Co, Ni or other TM was motivated by the possibility of obtaining ferromagnetism at room temperature which finds a wide application in spintronics, magnetic switches, magnetic sensors, and many others. The results are very controversial and depend very much on the synthesis conditions. Numerous publications report that $Zn_{1-x}M_xO$ (where M = transition metal ion and x = dopant concentration) is indeed a ferromagnet at room temperature. At the same time, other publications deny the existence of any long-range ferromagnetic order with increasing frequency. The confusing situation calls for a critical and detailed analysis. Then, the research work on the transition metal ion doped to obtain magnetic properties and understand the spin exchange concept is under developing [7]. Different reports have been presented to study the effects of the TM doping in the ZnO matrix, and thus different magnetic responses have been reported. Anghel et al., correlates the saturation magnetization, bandgap, and lattice volume of $Zn_{1-x}M_xO$ (M = Cr, Mn, Fe, Co, and Ni) nanoparticles synthesized by a chemical process [10]. Balti et al. [11] studied the effect of substitution of Zn^{2+} ions in Ni- and Co-doped ZnO in order to understand correlations between the structural, optical, and magnetic proprieties. In 2006, Benjamin et al. reported the production of anisotropic $Zn_{1-x}M_xO$ nanowires (average nanowire diameter about 35 nm and a length ranging from 80–160 nm) by the thermal decomposition of zinc acetate and dopant acetate in refluxing trioctylamine [12]. The substitution of Co for Zn cations results in complex magnetic behavior that cannot be modeled by a simple coexistence of paramagnetism and ferromagnetism. In 2017, Kumar et al. [13] reported the study of the ferromagnetism in Ni-doped ZnO nanostructures by a systematic correlation among the structural, optical and magnetic properties. Using X-ray absorption spectroscopy they proposed that Ni incorporate into the ZnO wurtzite matrix and shows 2+ oxidation state. Recently, different behaviors have been obtained for Co-doped ZnO samples; Buchner et al. [14] have found pinned antiferromagnetic (AFM) moments giving rise to the magnetization and; Henne et al. [15] and Ney et al., [16] have reported exchange-bias-like effect and coalescence-driven magnetic order of the uncompensated antiferromagnetism in Co-doped ZnO. Careful studies showed that secondary phases were often present in transition-metal-doped ZnO. For example, Kaspar et al. [17] used X-ray absorption fine structure to identify ferromagnetic CoZn phases in ZnO:Co thin films. Techniques such as transmission electron microscopy and synchrotron X-ray spectroscopies have identified secondary phases in transition-metal-doped ZnO and other semiconductors [18]. In summary, it has become clear that the reported ferromagnetism can be caused by a phase-segregated material rather than the

dopant ions immersed in the ZnO structure. Other interesting behaviors that have been explored: catalytic and photocatalytic activities due to the addition of Cu and Mn on ZnO influenced by admixtures on the electronic band structure parameters and also by the alteration of the adsorption ability on the semiconductor surface [19]. Hydrogen sensing applications using Ni-doped ZnO [20] and Pd-doped ZnO nanofibers which exhibit considerable sensitivity, rapid response and good selectivity to a low concentration of carbon monoxide [21] were also reported.

Rare earth (RE) atoms have partially filled f-orbitals which carry high magnetic moments that can be born on a single ion and may take part in the magnetic coupling as in the case of TM with partially filled d-orbitals [22]. Although 4f electrons of RE ions are localized with indirect exchange interactions via 5d or 6s conduction electrons, the high orbital momentum of 4f electrons leads to high total magnetic moments per atom (e.g., $7.94 \mu_B$ for Gd and $9.72 \mu_B$ for Tb). The colossal magnetic moment reported for Gd in GaN [23, 24], which can be explained in terms of a long-range spin polarization of Gd ions in the GaN matrix, have also evoked a great interest in the study of Gd-doped compounds [25–28] and other RE ions used as the dopants. Furthermore, Qi et al. [29] studied the magnetic properties of Er-doped ZnO thin films, prepared by reactive magnetron sputtering, and they reported that Er-doped ZnO thin films are a mixture of ferromagnetic and paramagnetic phases at room temperature. Er ions are in trivalent state and the ferromagnetism in the films is caused by the substitution of Zn^{2+} ions by Er^{3+} ions into ZnO lattice, due to an increase in the number of erbium ions occupying adjacent cation lattice positions, which are antiferromagnetic coupled with each other.

In relation to the optical properties, semiconducting materials doped with RE elements such as La, Nd, Sm, Eu, Er, Tb, and Gd have received great research interest because of their important applications in optoelectronics as emitters in the visible wavelength region [30]. RE doped ZnO is a significant material in optoelectronic devices for an efficient energy transfer from ZnO host to RE ions. There are two main factors leading to the stable and sharp luminescence in RE elements in a semiconductor host: one is that the 4f orbital of RE ions is shielded by the outer 6s, 5p and 5d orbitals, which weakens its coupling with the surrounding ligands yielding a number of discrete energy levels that are only slightly perturbed by the crystal field when compared to the free-ion energy levels [8]; the other is that the f-f transitions are parity forbidden; thus, resulting in small absorption cross-sections, but the initial efforts of incorporating RE ions into Si and other narrow bandgap semiconductors suffered severe limitations due to the solubility constraints and the thermal quenching. On the other hand, RE-doped ZnO compounds have been investigated most intensely because of the unique luminescent properties resulting from its stability and high emission quantum yields [8, 31–34]. According to Yogamalar et al., [7] the doping of ZnO with RE ions is difficult due to large differences in ionic size and charge between the RE dopant ion and Zn^{2+} and; an inappropriate energy level position of RE ion relative to the valence band (VB) and conduction band (CB) of ZnO. However, the growth mechanisms are systematically studied to obtain RE doped ZnO with specific properties using different physical and chemical methods. There are some pioneering works, such as Tb nanoclusters in Tb implanted ZnO single crystals [35], ZnO:Tb nanorod bundles [36]

with superparamagnetism behaviour and Tb doped ZnO nanostructures studied for a new type of green phosphor with interesting photoluminescence properties [36, 37]. In 2014, Kumar et al. [8] studied the effect of the incorporation of Tb^{3+} ions on some properties of ZnO nanophosphors in terms of luminescence and band gap energy. To the best of our knowledge, it is one of the few reports based on ZnO NCs doped with Tb ions, especially, for the study of the optical properties. However, a systematic and well-detailed study of the overall properties using XAFS technique has not been reported for Tb-doped ZnO NCs yet. RE-doped semiconductors are technologically important materials in optoelectric devices [38, 39] and; therefore, it is interesting to investigate the local structure, electronic structure and magnetic properties of Tb-doped ZnO NCs.

2.3 Intrinsic Defects of Zinc Oxide

The intrinsic or native point defects commonly formed in ZnO are zinc interstitials Zn_i , oxygen interstitials O_i , zinc vacancies V_{Zn} , oxygen vacancies V_O , zinc antisites Zn_O and oxygen antisites O_{Zn} . In the hexagonal (wurtzite) ZnO structure exists two different interstitial sites: the tetrahedrally and the octahedrally coordinated sites. In ZnO, the octahedrally coordinated interstitials (i.e., Zn_i and O_i) have lower defect formation energies than the tetrahedrally coordinated interstitials [40].

The dominant native donors are the V_O and Zn_i . The Zn_O defect in ZnO can also be a relevant donor, although its formation energy is always higher than that of Zn_i . However, it is thermally more stable than Zn_i . So if ZnO is once created by a non-equilibrium process (e.g., irradiation), it is expected to be a donor type. The formation of these donor levels is especially probable if the Fermi energy (FE) is equal to the VB maximum, E_V . The V_O is a deep donor defect (predicted to be 0.5–1 eV below the CB minimum, E_C) and; therefore, do not contribute to the free electron concentration. The main native acceptor in ZnO is the V_{Zn} . Its transition level energy is with 0.11 eV above E_V or 0.8 eV above E_V depending on its transition state. The O_i is a deep acceptor defect and its formation energy is higher than that of V_{Zn} . Among the native point defects of ZnO, O_{Zn} has the highest defect formation energy even for oxygen-rich conditions and it is considered as a deep acceptor [7].

Photoluminescence (PL) spectroscopy has been used for many years to study the emission bands of semiconductors. Undoped ZnO usually presents two emission bands: a short-wavelength band near the fundamental absorption edge and broad long-wavelength band—the maximum of which usually lies in the green spectral range. Red emission bands can be observed when doped ZnO with TM and RE ions [33, 41].

Some authors have suggested that the Zn vacancy can give rise to green luminescence which is one of the ZnO emissions widely debated in the literature. They have calculated the transition level between the -1 and -2 charge states which occurs at 0.9 eV above the VB maximum [42–44], and hence a transition between the CB (or a shallow donor) and the V_{Zn} acceptor level would give rise to luminescence around

2.5 eV. A strong evidence in favor of zinc vacancies being the source of green luminescence has been provided by some experiments [45, 46], which have reported strong passivation of the green luminescence by hydrogen plasma treatment. This observation is consistent with the green luminescence being caused by zinc vacancies, which act as acceptors; these acceptors can be passivated by hydrogen, which acts as a donor [44, 47]. The Zn vacancy is also a likely candidate because it is an acceptor-type defect: acceptor defects are more likely to occur in n-type material, and most ZnO materials to date have exhibited unintentional n-type conductivity [48].

Using electron paramagnetic resonance (EPR) measurements, the four possible centers can be distinguished as follows: (i) Zn_i as an interstitial has the electron configuration ending with $4s^2$, and hence it is diamagnetic. Therefore, it is impossible to detect Zn_i defect centers by EPR. External effects (light, thermal) are required to transfer an electron into the CB of ZnO ($Zn_i^+ + e$). A so-generated paramagnetic Zn_i^+ state can only be detected by EPR when the electronic wave functions of various Zn_i^+ centers do not overlap. (ii) Oxygen on interstitial sites (O_i) has possible electron configurations ending with $2p^4$, $2p^5$ and $2p^6$, giving O_i , O_i^- and O_i^{2-} , respectively. The O_i^{2-} state is diamagnetic and; therefore, cannot be observed by EPR. The O_i state with the $2p^4$ configuration assumes a triplet multiplicity. The O_i^- state with the $2p^5$ electron configuration is a paramagnetic center, which can be easily detected by EPR. On the other hand, the interaction of this paramagnetic defect with other diamagnetic defects of ZnO has to be taken into account [49]. (iii) Oxygen vacancies are intrinsic donors in ZnO and occur in three different charge states: (1) The diamagnetic oxygen vacancy that does not trap any electron with respect to the lattice results in a doubly positively charged vacancy and can be assigned as V_O . It has Zn^{2+} ions in its neighborhood, and there are no unpaired electrons left so that it is diamagnetic. (2) The oxygen vacancy with a trapped electron is designated V_O^\bullet (also referred to as F-centers, such a vacancy tends to absorb light in the visible region, because of that a material that is usually transparent becomes colored). This vacancy results from the reduction by one electron from the CB, so that it is positively charged with respect to the lattice, paramagnetic, and consequently observable by EPR. Because V_O is a very shallow donor [50], it is expected that most oxygen vacancies will be in their paramagnetic V_O^\bullet state under flat band conditions between 294 and 4.3 K [51]. (3) Finally, the vacancy-designed $V_O^{\bullet\bullet}$ is neutral with respect to the lattice and captures two electrons. The $V_O^{\bullet\bullet}$ defect center is diamagnetic if the spins of both electrons captured in the vacancy somehow compensate each other. If they do not, then one may expect the existence of a triplet state, which is EPR active as well but shows significantly broadened signals [51].

References

1. Hadis Morkoç and Ümit Özgür. *Zinc oxide: fundamentals, materials and device technology*. John Wiley & Sons, 2008.
2. Bruno Leonardo Caetano. *Formação e crescimento de nanopartículas de óxido de zinco via sol-gel*. PhD thesis, Universidade Estadual Paulista (UNESP), 2010.

3. Zhe Chuan Feng. *Handbook of zinc oxide and related materials: volume two, devices and nano-engineering*, volume 2. CRC press, 2012.
4. Petra Lommens, Frank Loncke, Philippe F Smet, Freddy Callens, Dirk Poelman, Henk Vrielinck, and Zeger Hens. Dopant incorporation in colloidal quantum dots: a case study on Co²⁺ doped ZnO. *Chem. Mater.*, 19(23):5576–5583, 2007.
5. Moazzam Ali and Markus Winterer. ZnO nanocrystals: surprisingly ‘alive’. *Chem. Mater.*, 22(1):85–91, 2009.
6. Marly Montero-Muñoz, JE Ramos-Ibarra, Jorge E Rodríguez-Páez, Marcio D Teodoro, Gilmar E Marques, Alfonso R Sanabria, Paola C Cajas, Carlos A Páez, Benoît Heinrichs, and Jose AH Coaquira. Role of defects on the enhancement of the photocatalytic response of ZnO nanostructures. *Applied Surface Science*, 448:646–654, 2018.
7. N Rajeswari Yogamalar and A Chandra Bose. Synthesis, dopant study and device fabrication of zinc oxide nanostructures: mini review. *Progress in Nanotechnology and Nanomaterials*, 2(1):1–20, 2013.
8. Vinod Kumar, S Som, Vijay Kumar, Vinay Kumar, OM Ntwaeaborwa, E Coetsee, and HC Swart. Tunable and white emission from ZnO: Tb³⁺ nanophosphors for solid state lighting applications. *Chem Eng J.*, 255:541–552, 2014.
9. Bernard Dennis Cullity and Chad D Graham. *Introduction to magnetic materials*. John Wiley & Sons, 2011.
10. Joshua Anghel, Aaron Thurber, Dmitri A Tenne, Charles B Hanna, and Alex Punnoose. Correlation between saturation magnetization, bandgap, and lattice volume of transition metal (M= Cr, Mn, Fe, Co, or Ni) doped Zn_{1-x}M_xO nanoparticles. *Journal of applied physics*, 107(9):09E314, 2010.
11. Imen Balti, Amine Mezni, Amel Dakhlaoui-Omrani, Philippe Leone, Bruno Viana, Ovidiu Brinza, Leila-Samia Smiri, and Noureddine Jouini. Comparative study of Ni- and Co-substituted ZnO nanoparticles: synthesis, optical, and magnetic properties. *J. Phys. Chem. C*, 115(32):15758–15766, 2011.
12. Benjamin D Yuhas, David O Zitoun, Peter J Pauzaskie, Rongrui He, and Peidong Yang. Transition-metal doped zinc oxide nanowires. *Angew. Chem. Int. Ed.*, 45(3):420–423, 2006.
13. Amit Kumar Rana, Yogendra Kumar, Parasmani Rajput, Shambhu Nath Jha, Dibyendu Bhat-tacharyya, and Parasharam M Shirage. Search for origin of room temperature ferromagnetism properties in Ni-doped ZnO nanostructure. *ACS Appl. Mater. Interfaces*, 9(8):7691–7700, 2017.
14. Martin Buchner, Bastian Henne, Verena Ney, Julia Lumetzberger, Fabrice Wilhelm, Andrei Rogalev, Amir Hen, and Andreas Ney. Pinned orbital moments in uncompensated antiferromagnetic Co-doped ZnO. *J. Appl. Phys.*, 123(20):203905, 2018.
15. Bastian Henne, Verena Ney, Mariano de Souza, and Andreas Ney. Exchange-bias-like effect of an uncompensated antiferromagnet. *Phys. Rev. B*, 93(14):144406, 2016.
16. V Ney, B Henne, J Lumetzberger, F Wilhelm, K Ollefs, A Rogalev, A Kovacs, M Kieschnick, and A Ney. Coalescence-driven magnetic order of the uncompensated antiferromagnetic Co doped ZnO. *Phys. Rev. B*, 94(22):224405, 2016.
17. Tiffany C Kaspar, T Droubay, Steve M Heald, Mark H Engelhard, Ponnusamy Nachimuthu, and Scott A Chambers. Hidden ferromagnetic secondary phases in cobalt-doped ZnO epitaxial thin films. *Physical Review B*, 77(20):201303, 2008.
18. Alberta Bonanni and Tomasz Dietl. A story of high-temperature ferromagnetism in semiconductors. *Chemical Society Reviews*, 39(2):528–539, 2010.
19. B Donkova, D Dimitrov, M Kostadinov, E Mitkova, and D Mehandjiev. Catalytic and photocatalytic activity of lightly doped catalysts M: ZnO (M= Cu, Mn). *Materials Chemistry and Physics*, 123(2-3):563–568, 2010.
20. Vijendra Singh Bhati, Sapana Ranwa, Saravanan Rajamani, Kusum Kumari, Ramesh Raliya, Pratim Biswas, and Mahesh Kumar. Improved Sensitivity with Low Limit of Detection of a Hydrogen Gas Sensor Based on rGO-Loaded Ni-Doped ZnO Nanostructures. *ACS applied materials & interfaces*, 10(13):11116–11124, 2018.
21. Shaohong Wei, Yang Yu, and Meihua Zhou. CO gas sensing of Pd-doped ZnO nanofibers synthesized by electrospinning method. *Materials letters*, 64(21):2284–2286, 2010.

22. Brian G Wybourne and Lidia Smentek. *Optical spectroscopy of lanthanides: magnetic and hyperfine interactions*. CRC press, 2007.
23. S Dhar, O Brandt, M Ramsteiner, VF Sapega, and KH Ploog. Colossal magnetic moment of Gd in GaN. *Phys. Rev. Lett.*, 94(3):037205, 2005.
24. S Dhar, L Pérez, O Brandt, A Trampert, KH Ploog, J Keller, and B Beschoten. Gd-doped GaN: A very dilute ferromagnetic semiconductor with a Curie temperature above 300K. *Phys. Rev. B*, 72(24):245203, 2005.
25. Hongliang Shi, Ping Zhang, Shu-Shen Li, and Jian-Bai Xia. Magnetic coupling properties of rare-earth metals (Gd, Nd) doped ZnO: first-principles calculations. *Journal of Applied Physics*, 106(2):023910, 2009.
26. K Potzger, Shengqiang Zhou, F Eichhorn, M Helm, W Skorupa, A Mücklich, J Fassbender, T Herrmannsdörfer, and A Bianchi. Ferromagnetic Gd-implanted ZnO single crystals. *Journal of applied physics*, 99(6):063906, 2006.
27. AA Dakhel and M El-Hilo. Ferromagnetic nanocrystalline Gd-doped ZnO powder synthesized by coprecipitation. *Journal of Applied Physics*, 107(12):123905, 2010.
28. S Assa Aravindh, Udo Schwingenschloegl, and Iman S Roqan. Ferromagnetism in Gd-doped ZnO nanowires: A first principles study. *Journal of Applied Physics*, 116(23):233906, 2014.
29. Jing Qi, Yinghu Yang, Li Zhang, Junhong Chi, Daqiang Gao, and Desheng Xue. Room-temperature ferromagnetism in Er-doped ZnO thin films. *Scripta Materialia*, 60(5):289–292, 2009.
30. Andrew J Steckl, Jeong Ho Park, and John M Zavada. Prospects for rare earth doped GaN lasers on Si. *Materials Today*, 10(7-8):20–27, 2007.
31. LF Koao, FB Dejene, RE Kroon, and HC Swart. Effect of Eu³⁺ on the structure, morphology and optical properties of flower-like ZnO synthesized using chemical bath deposition. *Journal of Luminescence*, 147:85–89, 2014.
32. LF Koao, FB Dejene, HC Swart, and JR Botha. The effect of Ce³⁺ on structure, morphology and optical properties of flower-like ZnO synthesized using the chemical bath method. *Journal of Luminescence*, 143:463–468, 2013.
33. NH Alvi, Kamran Ul Hasan, Omer Nur, and Magnus Willander. The origin of the red emission in n-ZnO nanotubes/p-GaN white light emitting diodes. *Nanoscale research letters*, 6(1):130, 2011.
34. Vinod Kumar, OM Ntwaeborwa, T Soga, Viresh Dutta, and HC Swart. Rare earth doped zinc oxide nanophosphor powder: a future material for solid state lighting and solar cells. *ACS Photonics*, 4(11):2613–2637, 2017.
35. Shengqiang Zhou, K Potzger, A Mücklich, F Eichhorn, M Helm, W Skorupa, and J Fassbender. Structural and magnetic properties of Tb implanted ZnO single crystals. *Nuclear Instruments and Methods in Physics Research Section B: Beam Interactions with Materials and Atoms*, 266(4):589–593, 2008.
36. Gao-Ren Li, Xi-Hong Lu, Cheng-Yong Su, and Ye-Xiang Tong. Facile synthesis of hierarchical ZnO:Tb³⁺ nanorod bundles and their optical and magnetic properties. *The Journal of Physical Chemistry C*, 112(8):2927–2933, 2008.
37. Shulin Ji, Liangliang Yin, Guodong Liu, Lide Zhang, and Changhui Ye. Synthesis of rare earth ions-doped ZnO nanostructures with efficient host-guest energy transfer. *The Journal of Physical Chemistry C*, 113(37):16439–16444, 2009.
38. MAJ Klik, T Gregorkiewicz, IV Bradley, and JP R Wells. Optically induced deexcitation of rare-earth ions in a semiconductor matrix. *Phys. Rev. Lett.*, 89(22):227401, 2002.
39. Xiaoyan Zeng, Junlin Yuan, Zhenyang Wang, and Li-de Zhang. Nanosheet-Based Microspheres of Eu³⁺-doped ZnO with Efficient Energy Transfer from ZnO to Eu³⁺ at Room Temperature. *Advanced Materials*, 19(24):4510–4514, 2007.
40. Hülya Kaftelen, Kasim Ocakoglu, Ralf Thomann, Suyan Tu, Stefan Weber, and Emre Erdem. EPR and photoluminescence spectroscopy studies on the defect structure of ZnO nanocrystals. *Phys. Rev. B*, 86(1):014113, 2012.
41. Aleksandra B Djurišić and Yu Hang Leung. Optical properties of zno nanostructures. *small*, 2(8-9):944–961, 2006.

42. Donald C Reynolds, David C Look, B Jogai, and H Morkoc. Similarities in the bandedge and deep-centre photoluminescence mechanisms of ZnO and GaN. *Solid State Communications*, 101(9):643–646, 1997.
43. DC Reynolds, DC Look, B Jogai, JE Van Nostrand, R Jones, and J Jenny. Source of the yellow luminescence band in GaN grown by gas-source molecular beam epitaxy and the green luminescence band in single crystal ZnO. *Solid state communications*, 106(10):701–704, 1998.
44. Anderson Janotti and Chris G Van de Walle. Fundamentals of zinc oxide as a semiconductor. *Reports on progress in physics*, 72(12):126501, 2009.
45. Takashi Sekiguchi, Naoki Ohashi, and Yoshihiro Terada. Effect of hydrogenation on ZnO luminescence. *Jpn. J. Appl. Phys.*, 36(3A):L289, 1997.
46. EV Lavrov, J Weber, F Börrnert, Chris G Van de Walle, and R Helbig. Hydrogen-related defects in ZnO studied by infrared absorption spectroscopy. *Phys. Rev. B*, 66(16):165205, 2002.
47. Anderson Janotti and Chris G Van de Walle. Native point defects in ZnO. *Phys. Rev. B*, 76(16):165202, 2007.
48. Jörg Neugebauer and Chris G Van de Walle. Gallium vacancies and the yellow luminescence in GaN. *Appl. Phys. Lett.*, 69(4):503–505, 1996.
49. John A Weil and James R Bolton. *Electron paramagnetic resonance: elementary theory and practical applications*. John Wiley & Sons, 2007.
50. A Pöpll and G Völkel. ESR and Photo-ESR Investigations of Zinc Vacancies and Interstitial Oxygen Ions in Undoped ZnO Ceramics. *physica status solidi (a)*, 125(2):571–581, 1991.
51. K Vanheusden, CH Seager, WL t Warren, DR Tallant, and JA Voigt. Correlation between photoluminescence and oxygen vacancies in ZnO phosphors. *Appl. Phys. Lett.*, 68(3):403–405, 1996.

Chapter 3

Synthesis and Experimental Techniques

In this section, we describe the synthesis and experimental techniques used in this thesis to study the structural, electronic, optical and magnetic properties of the magnetic ions-doped ZnO NCs. We first explain, briefly, the sol-gel syntheses process to obtain the samples. Then, we introduce the structural, morphological and electronic structure characterization techniques: X-ray diffraction (XRD), high-resolution transmission electron microscopy (HRTEM) and X-ray photoelectron spectroscopy (XPS). An overall description of the main features of the synchrotron radiation, beamline facilities and, especially, on the X-ray absorption mechanisms: X-ray absorption near edge spectroscopy (XANES) and extended X-ray absorption spectroscopy (EXAFS)—to study the local and electronic structure of the nanocrystals, is included. Finally, the experimental techniques used to study the optical and the magnetic properties i.e., photoluminescence, electron paramagnetic resonance (EPR) and SQUID-based magnetometry are presented.

3.1 Synthesis of ZnO Nanocrystals

3.1.1 *Synthesis—The Sol-Gel Process*

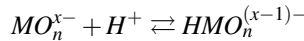
The sol-gel method is a versatile method useful for preparing metal oxides. Stoichiometric and homogeneous control of the doping is easily achieved. Since liquid precursors are used, it is possible to obtain a range of shapes (e.g., thin film, fibers and monoliths, etc.) without the need for machining or melting. The precursors such as metal alkoxides, with very high purity, make it easy to fabricate materials with high quality and cost-effective and the temperature required during the process is low and no vacuum facilities are needed.

The sol-gel process means the synthesis of an inorganic network by a chemical reaction in solution at low temperature. Starting from molecular precursors, an oxide network is obtained via inorganic polymerization reactions [1]. The most obvious fea-

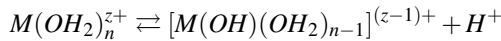
tures of this reaction, the transition from a liquid (solution or colloidal solution) into a solid (di- or multiphase gel) led to the expression "sol-gel process". This type of reaction, of course, is not necessarily restricted to an aqueous system, but aqueous reactions like these have been known for a very long time. These reactions mainly occur in solutions and the term "sol-gel processing" is often broadly used to describe the synthesis of inorganic oxides by wet chemical methods. It offers many advantages compared to the conventional "powder" route, such as lower temperature processing or better homogeneity for multi-component materials [2].

The sol-gel chemistry is based on inorganic polymerization reactions. Two routes are usually described in the literature depending on whether the precursor is an aqueous solution of an inorganic salt or an alkoxide in an organic solvent [3]. In both cases, the reaction can be described as follows:

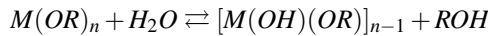
(i) Hydroxylation of the precursor leading to the formation of M–OH bonds: the hydroxylation of inorganic precursor is performed via a pH modification of the aqueous solution leading to the protonation of anionic oxo-ions:



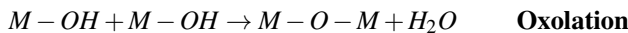
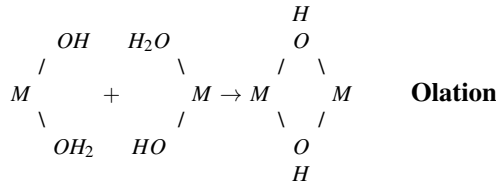
or the deprotonation of cationic aquo-ions:



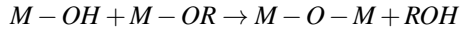
The hydroxylation of alkoxides is simply performed via hydrolysis by adding water:



(ii) Condensation: a polycondensation process follows the hydroxylation reaction leading to the departure of a water molecule:



or an alcohol molecule:



In both cases hydroxy or oxygen bridges are formed leading to condensed species. At the end of the process, all oxygen atoms are bridging oxygen and a hydrated oxide network is obtained [4]. Inorganic networks can also be built up by other chemical reactions—from the vapor phase or by high-temperature processes like melting.

For the synthesis of our NCs, absolute ethanol ($\text{CH}_3\text{CH}_2\text{OH}$, 99.95%, Vetec) was used as synthesis and washing solvent; zinc acetate dihydrate ($\text{Zn}(\text{CH}_3\text{CO}_2)_2 \cdot 2\text{H}_2\text{O}$, 99.999%, Sigma-Aldrich) as Zn precursor; Sodium hydroxide (NaOH, ACS reagent, $\geq 97.0\%$, Sigma-Aldrich) to perform the hydrolysis and Nickel(II) acetate tetrahydrate (Sigma-Aldrich), Cobalt(II) acetate tetrahydrate (99.999%, Sigma-Aldrich) and Terbium (III) acetate hydrate (Sigma-Aldrich) as doping precursors.

3.1.2 Preparation of the Precursor and Ethanolic Base

The ZnO precursor was prepared from an ethanolic solution (0.101 M) of zinc acetate ($\text{Zn}(\text{CH}_3\text{CO}_2)_2 \cdot 2\text{H}_2\text{O}$)—kept under a thermal bath at 60°C for 30 min, with continuous stirring. The base used in the hydrolyzing and condensation reaction of the derived precursor for ZnO formation were prepared from an ethanolic solution of (0.552 M) NaOH under a thermal bath at 60°C for approximately 30 min to solubilize the base. These solutions were then cooled to room temperature and stored in a freezer at -10°C , before use.

3.1.3 Samples Preparation

Nanocrystalline ZnO was synthesized at 45°C by the addition of an ethanolic solution of sodium hydroxide (NaOH) to zinc acetate dihydrate ($\text{Zn}(\text{CH}_3\text{CO}_2)_2 \cdot 2\text{H}_2\text{O}$) dissolved in ethanol. In a typical preparation, 50 mL of 0.552 M NaOH in ethanol was added to a 50-mL solution of 0.101 M $\text{Zn}(\text{CH}_3\text{CO}_2)_2 \cdot 2\text{H}_2\text{O}$ in ethanol under constant stirring. The addition was done at 10°C and kept for 15 min at this temperature to avoid sudden reaction and growth of the nanocrystals [5].

Then, the temperature was increased to 45°C which was kept constant for 2 hours. The doping was achieved by adding the Ni, Co or Tb precursor to the ZnO precursor solution. In our doping experiments, the concentration of zinc ions was reduced to keep the total initial concentration of metal ions constant. In this way, nanocrystals may be precipitated by centrifugation at 3000 rpm during 10 min, subsequent washing process with ethanol and resuspension in ethanol. Aggregates of Ni-, Co-, and Tb-doped ZnO NCs were obtained by simply allowing the solvent to evaporate from a concentrated

ethanol solution at 60 °C in a furnace and further thermal treatment at 250 °C during 2 hours.

Samples with different compositions were finally synthesized and used to obtain the different measurements presented in this thesis. The samples were named depending on the dopant and concentration, see Table 3.1.

Table 3.1 Synthesized samples

Dopant	Concentration (mol%)	Sample name
—	0	ZnO
Ni	1	ZnO:Ni1
	3	ZnO:Ni3
	5	ZnO:Ni5
	10	ZnO:Ni10
Co	1	ZnO:Co1
	3	ZnO:Co3
	5	ZnO:Co5
	10	ZnO:Co10
Tb	1	ZnO:Tb1
	3	ZnO:Tb3
	5	ZnO:Tb5
	10	ZnO:Tb10

3.2 Structural Characterization

3.2.1 X-ray Diffraction

The X-ray diffraction measurements were made in collaboration with Dr. Marcelo Sousa at the Faculty of Ceilândia - University of Brasilia, using a *Rigaku Miniflex 600* X-ray diffractometer with $CuK\alpha$ radiation. The data were collected from 10 to 90 °, with a step size fixed at 0.05 ° and a rate scan of 1.5 °/min—at room temperature. The NIST SRM640d standard Si were used to determine the instrumental linewidth. The profile peak shape was described using a Thompson-Cox-Hastings (TCH) pseudo-Voigt function: convolution of a Gaussian (H_G) and a Lorentzian (H_L) shapes [6], with an additional term which accounts for anisotropic particle size broadening effects. The Full width at half maximum - FWHM (H) was easily obtained using the numerical approximation provided by TCH relation (Eq. 3.1) and the integral breath (β) of the Voigt function is then calculated using the Eq. 3.3 of the pseudo-Voigt approximation, through the previous calculation of (H) and η using the Eq. 3.1 and 3.2.

$$H^5 = (H_G^5 + 2.69269H_G^4H_L + 2.42843H_G^3H_L^2 + 4.47163H_G^2H_L^3 + 0.07842H_GH_L^4 + H_L^5) \quad (3.1)$$

$$\eta = 1.36603 \frac{H_L}{H} - 0.47719 \left(\frac{H_L}{H} \right)^2 + 0.11116 \left(\frac{H_L}{H} \right)^3 \quad (3.2)$$

$$\beta = \frac{\pi H/2}{\eta + (1 - \eta)\sqrt{\pi \ln 2}} \quad (3.3)$$

The volume of the unit cell for the hexagonal system has been calculated using the following relation [7]:

$$V = 0.866a^2c \quad (3.4)$$

The Rietveld refinement was performed using the fourth function of GSAS package [8, 9] and, to deal with preferred orientation, the 8th order for the spherical harmonic correction (Orientational Distribution Function) was used. The crystallite size was estimated using the Scherrer's relation: $D_p = k\lambda / \beta \cos\theta$, where D_p is the average crystallite size in Å, λ is the wavelength of $CuK\alpha$ radiation (1.5418 Å), k is the Scherrer's constant (~ 1), β is the integral breadth of the peak, and θ is the diffraction angle.

3.2.2 Transmission Electron Microscopy

The transmission electron microscopy (TEM) is a technique whereby an electron beam is transmitted through an ultra-thin specimen to form an image. As a consequence of the small de Broglie wavelength of electrons, TEMs are capable of imaging at a significantly higher resolution than light microscopes. This enables to examine structures as small as a single column of atoms. This technique usually combines the high resolution imaging with elemental microanalysis and electron diffraction, so that a complete characterization of the shape, size, chemical composition and crystalline structure of nanoparticulate materials is achieved. In a TEM microscope, an electron gun located at the top of it emits the electrons by thermionic or field emission. These electrons travel through the vacuum in the column of the microscope where electromagnetic lenses focus them into a very thin beam. The electron beam then travels through the specimen to study. At the bottom of the microscope, the image is formed on the image plane of the objective lens from the unscattered electrons. Then, projector lenses form the images on a screen or charged coupled device (CCD) camera [10].

The interaction between electrons and matter is much stronger than that with visible light; then, one of the main requirements for applying this technique is that the sample must be thin enough—thickness below 100 nm—for electrons to pass through. It

exists a variety of procedures to prepare samples for TEM observation, depending on the kind of materials and their nature. In this case, the samples were quickly prepared by the deposition of a diluted sample containing the specimen onto Cu support grids. Individual particle size for the pure ZnO NCs was obtained by digital processing the taken images using the *ImageJ* software and they were used to mount the histogram of the particle size distribution according to the Sturges method. A log-normal distribution function was used to fit the histogram. The probability density of a log-normally distributed variable D is given by:

$$y = \frac{1}{\sqrt{2\pi}\sigma D} \exp \left\{ \frac{-\ln^2(D/D_0)}{2\sigma^2} \right\} \quad (3.5)$$

where σ is the standard deviation of the log of the distribution, D_0 is the median and $\langle D \rangle (= D_0 \exp(\sigma^2/2))$ the mean value [11].

The interplanar distances were measured from the Fourier transform of the high-resolution TEM images with the help of the *ImageJ* software.

3.2.2.1 JEOL JEM 2100 TEM

The JEOL JEM 2100 field emission microscope of the "Laboratório Multiusuário de Microscopia de Alta Resolução (LabMic)" at the Federal University of Goiás, was used to obtain the images of the nanocrystals that we show in this thesis. This microscope operates at acceleration voltage up to 200 kV and it is implemented with a ThermoNoran energy dispersive X-ray spectrometer (EDS). Ultrahigh TEM resolution as high as 0.19 nm enables to perform an observation at atomic resolution. Its high-resolution performance is then complemented by the ability to perform chemical microanalysis from sub-nanometre areas.

3.2.3 X-ray Photoelectron Spectroscopy

The XPS technique is very sensitive to chemical species; the peak positions depend on the local structure of the atoms and provide the information about the chemical state. The spectra shown in this thesis were obtained at the Brazilian Nanotechnology National Laboratory (LNNano), using a multiuser purpose XPS spectrometer (XPS, *Thermo Scientific™ K-Alpha™*) equipped with *AlK α* (1486.71 eV) X-ray monochromatic source. Before to analyze the data all the binding energies were corrected using the hydrocarbon component set at 284.8 eV and the inelastic noise of the O1s, Zn2p, Ni2p, and Tb3d spectra were subtracted using the Shirley method. Then, the spectra were deconvoluted with Voigtian-type functions, which combine Gaussian and Lorentzian profiles.

3.3 X-ray Absorption Spectroscopy Using Synchrotron Radiation

Elemental selectivity is one of the main features of X-ray absorption spectroscopy (XAS), which makes it suitable to analyze problems of different nature. XAS spectroscopy using a synchrotron radiation source is a powerful tool to determine the local structure of a specific atom and the electronic structure, regardless of the physical state of the sample. X-rays are ionizing radiation with sufficient energy to eject (or remove) a core electron (tightly bound) from an atom during an interaction. Each core-shell has a specific binding energy, and thus if one plots X-ray absorption as a function of energy, the spectrum for any atom resembles the X-ray absorption spectrum shown in Fig. 3.1. When the X-ray energy is scanned through the binding energy of a core shell, there is an abrupt increase in the absorption cross section. This gives rise to a so-called absorption edge, with each edge representing a different core-electron binding energy. The absorption edges are named according to the principal quantum number of the electron that is excited: K for $n = 1$, L for $n = 2$, M for $n = 3$, etc. The core-electron binding energy increases with increasing atomic number, ranging from 284 eV for the C K edge to 115606 eV for the U K edge, with the L edges at significantly lower energies than the corresponding K edge (e.g., 270 eV for the Cl L1 edge, 20948 eV and 17166 eV for the U L2 and L3 edges, respectively). The L edge is composed in fact by three distinct L edges, named L1, L2, and L3 according to the decreasing energy. L1 corresponds to the excitation of a 2s electron. The 2p excitation is split into two edges, L2 and L3, as a consequence of the spin-orbit coupling energy of the $2p^5$ configuration that is created when a 2p electron is excited. The higher energy of the $2p^5$ excited states is the $2P_{1/2}$ term. It gives rise to the L2 edge. At lower energy is the L3 edge, corresponding to the $2P_{3/2}$ excited state. Due to degeneracy, the L3 edge has twice the edge jump of the L2 and L1 edges [12, 13].

The X-ray absorption spectrum is typically divided into two regions: X-ray absorption near-edge spectroscopy (XANES)—typically within 30 eV of the main absorption edge, and extended X-ray absorption fine-structure spectroscopy (EXAFS) which spans the 30–2000 eV above the edge, as shown in Fig. 3.1. Though the two have the same physical origin, this distinction is convenient for the interpretation. EXAFS results from the interference in the single scattering process of the photoelectron scattered by surrounding atoms and provides information about the coordination number, the nature of the scattering atoms surrounding the absorbing atom, the interatomic distance between absorbing and backscattering atoms, and the Debye-Waller factor which accounts for the disorders due to the static displacements and thermal vibrations. The XANES region provides information about oxidation states, vacant orbitals, electronic configuration, and site symmetry of the absorbing atom (e.g., octahedral or tetrahedral coordination geometry). The XANES spectra may have pre-edge peaks related to the electronic transitions taking place between the different shells. The strength of such pre-edge peaks strongly depends on the coordination geometry around the absorbing atom and can, therefore, be used as an indication of geometrical changes. As we mention, the basic physical description of these two regimes is the same, but some important approximations and limits allow us to interpret the extended spectra in a more quantitative way than is currently possible for the near-edge spectra.

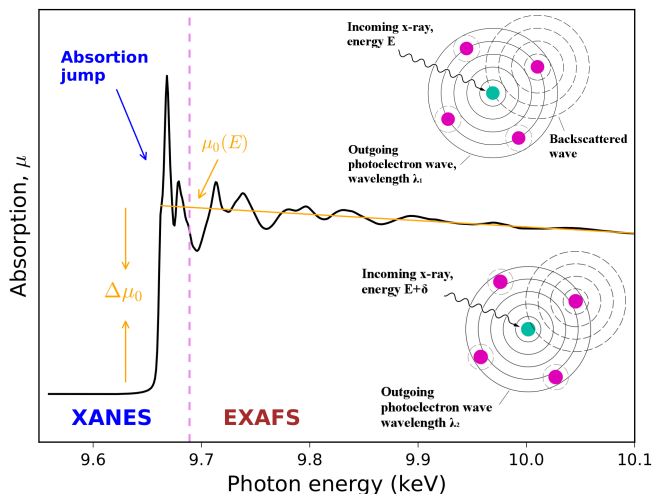


Fig. 3.1 X-ray absorption spectrum: XANES and EXAFS regions

For the EXAFS, we are interested in the oscillations well above the absorption edge, and we define the EXAFS fine-structure function $\chi(E)$ as:

$$\chi(E) = \frac{\mu(E) - \mu_0(E)}{\Delta\mu_0(E)} \quad (3.6)$$

Where $\mu(E)$ is the measured absorption coefficient, $\mu_0(E)$ is a smooth background function representing the absorption of an isolated atom, and $\Delta\mu_0(E)$ is the measured jump in the absorption $\mu(E)$ at the threshold energy E_0 .

EXAFS is best understood in terms of the wave behavior of the photoelectron created in the absorption process. Because of this, it is common to convert the X-ray energy to k , the wave number of the photoelectron, which has dimensions of 1/distance and is defined as:

$$k^2 = 2m(E - E_0)/\hbar^2 \quad (3.7)$$

Where E_0 is the absorption edge energy and m is the electron mass. The primary quantity for EXAFS is then $\chi(k)$, the oscillations as a function of photoelectron wave number, and $\chi(k)$ is often referred to simply as “the EXAFS”. The different frequencies apparent in the oscillations in $\chi(k)$ correspond to different near-neighbor coordination shells which can be described and modeled according to the EXAFS Equation,

$$\chi(k) = S_0^2 \sum_i N_i \frac{f_i(k)}{kR_i^2} e^{-2R_i/\lambda(k)} e^{-2k^2\sigma_i^2} \sin(2kR_i + \phi_{ij}(k)) \quad (3.8)$$

where $f_i(k)$ and $\phi_{ij}(k)$ are scattering properties of the atoms neighboring the excited atom, N_i is the number of neighboring atoms, R_i is the distance to the neighboring atom, σ_j^2 is the disorder in the neighbor distance known as Debye-Waller factor, and S_0^2 is the amplitude reduction due to many-body effects. The term $\exp(-2R_i/\lambda(k))$ is due to inelastic losses in the scattering process, with $\lambda(k)$ being the electron mean free path. Though somewhat complicated, the EXAFS equation allows us to determine N , R , and σ^2 knowing the scattering amplitude $f(k)$ and effective scattering phase shift $\phi(k)$ for each path [13, 14] (see Appendix A for further details).

3.3.1 XAFS1 and XAFS2 Beamlines at the LNL

The XAFS experiments on the samples studied here were performed in collaboration with Dr. Santiago Figueroa at the general purpose X-ray absorption spectroscopy XAFS1 (D08B (15°)) and XAFS2 beamlines at the LNL. Those beamlines are dedicated to XAFS experiments in the hard X-rays energy range (3.5 to 17.0 keV), coming from a bending magnet. A schematic diagram of a conventional XAFS beamline, as D08B (15°), is shown in Fig. 3.2. The white beam delivered by the bending magnet source was monochromatized by using a fixed-exit double-crystal Si(111) monochromator operated in flat crystal mode. Two Rh-coated cylindrical mirrors were used for harmonics rejection. The first Rh-coated cylindrical mirror which sends a parallel synchrotron beam onto the two flat Si(111) double crystal monochromator and the second Rh coated toroidal bendable mirror refocuses the monochromatic beam, in the sample position, to a low eccentricity ellipse of approximately 450 μm in diameter. The typical photon flux, in the sample position, for standard beam size and the current ring is around the 10^9 photon/s. The details of the beamline have been described elsewhere [15]. For the present work, each sample in powder state was dissolved in isopropyl alcohol and embedded in a cellulose matrix. The concentration was adjusted to yield an extinction of 1.5. The prepared pellets were encapsulated by Kapton tape and mounted on to sample holders for the EXAFS measurements. Zn K-edge XANES and EXAFS measurements were done in the XAFS1 beamline in transmission mode and the energy was calibrated using standard Zn foil. Ni, Co, and Tb atoms were measured at the Ni K-, Co K-, and Tb L3-edge in fluorescence mode in the XAFS2 beamline and calibrated using standard Ni and Co. XAFS spectra were measured at room temperature up to 1000 eV above the edge with a constant energy step of 0.3 eV in the XANES region, energy steps increasing from 2 to 5 eV in the EXAFS region, and an integration time of 3 s/point. For each sample, two spectra were averaged—four in the case of the Ni K-, Co K-, and Tb K-edge, in order to improve the signal-to-noise ratio.

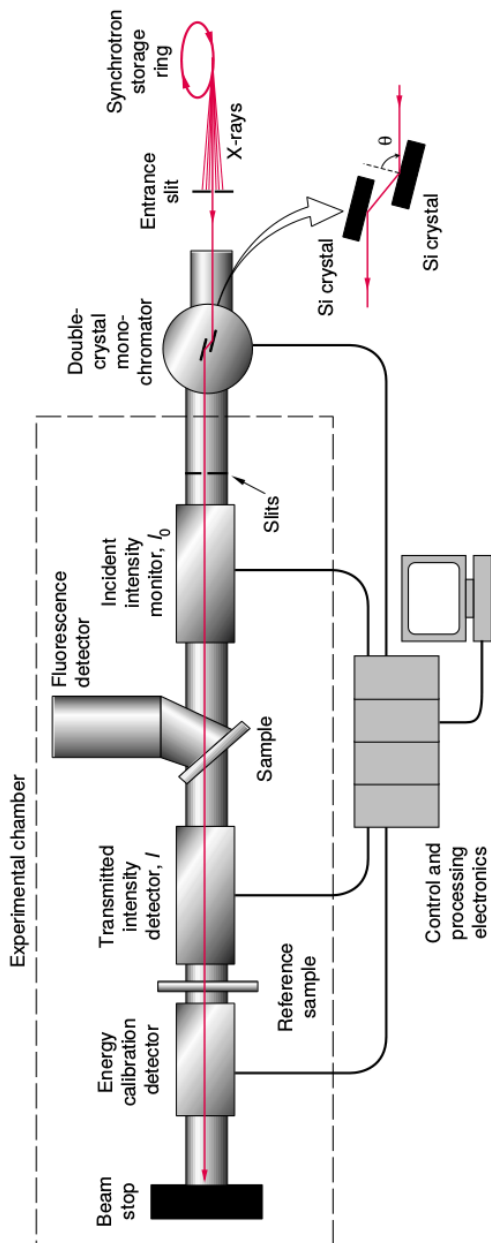


Fig. 3.2 A typical XAFS station for Transmission and Fluorescence XAFS.

The data were handled using the Athena interface of the Demeter package. For the analysis of the EXAFS data, the energy-dependent absorption coefficient $\mu(E)$ has been converted to the energy-dependent absorption function $\chi(E)$, and then to the wavenumber-dependent absorption coefficient $\chi(k)$. Finally, the k^2 -weighted $\chi(k)$ spectra were Fourier-transformed in R space to generate the $\chi(R)$ versus R spectra in terms of the real distance from the center of the absorbing atoms. The analysis of the EXAFS data has been carried out following the standard procedures using the Artemis and IFEFFIT software package (see Appendix A).

3.4 Photoluminescence Measurements

Photoluminescence measurements were performed in collaboration with Dr. Marcio Daldin at the experimental facilities of the Semiconductor Nanostructures Group - Department of Physics at the University of São Carlos¹. The photoluminescence system is composed by the excitation of a Helium-Cadmium laser (Kimmon-Koha company), with emission lines at 325 and 442 nm. This laser is coupled in multi-mode optical fibers with 105 μm core diameter and 0.22 numerical aperture (Thorlabs M111L02) through high precision optomechanical couplers. These fibers are of the solarization resistant type, chosen to be able to guide light in the ultraviolet region without degradation and emission of fluorescence by the materials that compose them. They are also customized with FC/APC type connectors to eliminate back-reflection effects of the beam within the laser itself. For these measurements, a sample-holder with small holes of 1 mm in diameter and depth was used. The samples were placed and lightly pressed on the holes to obtain a good mechanical adhesion and consequent heat exchange. Then, the sample-holder was placed inside a helium closed cycle cryostat implemented with a temperature controller (Lakeshore 335) that allows variation from 10 to 300 K. An optics specially designed for these types of measurements was designed to operate with the use of optical fibers. The fiber-guided laser is collimated by a quartz lens with a focal length of 50 mm and a diameter of 25.4 mm, and focused on the sample by another lens of the same diameter and focus of 100 mm, both positioned at a 45-degree angle in relation to the sample. We have a sample focused laser spot of approximately 200 μm in diameter. The luminescence collection optics are positioned in front of the cryostat window, where a 25.4 mm diameter 50 mm focus lens collimates the light emitted by the sample, and focused on a second optical fiber (identical to that of excitation) by a second lens with 25.4 mm of focus, demagnifying the image produced by the sample to the same value of the fiber core, thus ensuring that the whole cone of light is projected within this fiber. Between the lenses, a bandpass filter (Semrock LP03-325RE-25) was positioned to absorb the laser scattered and allow only the passage of luminescence. The luminescence, in turn, was guided by the fiber to the entrance of a detection system (manufactured by the company Andor), composed by a spectrometer of 75 cm, a diffraction grating with 150 lines/mm (blaze in 500 nm) and detected by a CCD silicon detector. At the entrance of the spectrometer, two other

¹ <http://nanostructures.df.ufscar.br/index.php/en/>

quartz lenses were positioned, one in front of the fiber with a focus of 25.4 mm for light collimation and a second with a focus of 50 mm for focusing on the spectrometer entrance. Taking the ratio between the foci and the diameter of the fiber, the light beam is incident on the 200 μm spectrometer slot, which is chosen by opening the slit. The values of the lens parameters when conjugated are also compatible with the numerical aperture of the spectrometer so that the CCD chip is completely illuminated by the light emitted by the sample. Finally, a software in Labview was used to control the instruments and carry out the measurements. In a simple way, all the necessary parameters are chosen, and the measurements are performed between the previously selected temperature range (10 to 300 K in this case), with the chosen step and time of stabilization between one measurement and other. In this way, a complete temperature variation for each sample was made with an average time of two and a half hours.

3.5 Electron Paramagnetic Resonance

Among several spectroscopic experiments, the advantage of the electron paramagnetic resonance (EPR) is its extreme sensitivity to the microscopic environment of the paramagnetic center. EPR offers an incomparable way to investigate ground states of localized magnetic impurities and defect centers in the NCs; and, in turn, to deduce many structural, electronic and magnetic information on these impurities, defects and the NCs themselves. When the EPR signal is detected it can give precious information on the magnetic impurities and their local environment at the atomic scale. If the nanocrystals are single crystalline and possess a coherent orientation the obtained information is maximal [16]. Although this technique can distinguish effectively paramagnetic species of metal particles, it has a special interest when these particles are diminished to nanoscale such as in the case where nanosized particles exist [17]. Correlation of EPR and optical spectroscopies hence allows one to yield a more complete insight into defect structures in general and into ZnO in particular [18].

Electron paramagnetic resonance (EPR) measurements have been performed on a conventional Bruker EMX Plus X-band spectrometer operating at X-band ($\nu \sim 9.50$ GHz) and using a standard TE102 mode cavity. To perform the measurement, a sample was hold in a quartz tube. The modulation of the static field (5 and 1G) at a frequency of 100 kHz was used with a lock-in amplifier to increase sensitivity and record the derivative of the EPR signal. The measurements have been performed at a temperature of 100 K with a nitrogen gas flow cryostat.

3.6 SQUID-Based Magnetometry

A magnetometer is an instrument used for the magnetic characterization of materials by measuring the strength and/or direction of magnetic fields. A superconducting quantum interference device (SQUID) is the most sensitive device available for such

purposes. It works as an extremely sensitive current-to-voltage converter, so that, when integrated to a Quantum Design magnetic property measurement system (MPMS), the complete system is a magnetic flux to voltage transducer. The fact of directly measuring magnetic flux is one of the main advantages of SQUID magnetometry, allowing to measure moments on the order of 10^{-7} emu [19]. A picture of the MPMS of the Magnetic Characterization Laboratory of the Institute of Physics at the University of Brasilia, which have been used for the magnetic characterization described in this thesis, is shown in Fig. 3.3. Schematic of the measurement process of a magnetic sample in this equipment is displayed in Fig. 3.3. In a MPMS, the SQUID does not detect directly the magnetic field from the sample since it may be interfered by any flux from nearby magnetic systems or even the earth's magnetic field. Instead, a measurement is performed by moving a sample through a system of superconducting pick-up coils, two of them with the same sense very closely spaced, and the other two of the opposite sense, spaced symmetrically outside. This system is located outside the sample chamber at the center of the superconducting magnet. As the sample moves through the coils, the magnetic moment of the sample induces an electric current in the detection coils. Because of the detection coils, the connecting wires, and the SQUID input coil form a closed superconducting loop, any change of magnetic flux in the detection coils produces a change in the persistent current in the detection circuit, which is proportional to the change in magnetic flux. Since the SQUID is a highly linear current-to-voltage converter, the variation in the current in the detection coils produces corresponding variations in the SQUID output voltage. Based on this profile of voltage versus position of the sample, given the assumption that the signal is from a point dipole, the magnetic moment can be determined [20].



Fig. 3.3 (Left) MPMS magnetometer of the Magnetic Characterization Laboratory of the Institute of Physics at the University of Brasilia and, (right) Schematics of the SQUID-based measurement system [21].

Magnetic measurements were obtained as a function of the temperature (5–300 K) and magnetic field (0 to ± 70 kOe) using a commercial magnetometer previously described (Quantum Design, MPMS) equipped with a superconducting magnet. Measurements were carried out on tightly packed powder samples placed in a special non-magnetic sample holder. The data reported here were corrected for the background

signal from the sample holder which shown a diamagnetic susceptibility. Data analyses were carried out using Python utilities.

References

1. C Jeffrey Brinker and George W Scherer. *Sol-gel science: the physics and chemistry of sol-gel processing*. Academic press, 2013.
2. H Schmidt. Chemistry of material preparation by the sol-gel process. *J. Non-Cryst. Solids*, 100(1-3):51–64, 1988.
3. Larry L Hench and Jon K West. The sol-gel process. *Chem. Rev.*, 90(1):33–72, 1990.
4. J Livage, C Sanchez, M Henry, and S Doeuff. The chemistry of the sol-gel process. *Solid state ionics*, 32:633–638, 1989.
5. Bożena Sikora, Krzysztof Fronc, Izabela Kaminska, Anna Baranowska-Korczyk, Kamil Sobczak, Piotr Dłużewski, and Danek Elbaum. The growth kinetics of colloidal ZnO nanoparticles in alcohols. *J. Sol-Gel Sci. Technol.*, 61(1):197–205, 2012.
6. P Thompson, DE Cox, and JB Hastings. Rietveld refinement of Debye–Scherrer synchrotron X-ray data from Al₂O₃. *J. Appl. Crystallogr.*, 20(2):79–83, 1987.
7. Vijayaprasath Gandhi, Ravi Ganesan, Haja Hameed Abdulrahman Syedahamed, and Mahalingam Thaiyan. Effect of cobalt doping on structural, optical, and magnetic properties of ZnO nanoparticles synthesized by coprecipitation method. *J. Phys. Chem. C*, 118(18):9715–9725, 2014.
8. Allen C Larson and Robert B Von Dreele. GSAS. *Report IAU*, pages 86–748, 1994.
9. Brian H Toby. EXPGUI, a graphical user interface for GSAS. *J. Appl. Crystallogr.*, 34(2):210–213, 2001.
10. David B Williams and C Barry Carter. The transmission electron microscope. In *Transmission electron microscopy*, pages 3–17. Springer, 1996.
11. P Bender, C Balceris, F Ludwig, O Posth, LK Bogart, Wojciech Szczerba, A Castro, L Nilsson, R Costo, H Gavilán, et al. Distribution functions of magnetic nanoparticles determined by a numerical inversion method. *New Journal of Physics*, 19(7):073012, 2017.
12. Alfred Beverley Philip Lever. *Comprehensive coordination chemistry II: from biology to nanotechnology*. Elsevier, 2004.
13. Matthew Newville. Fundamentals of XAFS. *Reviews in Mineralogy and Geochemistry*, 78(1):33–74, 2014.
14. Grant Bunker. *Introduction to XAFS: a practical guide to X-ray absorption fine structure spectroscopy*. Cambridge University Press, 2010.
15. SJA Figueroa, JC Mauricio, J Murari, DB Beniz, JR Piton, HH Slepicka, M Falcão de Sousa, AM Espíndola, and APS Levinsky. Upgrades to the XAFS2 beamline control system and to the endstation at the LNLS. In *Journal of Physics: Conference Series*, volume 712, page 012022. IOP Publishing, 2016.
16. Adrien Savoyant, Hatim Alnoor, Sylvain Bertainat, Omer Nur, and Magnus Willander. EPR investigation of pure and Co-doped ZnO oriented nanocrystals. *Nanotechnology*, 28(3):035705, 2016.
17. B Babu, G Rama Sundari, K Ravindranadh, M Rajesh Yadav, and RVSSN Ravikumar. Structural, spectroscopic and magnetic characterization of undoped, Ni²⁺-doped ZnO nanopowders. *J. Magn. Mater.*, 372:79–85, 2014.
18. Hülya Kaftelen, Kasim Ocakoglu, Ralf Thomann, Suyan Tu, Stefan Weber, and Emre Erdem. EPR and photoluminescence spectroscopy studies on the defect structure of ZnO nanocrystals. *Phys. Rev. B*, 86(1):014113, 2012.
19. RL Fagaly. Superconducting quantum interference device instruments and applications. *Rev. Sci. Instrum.*, 77(10):101101, 2006.
20. Mike McElfresh. Fundamentals of magnetism and magnetic measurements featuring Quantum Design’s magnetic property measurement system. *Quantum Design*, 11578:132, 1994.

21. Adriana I Figueroa. *Magnetic Nanoparticles: A Study by Synchrotron Radiation and RF Transverse Susceptibility*. Springer, 2014.

Chapter 4

Structural and Local Structural Properties of doped ZnO Nanocrystals

In this section, we present a systematic study of the structural and local structural properties of the pure and doped ZnO NCs systems. The size and composition of the NCs were changed by varying the concentration of dopant. The effects of the dopants on the local structure of the particles were studied via X-ray diffraction (XRD), high-resolution transmission electron microscopy (HRTEM) and extended X-ray absorption fine structure (EXAFS) measurements.

4.1 X-ray Diffraction Analysis

X-ray diffraction was used to obtain detailed information about the crystalline structure of the pure and doped ZnO NCs. It is worth to mention that the GSAS-EXPGUI [1, 2] package was used to refine the diffractograms with the Rietveld method. The fourth function of the GSAS package and, to deal with a preferred orientation, the 8th order for the spherical harmonic correction (Orientational Distribution Function) was used. The lattice parameters and the full width at half maximum (FWHM) of the diffraction peaks were used to determine the cell volume and the crystallite size (see Chap. 2 for further details). The Rietveld-refined XRD patterns of the doped ZnO NCs are presented along with the graphical description of the structural parameters in Fig. 4.1, 4.2 and 4.3. The results of the refined parameters are also provided in Table 4.1. As can be observed—for nickel, cobalt, and terbium at different concentrations—all the detected peaks resemble the standard Bragg positions of the hexagonal wurtzite structure (space group $P6_3mc$, JCPDS: 36-1451), which have been indicated by the red lines at the top and bottom of the XRD patterns. This result confirms the formation of the hexagonal ZnO wurtzite crystal structure. No additional reflections due to secondary phases such as NiO, CoO, Co_2O_3 , Co_3O_4 , TbO, Tb_2O_3 , Tb_3O_4 , Tb_4O_7 or $Zn-(OH)_2$ are present. However, within the detection limit of the XRD technique, the existence of phases containing nickel, cobalt, and terbium in small quantities or small clusters cannot be completely ruled out.

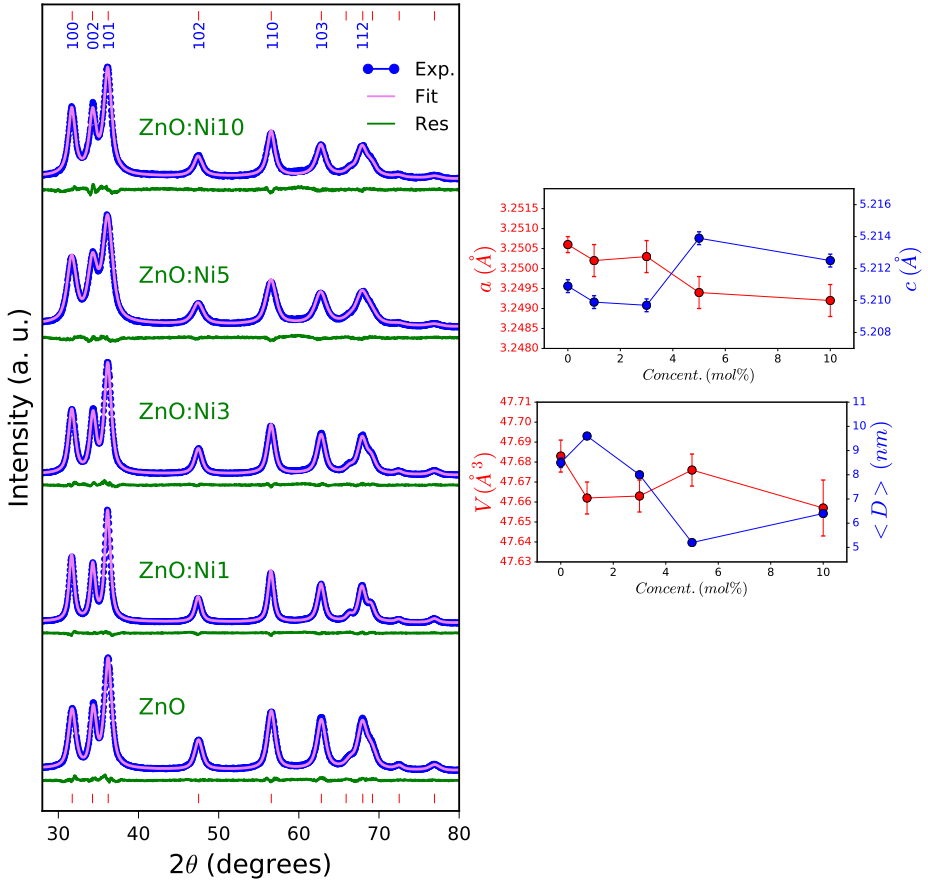


Fig. 4.1 (Left) Rietveld refinement of the Ni-doped ZnO NCs and, (right) graphical behaviour of the structural parameters.

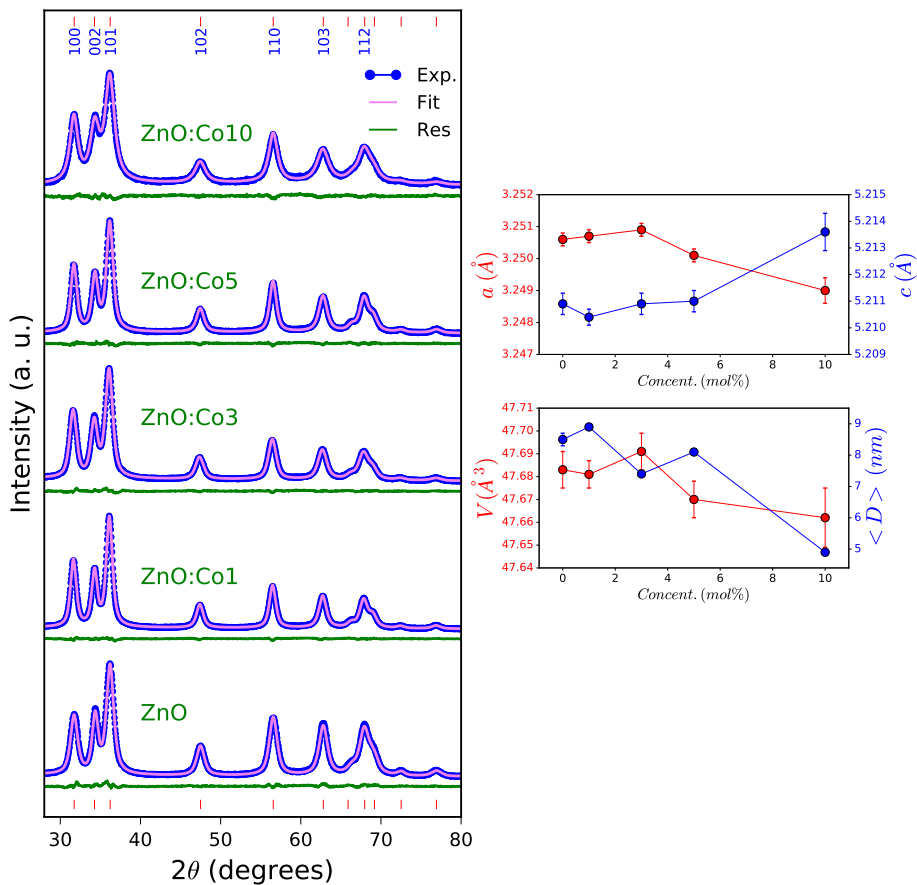


Fig. 4.2 (Left) Rietveld refinement of the Co-doped ZnO NCs and, (right) graphical behaviour of the structural parameters.

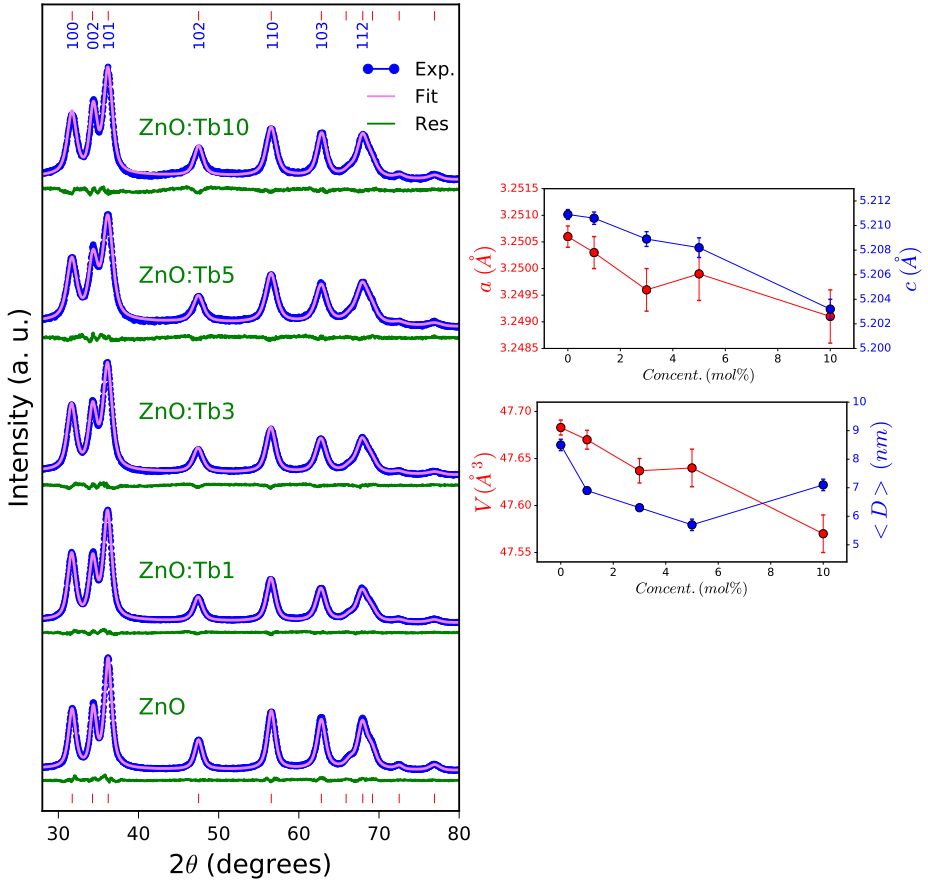


Fig. 4.3 (Left) Rietveld refinement of the Tb-doped ZnO NCs and, (right) graphical behaviour of the structural parameters.

Table 4.1 List of structural parameters of pure and doped ZnO NCs obtained from the XRD patterns refined with the Rietveld method.

Sample	a-parameter (Å)	c-parameter (Å)	Cell volume (Å ³)	Crystallite size (nm)
ZnO	3.2506 (2)	5.2109(4)	47.683 (8)	8.5 (2)
ZnO:Co1	3.2507 (2)	5.2104 (3)	47.681 (6)	8.9 (1)
ZnO:Co3	3.2509 (2)	5.2109 (4)	47.691 (8)	7.4 (1)
ZnO:Co5	3.2501 (2)	5.2110 (4)	47.670 (8)	8.1 (1)
ZnO:Co10	3.2490 (4)	5.2136 (7)	47.662 (13)	4.9 (1)
ZnO:Ni1	3.2502 (4)	5.2099 (4)	47.662 (8)	9.6 (1)
ZnO:Ni3	3.2503 (4)	5.2097 (4)	47.663 (8)	8.0 (1)
ZnO:Ni5	3.2494 (4)	5.2139 (4)	47.676 (8)	5.2 (1)
ZnO:Ni10	3.2492 (4)	5.2125 (4)	47.657 (14)	6.4 (2)
ZnO:Tb1	3.2503 (3)	5.2106 (5)	47.67 (1)	6.9 (1)
ZnO:Tb3	3.2496 (4)	5.2089 (6)	47.637 (13)	6.3 (1)
ZnO:Tb5	3.2499 (5)	5.2082 (8)	47.64 (2)	5.7 (2)
ZnO:Tb10	3.2491 (5)	5.2032 (8)	47.57 (2)	7.1 (2)

A more detailed analysis of the X-ray spectra shows that as the dopant concentration increases, the FWHM has an increasing tendency, which, in turn, decreases slightly the crystallite size—this decreasing trend does not show a monotonic behavior (see Fig. 4.1, 4.2, 4.3 and Table 4.1). The reduction in the crystallite size is mainly due to the distortion in the host ZnO lattice by foreign impurities that acts as grain growth inhibitors; they decrease the nucleation and subsequent growth rate of ZnO NCs [3], which is in accordance with previous works [4]. In addition, it is established that, as the particle size decreases, the increasing number of surface and interface atoms generates stress/strain and concomitant structural perturbations [5]. The substitution of Zn²⁺ by other ions produces defects around the dopant due to the difference in size between the ions so that these defects lead to changes in the stoichiometry of the material [6]. Interstitial doping can also cause distortion of the ZnO structure. This is also frequently associated with an increased concentration of defects [7], especially holes introduced by the larger ionic radii of rare earth dopant ions. The lattice constants and unit cell volumes have been calculated using the equations provided in the Chap. 3. Changes in these parameters were observed due to the incorporation of dopant ions. In Fig. 4.1, 4.2 and Table 4.1 is shown the dependence of the lattice constants on the dopant concentration. As observed, the lattice constant “a” shows a decreasing tendency for Ni and Co and an increasing in c-lattice parameter because of doping. As a result, a decreasing tendency of the unit cell volume is determined. The difference in the lattice constants must be related to the fact that the ionic radii for tetrahedral coordination of Ni²⁺ (0.55Å) and Co²⁺ (0.58Å) are smaller than the ionic radius of Zn²⁺ (0.6Å) [8]. The cell volume decrease with the increasing of Ni and Co concentration; it suggests that Zn²⁺ ions were substituted by dopant ions in the ZnO structure. This trend is expected for a solid solution regime following the Vegard’s law [9]. M. Arshad et al. [10] reported similar results in the study of the influence of cobalt dopant in the ZnO matrix

obtained via sol-gel and, usually, it is considered as an evidence of successful incorporation of Ni^{2+} and Co^{2+} in sites occupied by Zn^{2+} sites in the ZnO lattice. Here, we will be a little more cautious about it, before analyzing the other techniques used to study our samples.

In the case of terbium, the lattice constants and the volume show a decreasing tendency (see Fig. 4.3 and Table 4.1). The structural analysis indicates the shift of the diffraction peaks to higher angles by increasing the Tb doping. At first, these results are contrary to what is expected for a substitutional doping. The ionic radius of Tb^{3+} (0.93 Å) and Tb^{4+} (0.76 Å) are very different from that of Zn^{2+} ions. Then, for a simple substitution of Tb on Zn sites, an increase in the lattice parameters and cell volume would be expected due to the larger difference. Though the precise mechanism of rare earth (RE) doping is not well known, the incorporation mechanisms of such elements in the wurtzite structure appear limited. Another option consists of the insertion of RE ions in the interstitial sites or non-occupied positions of the ZnO structure: four octahedral sites with six-fold coordination per unit cell are possible and the maximum radius of these unoccupied crystallographic positions is 0.88 Å, which is the theoretical ion size upper limit allowed. Nevertheless, it has never been demonstrated that ions with larger sizes such as rare earths follow this insertion pathway. Then, the reduction of the value of parameter “c” with the Tb concentration, despite the substitution of Tb on Zn sites, can only be explained by the formation of Tb-defect complexes [11].

Flemban et al., [11] have reported these features in Gd-doped ZnO films, which was corroborated with density functional theory calculations. They have confirmed that Gd-oxygen vacancy (V_O) complexes cause the contraction of lattice constant “c”; whereas the isolated Zn vacancy (V_{Zn}) enlarge “c”. In some vacancy configurations, the parameter “c” contracts meanwhile the parameter “a” remains constant. Those results are in line with our results obtained for Tb-doped ZnO NCs. Moreover, the authors indicated that isolated Gd atoms in substitutional sites (Gd_{subs}) must enlarge both lattice parameters as expected; therefore, it is expected also for Tb_{subs} ions. Minimizing the total energy of a series of configurations constructed in a 72-atom supercell, the authors showed the parameters of the energetically most favorable values; the V_O defects shrink the lattice, counteracting the expansion induced by Gd_{subs} impurities when they form $\text{Gd}_{\text{subs}}-V_O$ and $\text{Gd}-2V_O$ complexes. $\text{Gd}-2V_O$ complexes do not modify the parameter “a”. This result is in line with our XRD results and, furthermore, we believe that the induced cationic vacancies created by Tb^{3+} ions in the ZnO structure are responsible for the shrinkage of the c-axis length. Similar c-axis variations were also reported in Er-, Gd-, and Ce-doped ZnO systems [4, 12, 13].

4.2 Microscopy Measurements

High-resolution transmission electron microscopy (HRTEM) was used to further investigate the nanostructures of the samples. The Fig. 4.4 depicts HRTEM images of the pure ZnO NCs prepared via sol-gel method. Individual particle sizes for the pure ZnO NCs were obtained by processing the images using the *ImageJ* software. $N = 220$

particles were accounted to mount the histogram distribution using the Sturges criteria. Then, the histogram was fitted to a log-normal function to obtain the mean diameter and standard deviation (see Chap. 3 for more details). The values obtained from this analysis are shown in Fig. 4.4(d). As observed, the particles show circular- and elliptical-like shapes with an average size of 8.1 nm and a standard deviation of 0.2 nm. The calculated particle size by this method is in agreement with the crystallite size estimated from XRD measurements. In addition, the HRTEM images (Fig. 4.4(b) and 4.4(c)), show clear lattice fringes (interplanar distances) of $d = 2.6 \text{ \AA}$ as illustrated which corresponds well with the d -spacing of (002) planes of wurtzite ZnO. The interplanar distances $d = 2.46$ and 2.7 \AA shown in Fig. 4.4(c) were associated with (100) and (101) planes, respectively. These three different d -spacings are related to the main Bragg reflections of Zn—as depicted in the XRD patterns showed in Fig. 4.1, 4.2 and 4.3, and they have been observed for all the studied samples.

It was not possible to obtain the particle size distribution of the doped samples due to agglomeration of the particles. However, it is possible to judge the size of ZnO NCs intuitively by using the HRTEM images for Ni- and Co-doped ZnO samples, Fig. 4.5 and Fig. 4.6, respectively. The results are in general in agreement with the data calculated from XRD patterns.

In general, the spheroidal shape of NCs is maintained for the doped ZnO NCs regardless of the doping amount. Exceptions are the samples doped with Tb where different shapes are found (see Fig. 4.7 and 4.8). Particles little more elongated than in the previous cases are the predominant shape.

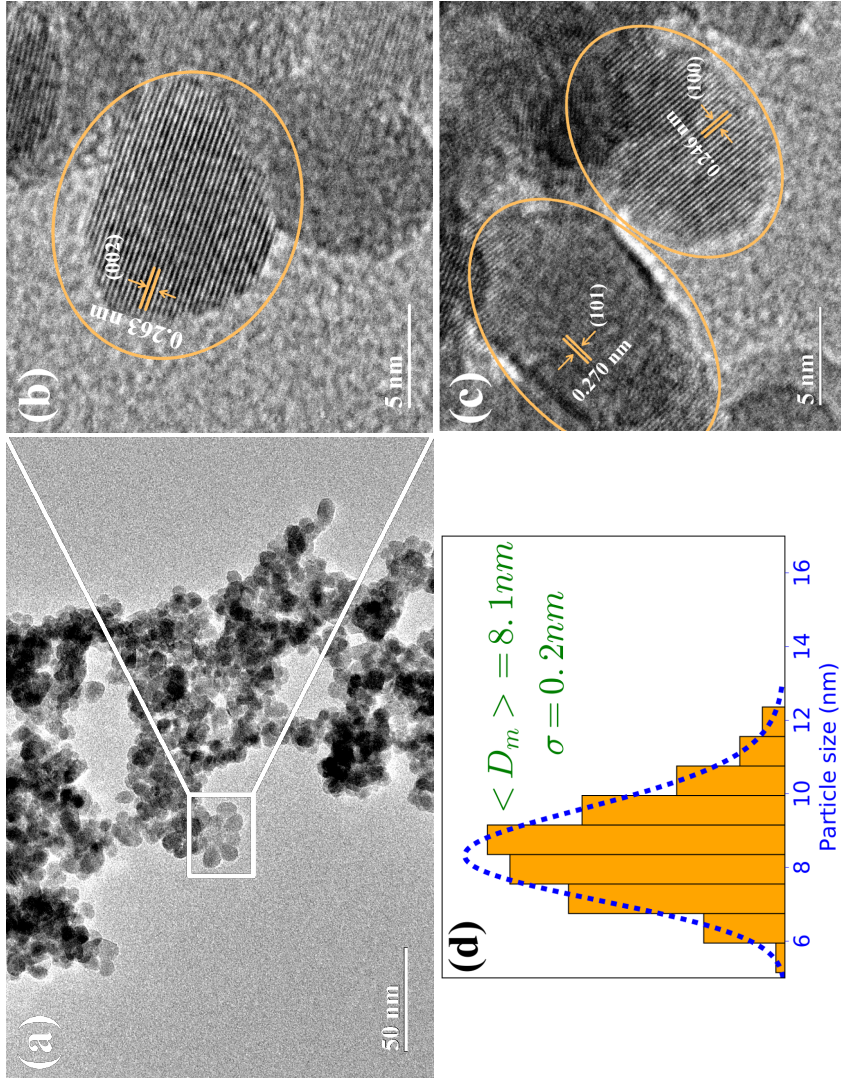


Fig. 4.4 (a) TEM (scale bar: 50 nm), (b, c) high-resolution TEM (scale bar: 5 nm) images of pure NCs and, (d) histogram with the fit to obtain the parameters of the sizes distribution.

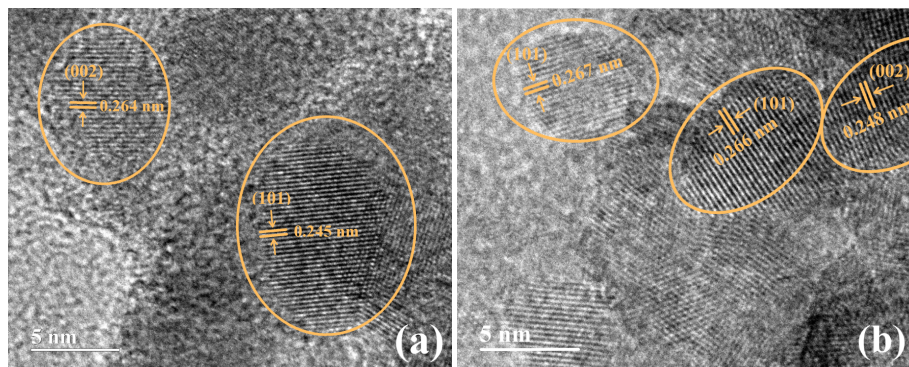


Fig. 4.5 High-resolution TEM (scale bar: 5 nm) images: (a) ZnO:Ni3 and, (b) ZnO:Ni10 samples.

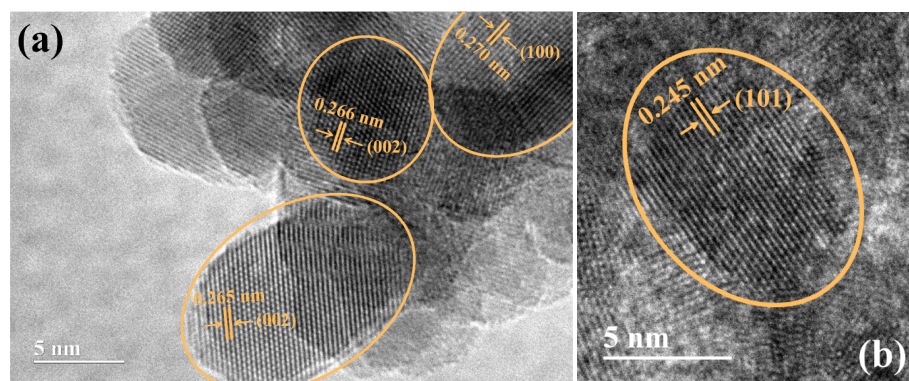


Fig. 4.6 High-resolution TEM (scale bar: 5 nm) images: (a) ZnO:Co3 and, (b) ZnO:Co10 samples.

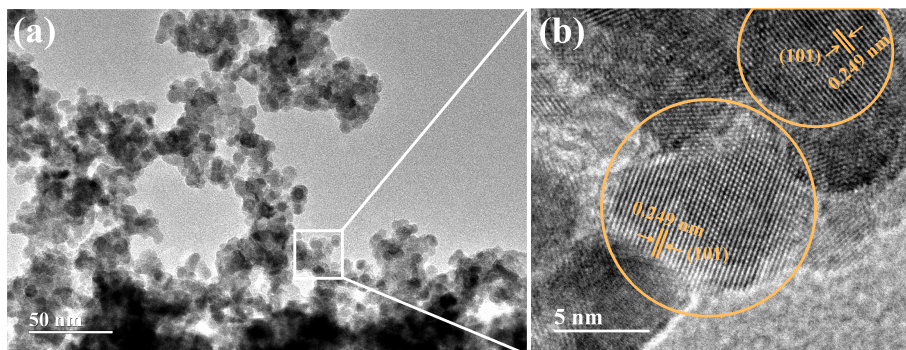


Fig. 4.7 (a) TEM (scale bar: 50 nm) and, (b) high-resolution TEM (scale bar: 5 nm) images of ZnO:Tb3 sample.

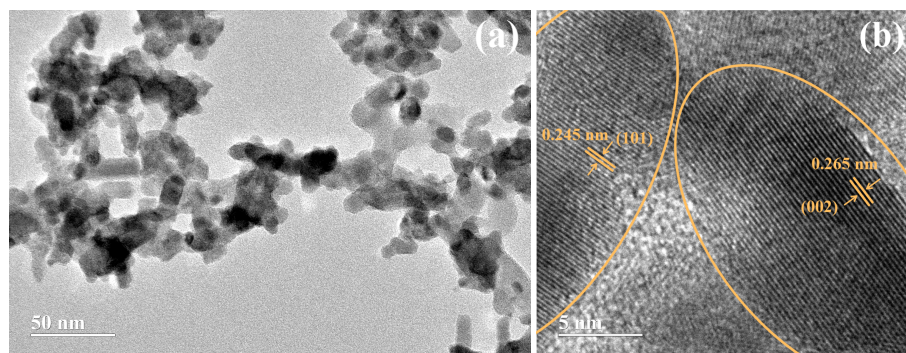


Fig. 4.8 (a) TEM (scale bar: 50 nm) and, (b) high-resolution TEM (scale bar: 5 nm) images of ZnO:Tb10 sample.

4.3 EXAFS Measurements

X-ray absorption fine structure (EXAFS) spectra for Ni-, Co-, and Tb-doped ZnO samples series were measured at the Zn K-edge (9659 eV) using Si(111) and Si(220) channel-cut crystal monochromators in the XAFS1 beamline at the Brazilian Synchrotron Light Laboratory (LNLS). The measurements were performed at room temperature in transmittance detection mode. ZnO standard was also measured as a reference at the Zn K-edge.

4.3.1 Zn K-edge Results

When the size of ZnO becomes nanometer scale, the local structures around Zn are expected to be different from those of the bulk counterpart because of the size effect, structural distortion, and disorder. The local structural properties around the probe atom can be obtained by looking at the oscillations (EXAFS) above the X-ray absorption edge of the probe atom [14]. The maximum and minimum of ZnO EXAFS spectrum oscillations (see Fig. 4.9(a)) match well with those related to ZnO standard, which indicates little structural differences between the pure ZnO NCs and ZnO standard. For doped ZnO samples (see Fig. 4.10, 4.11 and 4.12), it was observed the same overall features in comparison to those spectra of ZnO standard and pure ZnO NCs.

For a detailed analysis of local structure, the $k^2\chi(k)$ signals were Fourier transformed to R-space with a Kaiser-Bessel window in the 3–13 \AA^{-1} k-range, as shown in Fig. 4.9, 4.10, 4.11 and 4.12(c). The first ($R = 1.6\text{\AA}$) and the second peak ($R = 3\text{\AA}$) for the undoped ZnO NCs can be attributed to 4 oxygen and 12 zinc atoms located around a zinc atom, respectively. The intensity of the peaks is mainly related to the number of neighbors. Considering the peak relative to Zn–O contributions, the first oxygen neighbors remain almost unchanged, and both the distance and the intensity are compatible with the presence of tetrahedrally coordinated oxygen atoms around Zn atoms when compare with the ZnO standard (see Fig. 4.9(c)). The decrease in intensity observed for the peak centered at 3 \AA , which is related to the Zn–Zn neighbors, was assigned to the decrease in the number of Zn neighbors around the absorber atom and, therefore, it can be interpreted as the presence of zinc vacancies [15, 16]. A similar trend has been observed in the Zn–Zn contributions for doped ZnO NCs. As previously pointed out, it's attributed to a change in the coordination number of Zn atoms.

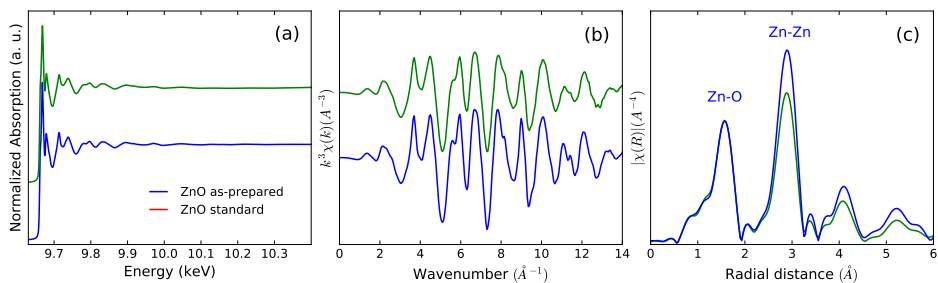


Fig. 4.9 (a) Zn K-edge EXAFS spectra of ZnO NCs and ZnO standard, (b) k^3 -weighted $\chi(k)$ signal and, (c) their respective Fourier transform magnitude spectra.

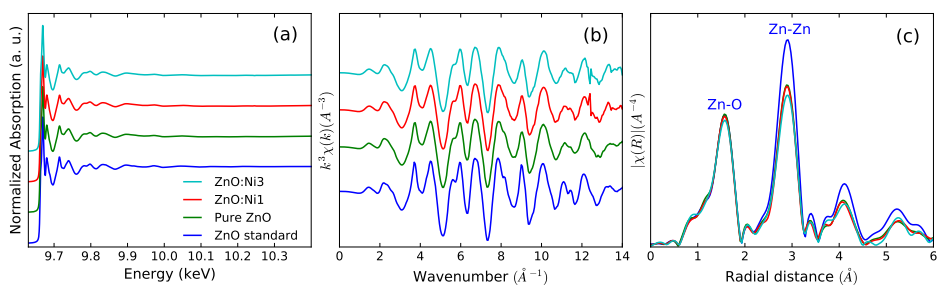


Fig. 4.10 (a) Zn K-edge EXAFS spectra of Ni-doped ZnO NCs, (b) k^3 -weighted $\chi(k)$ signal and, (c) their respective Fourier transform magnitude spectra.

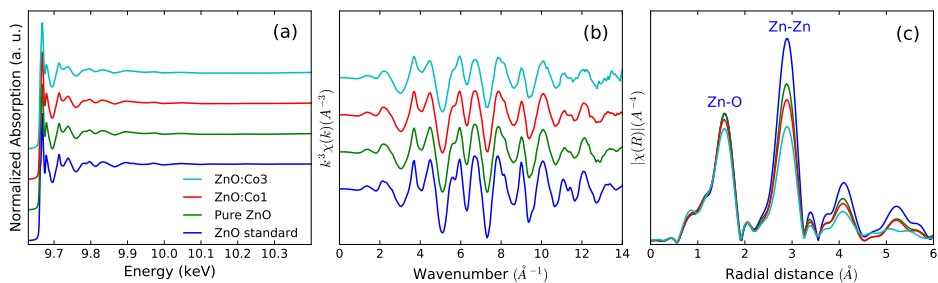


Fig. 4.11 (a) Zn K-edge EXAFS spectra of Co-doped ZnO NCs, k^3 -weighted $\chi(k)$ signal and, (c) their respective Fourier transform magnitude spectra.

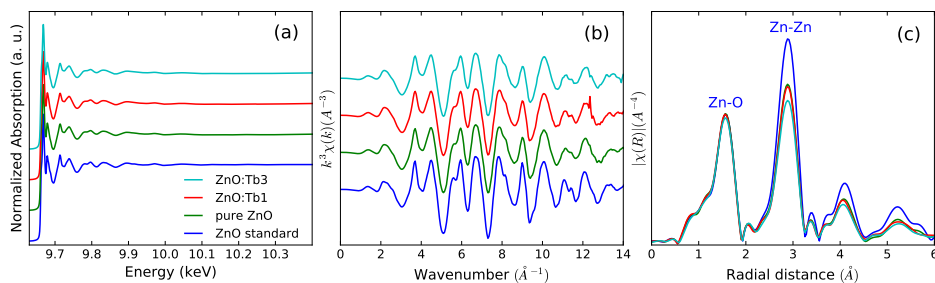


Fig. 4.12 (a) Zn K-edge EXAFS spectra of Tb-doped ZnO NCs, (b) k^3 -weighted $\chi(k)$ signal and, (c) their respective Fourier transform magnitude spectra.

4.3.2 Ni K-, Co K-, and Tb L3-edge Results

For the fits of Zn K-edge EXAFS spectra, the structure is assumed as pure ZnO wurtzite, where Zn is coordinated with four O atoms (Zn–O) at a distance of 1.965 Å in the first shell and the second shell (next nearest-neighbors) of Zn atoms is surrounded by 12 Zn atoms (Zn–Zn) at a distance of 3.208 Å. The fits were performed in phase uncorrected R-space range of 1–3.6 Å. In the fit, the coordination numbers of the different shells, the bonding length (R) and the Debye-Waller factor (σ^2) (which is related to thermal vibration and static disorder of each atomic shell) were fitted as free parameters, whereas the nonstructural parameter E_0 was kept constant for all the paths. Fig. 4.13, 4.14, 4.15, and 4.16 show the best-fit curves for the pure and Ni, Co, and Tb-doped ZnO NCs (with 1 mol% of concentration), respectively, and the best-fit results are summarized in Table 4.2. The results obtained from the fits of Zn K-edge EXAFS curves of the Ni- and Co-doped ZnO NCs reveal that the Zn–O bond distance is slightly increased with the dopant, and the Zn–O bond distance of NCs containing Tb shows a barely perceptible decrease, which agrees well with the results obtained from XRD data analysis. As the ionic radii of Zn^{2+} , Ni^{2+} , and Co^{2+} are almost the same (0.60, 0.55 and 0.58 Å, respectively), the change in bond lengths is insignificant in this case. In addition, there is an increase in the Debye-Waller factor (σ^2) for the Zn–O bond for the Co-doped samples, which indicate an increase in the local disorder in the ZnO lattice near the cation sites due to Co doping. The Debye-Waller factor values of Zn–Zn path, however, do not show any change. There is a decrease in the coordination numbers (CNs) of Zn–Zn shells for Co and Tb doped samples. This confirms that for Co and Tb doping, the number of Zn vacancies is increased around the Zn atoms in the Co- and Tb-doped ZnO NCs.

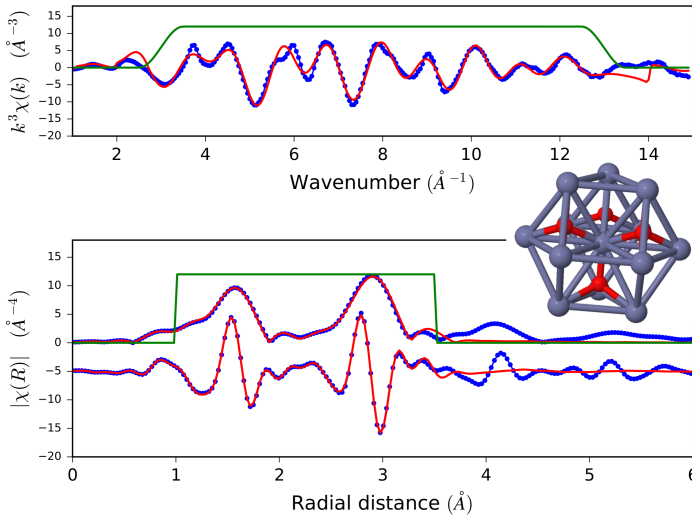


Fig. 4.13 k^3 -weighted $\chi(k)$ signal (top panel) and their Fourier-transformed spectrum (bottom panel) including the real part of $\chi(R)$ for the pure ZnO NCs. Blue dots indicate experimental data and the red solid line is the best-fit curve.

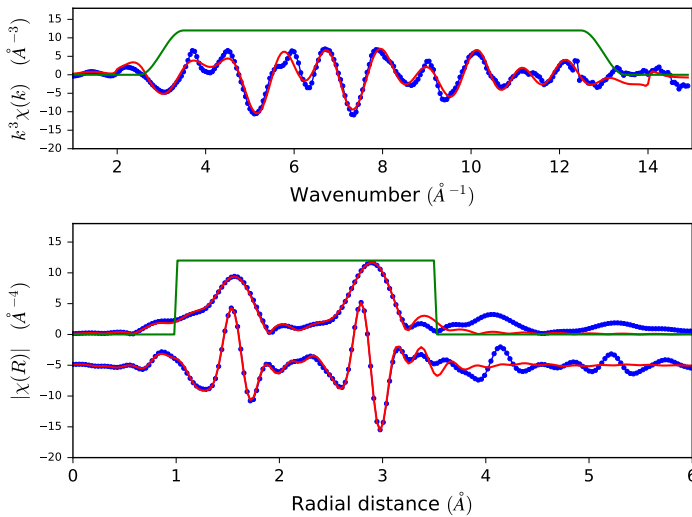


Fig. 4.14 k^3 -weighted $\chi(k)$ signal (top panel) and their Fourier-transformed spectrum (bottom panel) including the real part of $\chi(R)$ for the ZnO:Ni1 sample. Blue dots indicate experimental data and the red solid line is the best-fit curve.

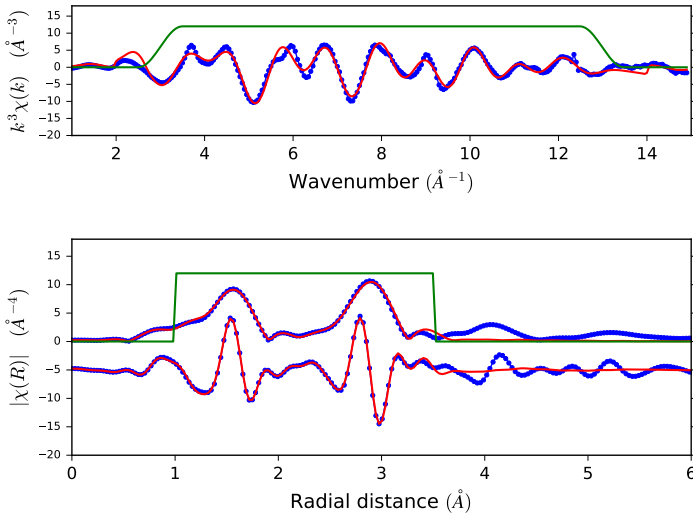


Fig. 4.15 k^3 -weighted $\chi(k)$ signal (top panel) and their Fourier-transformed Spectrum (bottom panel) including the real part of $\chi(R)$ for the ZnO:Co1 sample. Blue dots indicate experimental data and the red solid line is the best-fit curve.

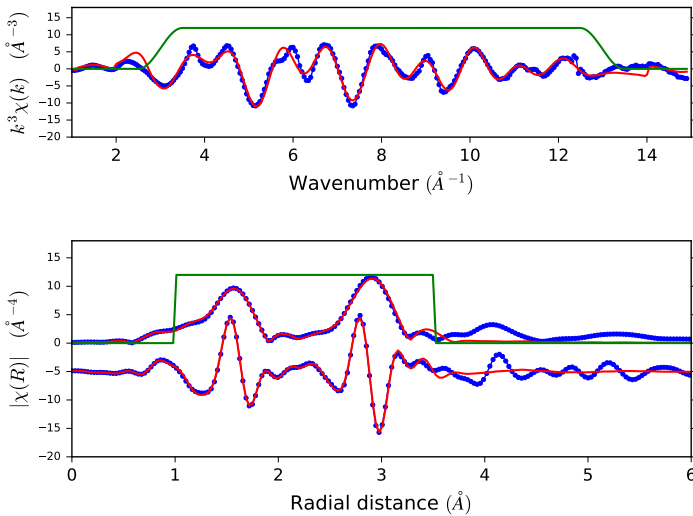


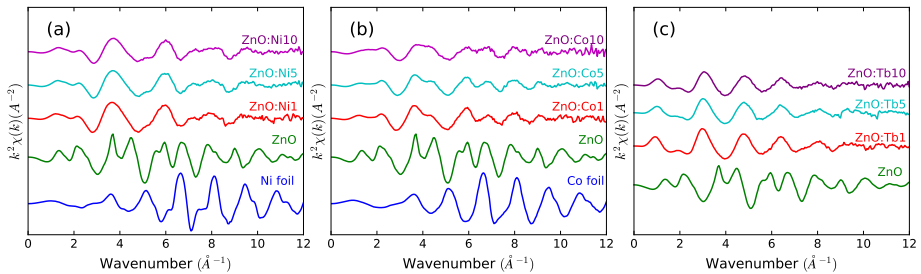
Fig. 4.16 k^3 -weighted $\chi(k)$ signal (top panel) and their Fourier-transformed spectrum (bottom panel) including the real part of $\chi(R)$ for the ZnO:Tb1 sample. Blue dots indicate experimental data and the red solid line is the best-fit curve.

Table 4.2 List of structural parameters obtained from the EXAFS data analysis for Ni-, Co-, and Tb-doped ZnO NCs.

Sample	$A - B_s$ ^(a)	N ^(b)	r ^(c) (Å)	σ^2 ^(d) (Å)	E_f ^(e) (eV)	k-range (Å ⁻¹)	R-factor
ZnO	Zn-O	4.0 (3)	1.949 (5)	0.0039 (8)	3.7 (6)	3-13	0.0030889
	Zn-Zn	15 (2)	3.233 (5)	0.012 (1)			
ZnO:Ni1	Zn-O	3.9 (3)	1.950 (6)	0.004 (1)	3.2 (6)	3-13	0.0038879
	Zn-Zn	14 (2)	3.229 (6)	0.012 (1)			
ZnO:Ni3	Zn-O	3.9 (2)	1.952 (5)	0.0039 (9)	4.0 (6)	3-13	0.0027575
	Zn-Zn	15 (2)	3.233 (6)	0.012 (1)			
ZnO:Co1	Zn-O	4.1 (3)	1.952 (5)	0.0045 (9)	2.5 (6)	3-13	0.0027177
	Zn-Zn	13 (2)	3.227 (6)	0.012 (1)			
ZnO:Co3	Zn-O	4.2 (2)	1.958 (5)	0.0051 (7)	3.0 (5)	3-13	0.0019436
	Zn-Zn	11(2)	3.224 (5)	0.012 (1)			
ZnO:Tb1	Zn-O	4.0 (3)	1.950 (5)	0.0040 (9)	4.0 (6)	3-13	0.0034292
	Zn-Zn	15 (3)	3.232 (6)	0.012 (1)			
ZnO:Tb3	Zn-O	3.9 (2)	1.949 (5)	0.0039 (8)	4.1 (5)	3-13	0.0031027
	Zn-Zn	14 (2)	3.234 (6)	0.012 (1)			

^a A , absorber and b_s , backscatterers; ^b N , coordination number; ^c r , interatomic distance; ^d σ^2 , Debye-Waller factor; ^e E_f , Fermi energy.

The experimental EXAFS signal measured at the Co K-edge (Fig. 4.17(b)) shows features similar to those of the Zn K-edge. This provides further qualitative evidence that Co substitutes Zn atoms in the tetrahedral sites of the host lattice and there is no evidence of other Co phases or metallic Co present in interstitial sites, in agreement with previous reports on Co-doped ZnO thin films [17], nanowires [18], and nanopowders [19]. It's worth mentioning that the Zn K-edge measurements were made in transmittance detection mode. Meanwhile, the Co K-, Ni K-edge, and Tb L3-edge were carried out in fluorescence detection mode and; therefore, the signal-to-noise ratio increase [20].

**Fig. 4.17** k^2 -weighted $\chi(k)$ signals for the Ni-, Co-, and Tb-doped ZnO NCs at the (a) Ni K-edge, (b) Co K-edge and, (c) Tb L3-edge, respectively. Zn K-edge of pure ZnO is included as a reference.

The experimental EXAFS signals at the Ni K-edge and Tb L3-edge (Fig. 4.17(a) and 4.17(c)) show different features compared to those at the Zn K-edge. This suggests changes in the Ni and Tb local surrounding with respect to that determined for the Zn and Co sites. Furthermore, the formation of metallic clusters can be excluded because of the oscillations features differ from that determined for the Ni and Co foils in their $k^2\chi(k)$ spectra [20].

References

1. Allen C Larson and Robert B Von Dreele. GSAS. *Report IAU*, pages 86–748, 1994.
2. Brian H Toby. EXPGUI, a graphical user interface for GSAS. *J. Appl. Crystallogr.*, 34(2):210–213, 2001.
3. Vijayaprasath Gandhi, Ravi Ganesan, Haja Hameed Abdulrahman Syedahamed, and Mahalingam Thaiyan. Effect of cobalt doping on structural, optical, and magnetic properties of ZnO nanoparticles synthesized by coprecipitation method. *J. Phys. Chem. C*, 118(18):9715–9725, 2014.
4. Rafael Pérez-Casero, Araceli Gutiérrez-Llorente, Olivier Pons-Y-Moll, Wilfrid Seiler, Reine Marie Defourneau, Daniel Defourneau, Eric Millon, Jacques Perriere, Philippe Goldner, and Bruno Viana. Er-doped ZnO thin films grown by pulsed-laser deposition. *J. Appl. Phys.*, 97(5):054905, 2005.
5. Marcos Fernández-García and José A Rodríguez. *Metal oxide nanoparticles*. Wiley Online Library, 2011.
6. Sha Wang, Ping Li, Hui Liu, Jibiao Li, and Yu Wei. The structure and optical properties of ZnO nanocrystals dependence on Co-doping levels. *J. Alloys Compd.*, 505(1):362–366, 2010.
7. A Douayar, P Prieto, G Schmerber, K Nouneh, R Diaz, I Chaki, S Colis, A El Fakir, N Hassanain, A Belayachi, et al. Investigation of the structural, optical and electrical properties of Nd-doped ZnO thin films deposited by spray pyrolysis. *The European Physical Journal-Applied Physics*, 61(1):10304, 2013.
8. Jasneet Kaur, RK Kotnala, Vinay Gupta, and Kuldeep Chand Verma. Anionic polymerization in Co and Fe doped ZnO: Nanorods, magnetism and photoactivity. *Curr. Appl. Phys.*, 14(5):749–756, 2014.
9. Lars Vegard. Die konstitution der mischkristalle und die raumfüllung der atome. *Zeitschrift für Physik*, 5(1):17–26, 1921.
10. Mohd Arshad, Ameer Azam, Arham S Ahmed, S Mollah, and Alim H Naqvi. Effect of Co substitution on the structural and optical properties of ZnO nanoparticles synthesized by sol-gel route. *J. Alloys Compd.*, 509(33):8378–8381, 2011.
11. Tahani H Flemban, MC Sequeira, Z Zhang, S Venkatesh, E Alves, K Lorenz, and Iman S Roqan. Identifying the influence of the intrinsic defects in Gd-doped ZnO thin-films. *J. Appl. Phys.*, 119(6):065301, 2016.
12. M Subramanian, P Thakur, M Tanemura, T Hihara, V Ganesan, T Soga, KH Chae, R Jayavel, and T Jimbo. Intrinsic ferromagnetism and magnetic anisotropy in Gd-doped ZnO thin films synthesized by pulsed spray pyrolysis method. *J. Appl. Phys.*, 108(5):053904, 2010.
13. Ghulam Murtaza Rai, Muhammad Azhar Iqbal, Yongbing Xu, Iain Gordon Will, and Wen Zhang. Influence of Rare Earth Ho³⁺ Doping on Structural, Microstructure and Magnetic Properties of ZnO Bulk and Thin Film Systems. *Chinese J Chem Phys.*, 24(3):353, 2013.
14. DC Koningsberger, BL Mojet, GE Van Dorsen, and DE Ramaker. XAFS spectroscopy; fundamental principles and data analysis. *Top. Catal.*, 10(3-4):143–155, 2000.
15. Bruno Leonardo Caetano. *Formação e crescimento de nanopartículas de óxido de zinco via sol-gel*. PhD thesis, Universidade Estadual Paulista (UNESP), 2010.
16. Scott Calvin. *XAFS for Everyone*. CRC press, 2013.

17. G Martínez-Criado, A Segura, JA Sans, A Homs, J Pellicer-Porres, and J Susini. X-ray absorption of $Zn_{1-x}Co_xO$ thin films: A local structure study. *Appl. Phys. Lett.*, 89(6):061906, 2006.
18. Tao Yao, Wensheng Yan, Zhihu Sun, Zhiyun Pan, Yi Xie, Yong Jiang, Jian Ye, Fengchun Hu, and Shiqiang Wei. Magnetic property and spatial occupation of Co dopants in $Zn_{0.98}Co_{0.02}O$ Nanowires. *J. Phys. Chem. C*, 113(32):14114–14118, 2009.
19. Rongliang He, Rosalie K Hocking, and Takuya Tsuzuki. Co-doped ZnO nanopowders: location of cobalt and reduction in photocatalytic activity. *Mater. Chem. Phys.*, 132(2-3):1035–1040, 2012.
20. Gabriele Giuli, Angela Trapananti, Franziska Mueller, Dominic Bresser, Francesco d’Acapito, and Stefano Passerini. Insights into the effect of iron and cobalt doping on the structure of nanosized ZnO. *Inorg. Chem.*, 54(19):9393–9400, 2015.

Chapter 5

Electronic Structure—XPS and XANES Results

In this chapter, the results obtained by X-ray photoelectron spectroscopy (XPS) and X-ray absorption near-edge structure (XANES) are described. The XPS and XANES techniques are presented together as complementary methods in order to have an overall and accurate description of the oxidation states and local environment of the absorbers atoms. Although XPS spectra sometimes is enough to obtain a detailed information of the oxidation states, XANES spectrum—which corresponds to the pre-edge and absorption edge set—provides additional information about local symmetry and oxidation state of the absorber atom. The binding energies related to Zn2p core-level for all the samples are first presented and analyzed, and then the Ni2p, Co2p, and Tb3d core-levels of the dopant ions. In addition, it is also given the results obtained for O1s core-level in order to analyze the oxygen vacancies. Finally, the XANES results are presented for Ni K, Co K, and Tb L3 absorption edges.

5.1 X-ray Photoelectron Spectroscopy

5.1.1 Survey Spectra

The low-resolution XPS survey spectra of the Ni-, Co-, and Tb-doped ZnO NCs are shown in Fig. 5.1—at different concentrations (i.e., 0, 1 and 10 mol%). It is possible to observe the peaks related to the core-levels Zn2p, O1s, C1s as well as Ni2p, Co2p and Tb3d in the case of the samples containing nickel, cobalt, and terbium, respectively. No additional peaks were detected.

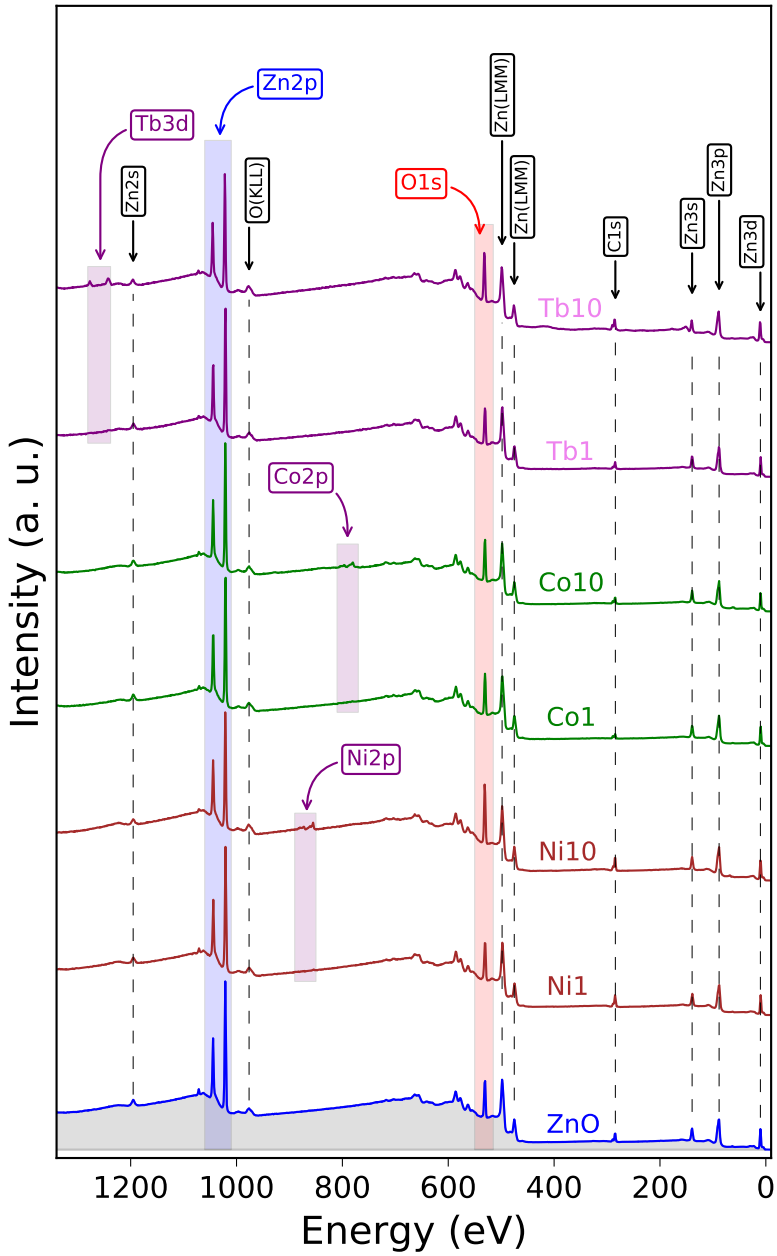


Fig. 5.1 XPS survey spectra of pure and Ni-, Co-, and Tb-doped ZnO NCs (1 and 10 mol%).

The binding energies were corrected for the charging effect with reference to the C1s line located at 284.8 eV. Some authors usually use the position of the main peak to describe the oxidation state of the samples and, an absolute value of binding energy is meaningless without a proper calibration. The Zn2p, Ni2p, Co2p, Tb3d and O1s core-levels peaks are marked with the colored boxes in Fig. 5.1. They are the most important regions to analyze and offer fundamental information related to the chemical composition and oxidation states of ions located at the NCs surface.

5.1.2 Zn2p Core-level

The high-resolution XPS spectra of the Zn2p core-level (blue box region in Fig. 5.1 of undoped and doped ZnO samples are shown in Fig. 5.2. These spectra are characterized by the presence of a doublet due to the spin-orbit coupling effect which splits the Zn2p core-level into two new energy levels namely Zn $2p_{3/2}$ and Zn $2p_{1/2}$.

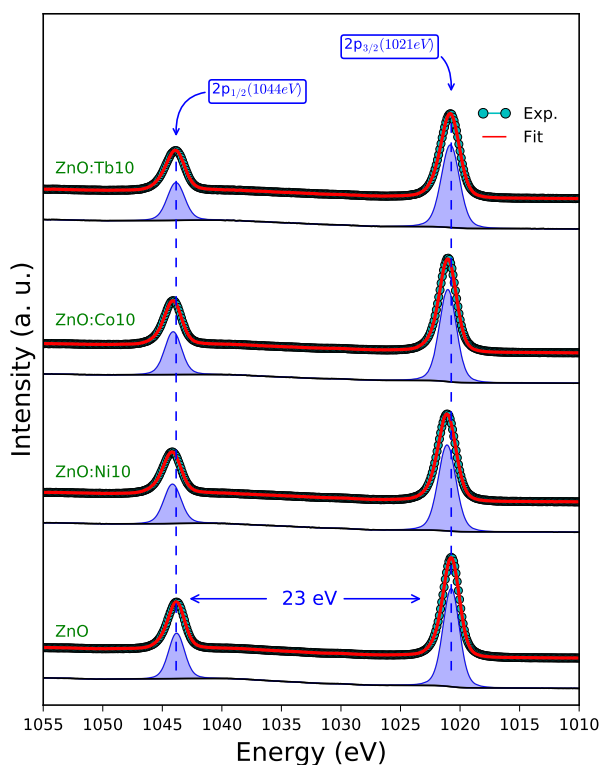


Fig. 5.2 High-resolution XPS spectra of Zn2p core-level for pure and 10 mol% doped ZnO NCs

Table 5.1 Summary of the results obtained from the XPS analysis of pure and doped ZnO NCs.

Zn2p (eV)		Ni2p (eV)		O1s (eV)					
Sample	2p _{3/2}	2p _{1/2}	Sat 1	2p _{1/2}	Sat 2	O1s _(a)	O1s _(b)		
ZnO	1020.74	1043.80	—	—	—	530.02	531.45		
ZnO:Ni1	1021.08	1044.16	855.05	861.11	872.77	878.95	531.08		
ZnO:Ni10	1021.09	1044.15	855.57	861.40	873.20	879.16	530.95		
Zn2p (eV)		Co2p (eV)		O1s (eV)					
Sample	2p _{3/2}	2p _{1/2}	2p _{3/2}	Sat 1	2p _{1/2}	Sat 2	O1s _(a)	O1s _(b)	
ZnO:Co1	1020.86	1043.92	780.57	785.77	796.29	801.52	529.69	531.13	
ZnO:Co10	1021.02	1044.09	780.60	785.39	796.35	802.01	529.78	531.23	
Zn2p (eV)		Tb3d (eV)		O1s (eV)					
Sample	2p _{3/2}	2p _{1/2}	Sat1	Tb3d _{5/2} (3+)	Sat1	Tb3d _{3/2} (3+)	Sat2	O1s _(a)	O1s _(b)
ZnO:Tb1	1021.03	1044.08	1249.33	1240.82	1243.71	1275.49	—	529.78	531.28
ZnO:Tb10	1020.81	1043.86	1249.24	1239.85	1242.60	—	—	529.44	530.91

It can be seen that the peaks are centered at around 1021 eV (Zn $2p_{3/2}$) and 1044 eV (Zn $2p_{1/2}$) and the separation energy between the peaks is around 23 eV. These values are in good agreement with the reported values for zinc oxide [1]. The Table 5.1.2 resume the position peaks of the doublets obtained through the deconvolution using Gaussian-Lorentzian peak shape and after subtracting from the Shirley background.

5.1.3 Ni2p and Co2p Core-levels

The oxidation state of Ni and Co cations in ZnO NCs were examined by high-resolution XPS spectra as shown in Fig. 5.3 and 5.5, respectively. The Co2p and Ni2p levels show four peaks, a doublet—due to the spin-orbit coupling effect—and its corresponding satellites related to the “shake up” process, located at slightly higher energies. The nature of the electronic process responsible for the satellites corresponds to $O2p \rightarrow 3d$ charge transfer excitation and different transition-metal oxides may present these satellite peaks as described elsewhere [2]. In addition, Ni2p and Co2p peaks shift to higher binding energy, which is usually related to the doping effect. The dopant leads to the change of electron cloud around Ni and Co atoms and the increase of $2p_{3/2}$ and $2p_{1/2}$ binding energies. Different binding energies are usually associated to the same peak in the vast literature and, although our results were properly calibrated, we believe that the energy difference between $2p_{3/2}$ and $2p_{1/2}$ levels is a better way to determine changes in the oxidation state instead of only considering the energy value of a single XPS peak.

The peaks related to Ni $2p_{3/2}$ and $2p_{1/2}$ core-levels are found to be centered at 855.3 eV and 873.0 eV, respectively, whereas the corresponding satellite peaks (sat1 and sat2) are observed at 861.3 and 879.1 eV (see Fig. 5.3), which are comparable to the results reported in the literature [3, 4]. The Ni $2p_{3/2}$ core-level position (855.05–855.57 eV) is different from that of metallic Ni (852.5–853.1 eV), NiO (854.0–854.9 eV) and Ni₂O₃ (855.7–857.1 eV) [5–7]. The absence of Ni metallic clusters can also be explained on the basis of the energy difference between Ni $2p_{3/2}$ and $2p_{1/2}$ core-levels. For the Ni-doped ZnO NCs we found a difference of 17.70 eV, which is different from the value reported for metallic Ni (17.27 eV) [7] and Ni₂O₃ (18.39 eV) [8]. In addition, the peaks shape for Ni metal with satellites structure is narrow and different from that observed for the Ni-doped ZnO NCs in this work. The energy difference reported for NiO (17.49 eV) [7] is very close to the observed value (17.70 eV). This result evidences that Ni ions are mostly in 2+ oxidation state in our samples. Considering the similar results of Ni-doped ZnO samples with other reported works, it is probably that the Ni²⁺ ions are substituting at least partially the Zn²⁺ ions in the ZnO NCs.

The peaks related to Co $2p_{3/2}$ and $2p_{1/2}$ core-levels are centered at 780.6 and 796.3 eV, respectively, whereas the corresponding satellite peaks (sat1 and sat2) are observed at 785.6 and 801.8 eV (see Fig. 5.5 and Table 5.3). The spin-orbital splitting energy of 15.7 eV between the transitions $2p_{3/2}$ and $2p_{1/2}$ is larger than that value reported for Co metal (15.06 eV) [7]. Therefore, the formation of Co metal cluster in

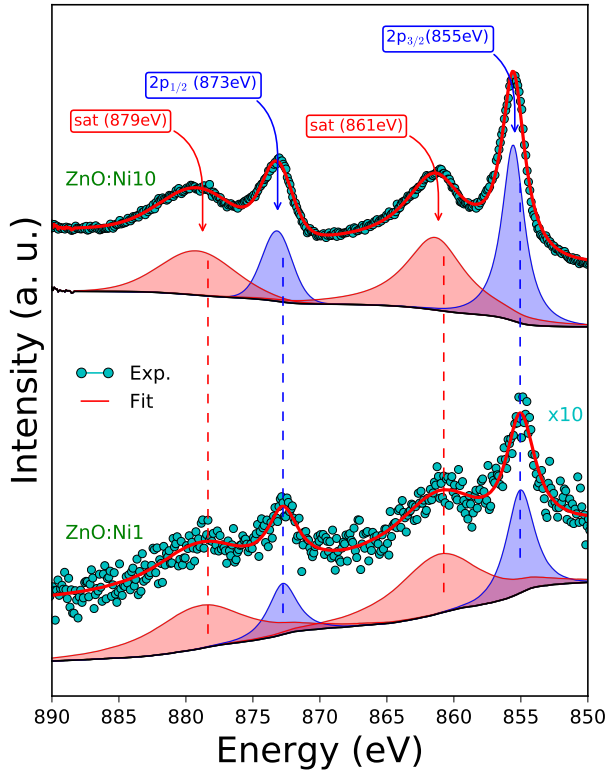


Fig. 5.3 High-resolution XPS spectra of Ni2p core-level of 1 and 10 mol% Ni-doped ZnO NCs.

our samples can be ruled out [9]. It is expected that if Co is surrounded by oxygen, the difference should be around 15.5 eV [6]. Although, the valence of Co is not easily determined by XPS measurements, the energy difference (15.7 eV) between the two binding energies of Co 2p_{3/2} and 2p_{1/2} agrees with values reported in the literature for Co:ZnO, Co₃O₄ (2+/3+ valence state) and CoO (2+ valence state) [10–12] and sometimes is indicated as a characteristic of the Co²⁺ ions [13, 14].

Moreover, the similar values of binding energies for Co₃O₄ and CoO makes it difficult to identify the Co state via XPS experiments in the samples. According to Hao et al. [15], Co²⁺ and Co³⁺ oxides can be differentiated via XPS experiments using their different magnetic properties. Compounds with Co²⁺ ions, which show a high-spin configuration [16, 17], such as in CoO compound, are characterized by two shake-up satellite peaks located at higher binding energies (787.0 and 804.0 eV), as shown in Table 5.3. However, in compounds containing Co³⁺ ions, which show low-spin states, the satellite structure is weak or missing [18, 19]. Co₃O₄, a mixed-valence oxide, shows a weak satellite structure symptomatic of the shake-up from the Co²⁺ components. The Co₂O₃ (3+ valence state) spectrum is practically identical to that of Co₃O₄ [5]. Therefore, the results revealed that Co²⁺ ions mainly substitute Zn ions in the ZnO.

The formation of also the CoO phase is not excluded and the presence of Co ions in interstitial sites is less probable since interstitial Co ions are expected to be in low-spin states [20, 21].

Table 5.2 List of XPS peak positions (in eV) obtained for the Ni-doped ZnO NCs. Peak positions of other nickel compounds reported in the literature are included.

Sample	Ni 2p _{3/2} (eV)	sat 1 Ni 2p _{3/2} (eV)	Ni 2p _{1/2} (eV)	sat 2 Ni 2p _{1/2} (eV)
ZnO:Ni1	855.05	861.11	872.77	878.95
ZnO:Ni10	855.57	861.40	873.20	879.16
Ni metallic Refs. [5, 7, 22, 23]	852.5, 852.9, 853.1, 852.7			
NiO (2+) Refs. [5, 8, 22–26]	854, 854.5, 854.9	861.0		
Ni ₂ O ₃ (3+) Refs. [8, 22–24, 26]	855.68, 855.9, 855.8, 857.1, 855.5	861.4	874.07	
Ni(OH) ₂ (2+) Refs. [5, 22, 26, 27]	856.9, 855.6, 856.6	862.5		

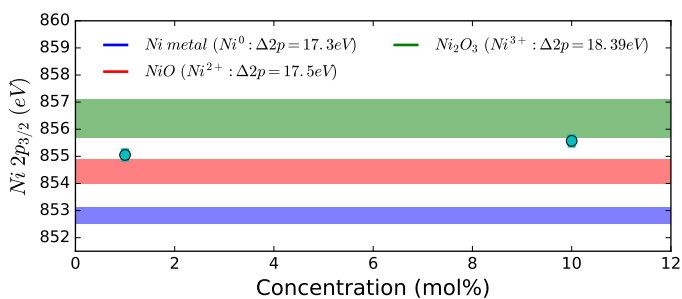


Fig. 5.4 Figure for better visualization of the Ni 2p_{3/2} XPS peak positions reported in the Table 5.2.

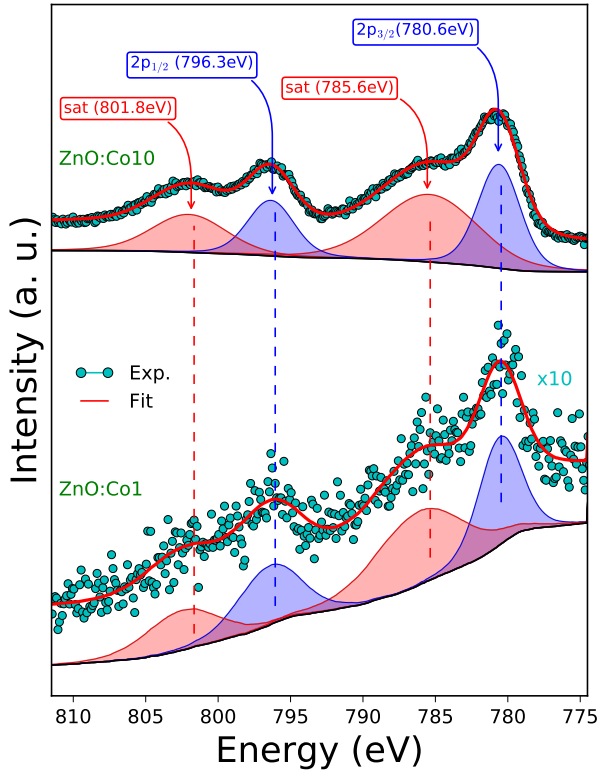


Fig. 5.5 High-resolution XPS spectra of Co_{2p} core-level of 1 and 10 mol% Co-doped ZnO NCs.

Table 5.3 List of XPS peak positions (in eV) obtained for the Co-doped ZnO NCs. Peak positions of other cobalt compounds reported in the literature are included.

Sample	Co2P _{3/2} (2+) (eV)	sat 1 Co2P _{3/2} (2+) (eV)	Co2P _{3/2} (3+) (eV)	Co2p _{1/2} (2+) (eV)	sat 2 Co2p _{1/2} (2+) (eV)	Co2p _{1/2} (3+) (eV)
ZnO:Co1	780.57	785.77		796.29	801.52	
ZnO:Co10	780.60	785.39		796.35	802.01	
Co metallic Refs. [5, 28]	778.0, 778.30					
CoO (2+) Refs. [16, 17, 29, 30]	780.4, 781.1, 780.5	787.0, 787.3, 786.4		796.0, 796.2, 796.3	804.0, 802.5, 803.0	
Co ₂ O ₃ (3+) Refs. [5, 31]			779.9, 780.0,			797.1
Co ₃ O ₄ (2+/3+) Refs. [10, 16, 29, 32, 33]	780.0, 780.3, 780.7	789.3, 789.5	779.6	795.4, 796.0	804.9, 804.5	794.5

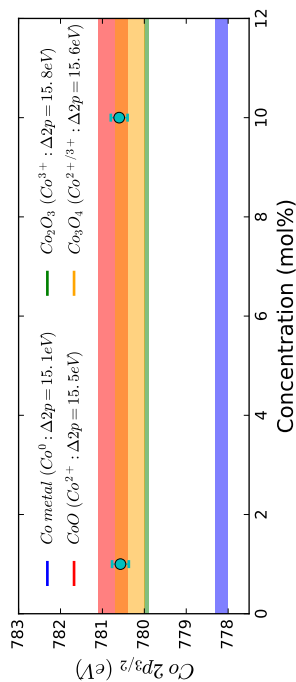


Fig. 5.6 Figure for better visualization of the Co 2p_{3/2} XPS peak positions reported in the Table 5.3.

5.1.4 Tb 3d and 4d Core-levels

To identify the oxidation state of Terbium ions, we studied the Tb3d core-levels ($3d_{5/2}$ and $3d_{3/2}$ doublet) that appear at high binding energies (between 1230 and 1290 eV). In Fig. 5.7 is shown the high-resolution spectrum of the Tb3d core-level. We observe some differences between the samples at concentrations of 1 and 10 mol% Tb. For the sample doped with 1 mol% Tb, the peak located at 1240.82 eV with a satellite peak at 1249.33 eV was assigned to the $3d_{5/2}$ core-level of Tb^{3+} ions [34, 35]. The additional peak located at 1275.49 eV was related to the $3d_{3/2}$ core-level of Tb^{3+} ions. The position of these peaks is shifted from those ones published for pure $TbO_{1.5}$ (Tb^{3+}) (see Table 5.4), where the Tb $3d_{5/2}$ and Tb $3d_{3/2}$ peaks are located at about 1239.1 and 1274 eV [36]. Moreover, in the sample doped with 10 mol% Tb, the additional peak centered at 1243.71 eV suggests the presence of Tb^{4+} ions. Terbium in the 3+ state shows relatively intense satellite peak near to the Tb $3d_{5/2}$ component at 1249.33 eV [37, 38]. As shown in Fig. 5.7, the broad $3d_{5/2}$ peak observed in the XPS spectrum of the sample ZnO:Tb10 can be deconvoluted into two peaks located at 1239.85 and 1242.6 eV. Some authors have reported that the latter peak might be caused by the oxidation of Tb^{3+} into Tb^{4+} when the sample is hit with high-energy photoelectrons [39].

The next most intense core-level (Tb4d region) was also analyzed. The characteristics of the XPS peaks of the Tb4d core-levels are important features to distinguish the valence state condition of Tb ions [34]. The spin-orbit splitting of Tb4d is too small to be resolved by a laboratory instrument; therefore, a single asymmetric line would be expected if a single oxidation state was present. It is expected that Tb^{3+} ions exhibit a single XPS line below 150 eV and Tb^{4+} ions show some features well above 150 eV. Generally, both Tb^{3+} and Tb^{4+} ions show two strong photoelectron peaks at 150 and 157 eV, respectively [40]. In Fig. 5.8 is shown the XPS spectrum of the Tb4d core-level region. As observed, a pronounced shoulder located at 149.8 eV and a broad peak near 155.8 eV is observed. The sharp peak located at 139.1 eV corresponds to the Zn3s core-level and was used as a reference to improve the fit. The additional peak positioned at 175.2 eV appears just in this sample and was not identified in the literature. We believe, according to the strong evidence of the presence of Tb^{4+} ions, that this peak is also related to Tb^{4+} ions. Then, we can conclude that the surface of the 10 mol% Tb-doped ZnO NCs contains the Tb ions in both 3+ and the 4+ valence states.

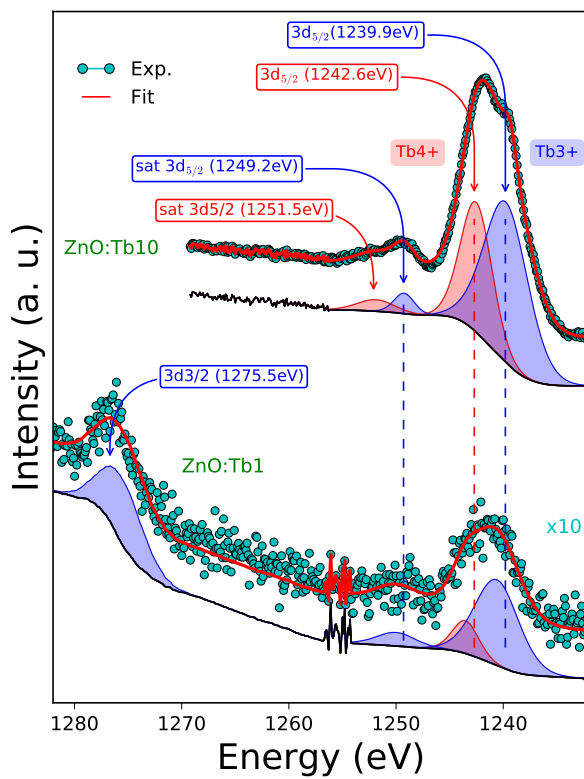


Fig. 5.7 High-resolution XPS spectra of Tb3d core-level of 1 and 10 mol% Tb-doped ZnO NCs

Table 5.4 List of XPS peak positions (in eV) obtained for the Tb-doped ZnO NCs. Peak positions of some other terbium compounds reported in the literature are included for comparison.

Sample	Peak 1 Tb $3d_{5/2}$ (3+) (eV)	Sat 1 Tb $3d_{5/2}$ (3+) (eV)	Peak 1 Tb $3d_{5/2}$ (4+) (eV)	Sat 1 Tb $3d_{5/2}$ (4+) (eV)	Peak 2 Tb $3d_{3/2}$ (3+) (eV)	Sat 2 Tb $3d_{3/2}$ (3+) (eV)	Peak 1 Tb $3d_{3/2}$ (4+) (eV)	Sat 1 Tb $3d_{3/2}$ (4+) (eV)
ZnO:Tb1	1240.82	1249.33	1243.71	—	1275.49	—	—	—
ZnO:Tb10	1239.85	1249.24	1242.60	1251.49	—	—	—	—
Tb ₂ O ₃ (3+) [39]	1241.2	—	—	—	1275.0	—	—	—
TbO _{1.5} (3+) [39]	1239.1	1250.4	—	—	1274	1286.3	—	—
TbO _{1.82} (4+) [39]	—	—	1241.4	1251.4	—	—	1276	1287.7

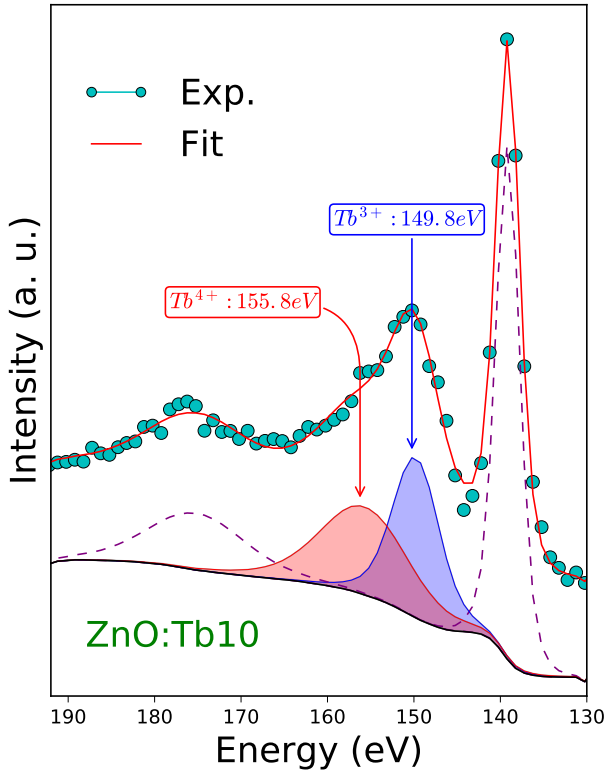


Fig. 5.8 XPS spectrum of Tb4d core-level of ZnO:Tb10 sample.

5.1.5 O1s Core-level

To identify the point defects in Ni-, Co-, and Tb doped ZnO samples, the region of the O1s core-level of all samples was also analyzed in a high resolution. The Fig. 5.9 shows the normalized high-resolution XPS spectra of O1s core-level fitted by two Gaussian-Lorentzian components. The spectra suggest the presence of two oxygen species [41, 42], named O1s_(a) and O1s_(b). Oxygen atoms attached to transition metals have binding energy in the range 529–530 eV. Therefore, we can assign the component O1s_(a) centered at around 529.7 eV to the structural oxygens ions bound to metal cations (i.e., Zn²⁺, or Co²⁺ or Ni²⁺) occupying substitutional sites in the wurtzite structure of ZnO. On the other hand, the second component O1s_(b) at higher binding energy approximately at 531.2 eV has been associated with weak bonds of OH species and carbonate species present on the surface of the material [43–46]. However, this second peak can also be attributed to oxygen vacancies present on the surface of the material or to oxygen-deficient regions within the ZnO matrix according to the literature [47, 48].

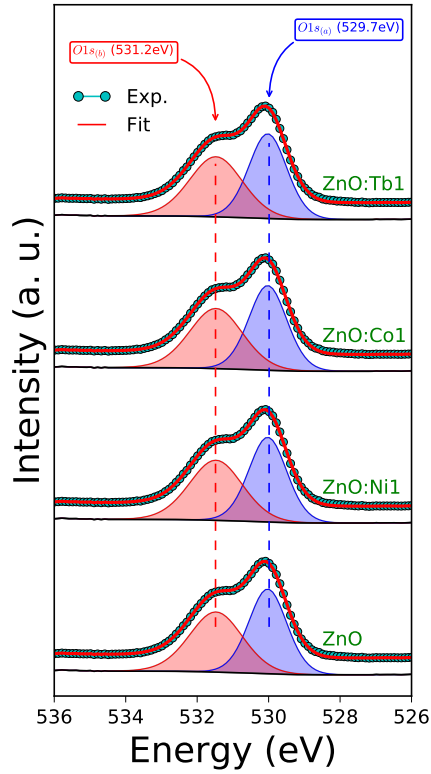


Fig. 5.9 O1s core-level XPS spectra of pure and doped ZnO NCs.

5.1.6 XPS Concentrations

In order to assess the dopant content (C_x) of $Zn_xM_{1-x}O$ (M: Ni, Co or Tb) NCs, the spectral area of Zn and dopant ions were used according to the formula:

$$C_x = (I_x/S_x) / (\sum I_i/S_i) \quad (5.1)$$

here I_x and S_x represent the XPS spectral area and the sensitivity factor (RSF) of the dopant element, respectively, and $(\sum I_i)/S_i$ denotes the sum of the ratios of the XPS spectral area to the sensitivity factor considering all cations in the sample. In this calculation, Zn and dopant ions are taken into account; meanwhile, the oxygen anion is completely ignored. For example, in the Ni-doped ZnO sample with nominal Ni concentration of 10 mol%, the spectral area and RSF for Ni2p (Zn2p) are 209289.6 (2244393.4) and 22.18 (28.72), respectively. Then, Ni concentration is determined to be 9.5 ± 0.3 at%. This value is consistent with the nominal one and confirms the dopant content in our samples. In Table 5.5 are listed the values used to calculate the dopant

concentration via XPS experiments for all of the studied samples. The accordance between the nominal and XPS dopant concentration means that low-temperature sol-gel synthesis is an effective method to doped ZnO NCs [49].

Table 5.5 Comparison between the nominal and experimental concentrations obtained via XPS measurements.

Sample	Nominal concentration (mol%)	Experimental concentration (at%)	XPS Area dopant	XPS Area Zn2p
ZnO:Ni	1	1.0 (2)	17871.1	2196869.8
	10	9.5 (3)	209289.6	2244393.4
ZnO:Co	1	1.1 (2)	13728.4	1820331.6
	10	9.7 (3)	119227	1671079.8
ZnO:Tb	1	1.01(14)	28043.2	1597523.9
	10	—	—	—

*Sensitivity factors (RSF); Ni: 22.18, Co: 19.16, Tb: 49.42 and Zn: 28.72

5.2 XANES Measurements

The XANES spectra at the Ni K (8333 eV), Co K (7709) and Tb L3-edge (7515 eV) were performed at 300 K in fluorescence detection mode in backscattering geometry. As described in detail in Chap. 3, the APPLE-II undulator and a double—Si-(111)—crystal monochromator were used to collect the spectra. Reference samples were also measured at different edges: Ni metallic foil, NiO, Ni(CH₃CO₂)₂ and LaNiO₃ measured at the Ni K-edge; Co metallic foil, CoO, Co₂O₃, Co₃O₄, and CoAl₂O₄ measured at the Co K-edge; and, Tb₂O₃ and Tb₄O₇ measured at the Tb L3-edge.

5.2.1 Co K-edge Results

We have employed Co K-edge XANES to obtain the oxidation state and local geometry of Co dopant in the lattice. This is because Co K-edge XANES has the advantage of good sensitivity and a large chemical shift between the onset of the absorption for Co⁰ and Co²⁺, so that the higher the oxidation state, the greater the energy from the absorption edge. Co K-edge XANES spectra of Co-doped ZnO NCs (with 1 and 3mol%) and reference materials are shown in Fig. 5.10. In this case, the CoO, Co₂O₃, and Co₃O₄ compounds were used as references where Co atoms are present in different oxidation states 2+, 3+ and 2+/3+, respectively. The plateau at $E_0 = 7708.8$ eV in the Co metal spectrum is characteristic of Co⁰ and can be effectively used to determine the presence of Co metal. This plateau is different from the small feature observed in the spectrum of ZnO:Co samples which will be discussed later. Therefore, it is clear that the plateau near the threshold associated with Co⁰ is absent in the spectra of Co:ZnO samples,

as well as in the reference compounds. On the other hand, the absorption edge of Co metal poorly matches the absorption edge of Co:ZnO samples because of the much lower threshold energy corresponding to the Co^0 . Thus, there is no detectable Co^0 in Co-doped ZnO NCs. The spectra presented in Fig. 5.10(b) shows that the absorption edge of the Co-doped ZnO sample is strongly shifted from the absorption edge of Co_2O_3 , which exclude the presence of Co^{3+} oxidation state in our samples. The absorption edge of Co_3O_4 is slightly shifted from our sample and is superimposed to the line of the standard CoO. The Co_3O_4 cubic-centered structure (space group $\text{Fd}\bar{3}\text{m}$) has the Co^{2+} and Co^{3+} ions distributed in the tetrahedral and octahedral sites and, in the rock-salt CoO (space group $\text{Fm}\bar{3}\text{m}$), the Co^{2+} ions occupy octahedral sites [50]. Then, this result confirms that the Co atoms assume predominantly the 2+ valence state in the Co-doped ZnO NCs, which is in agreement with the XPS spectra analysis.

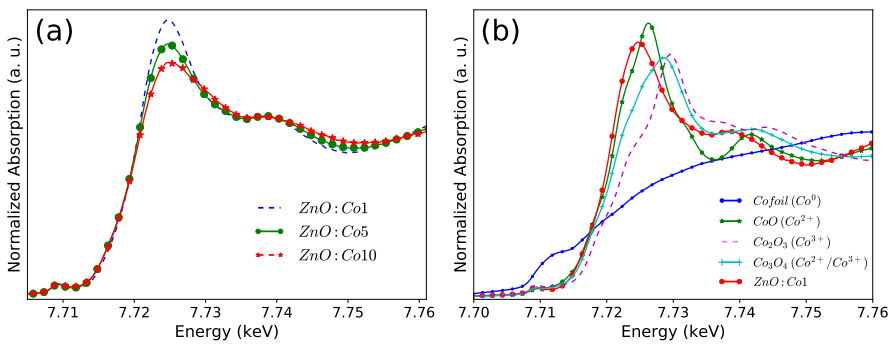


Fig. 5.10 (a) Co K-edge XANES spectra for Co-doped ZnO NCs and, (b) Co K-edge XANES spectra of ZnO:Co1 sample and some reference compounds.

The obvious difference in the XANES spectra between Co:ZnO samples and CoO indicates that the local geometry of Co ions is different. A crucial role for the analysis of the absorption edge is played by the intensity of the pre-edge feature of the XANES spectra, which is more pronounced for Co in its 2+ state, while its intensity is reduced for Co^{3+} and turns into a shoulder for Co metal. This pre-edge peak is due to electron transitions from the occupied 1s to unoccupied 3d states that becomes partially dipole allowed when Co is coordinated to O ligands and $\text{Co}3\text{d}/\text{O}2\text{p}$ mixing occurs in low-lying conduction-band states [51]. Its intensity depends on the local symmetry of the Co ion. Compounds with cobalt ions in tetrahedral coordination will exhibit higher intensity in the pre-edge region in comparison to cobalt ions in octahedral coordination where this transition is rarely observed due to its centrosymmetric position. In Fig. 5.11 we show the pre-edge peak of the sample ZnO:Co1 along with the spectra of two standard samples (i.e., CoO and CoAl_2O_4). In these compounds, the Co ions have the same oxidation state (2+) but occupy different coordination sites: octahedral and tetrahedral sites, respectively. The pre-edge peak in the CoAl_2O_4 compound wherein Co occupies tetrahedral sites exhibits higher peak intensity than in CoO wherein Co occupies octahedral sites. It can be seen from Fig. 5.11(c) that in the CoAl_2O_4 com-

pound, where the Co^{2+} atoms are tetrahedrally coordinated by aluminum and oxygen atoms the transition from the pre-edge is more pronounced when compared with the transition in CoO compound as shown in Fig. 5.11(b), where Co atoms present the same oxidation state (2+) but in octahedral coordination. This result suggests that the cobalt ions in Co-doped ZnO NCs replace Zn^{2+} ions located in tetrahedrally coordinated sites. Considering the EXAFS analysis of the previous chapter and the XANES results here, we can clearly conclude that the Co^{2+} ions substitute Zn^{2+} ions.

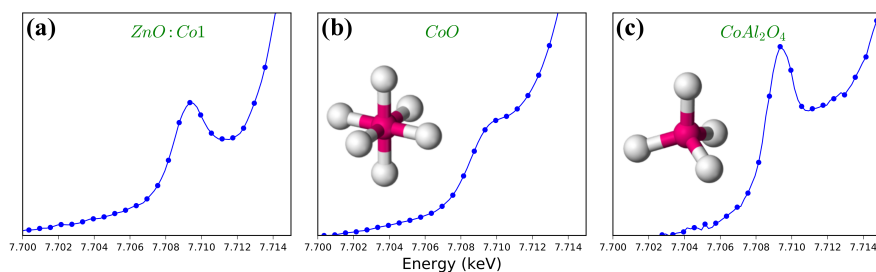


Fig. 5.11 Pre-edge peak features of (a) 1 mol% Co doped ZnO, (b) CoO (Co^{2+} , 6-fold coordination) and, (c) CoAl_2O_4 (Co^{2+} , 4-fold coordination)

5.2.2 Ni K-edge Results

Fig. 5.12 shows the XANES spectra at the Ni K-edge for the Ni-doped ZnO NCs and some reference compounds. The main peak is assigned to the Ni $1s \rightarrow 4p$ dipole transitions. The absorption edge of Ni metal ($E_0 = 8332$ eV) poorly matches the absorption edge of Ni-doped ZnO NCs; thus, there is no detectable Ni^0 in our Ni-doped ZnO NCs. The referred plateau in the Ni foil is different from the small pre-edge peak attributed to $1s \rightarrow 3d$ photoexcitation which, while ideally forbidden, finds relaxed angular selection rules due to $\text{O}2p\text{-Ni}3d$ hybridization [52]. The spectra presented in Fig. 5.12(b) shows that the absorption edge of the ZnO:Ni1 sample shows lower threshold energy than the absorption edge of LaNiO_3 , and very close to those of NiO and $\text{Ni}(\text{CH}_3\text{CO}_2)_2$ used as references. These results exclude the presence of Ni^{3+} ions in our samples and suggest the presence of Ni^{2+} ions. The similarities and differences between the results of Ni-doped ZnO NCs and the references do not permit to identify the presence of secondary phases. The most interesting feature of the pre-edge peak could be the dependence on the coordination symmetry as also indicated in the analysis of Co-doped samples. Group theory predicts that the intensity of ions occupying sites with tetrahedral symmetry is much greater than that expected for ions occupying octahedral sites. The pre-edge feature of the Ni-doped samples shows a reduced intensity peak when compared with compounds where Ni ions occupy tetrahedral coordination sites, but the intensity is comparable with those compounds where Ni ions occupy octahedral coordination sites. T. Yamamoto [53] made a detailed study of this behavior with nickel compounds. NiO and $\text{Ni}(\text{CH}_3\text{CO}_2)_2$ are compounds in which the Ni atoms are

in six-fold coordination. The comparable intensity of the pre-edge peak with those intensities obtained for six-fold coordinated compounds and the nearby absorption edge with some reference compounds (see inset Fig. 5.12(b)) suggest that in our samples the Ni ions are positioned mostly in octahedral sites with 2+ oxidation state.

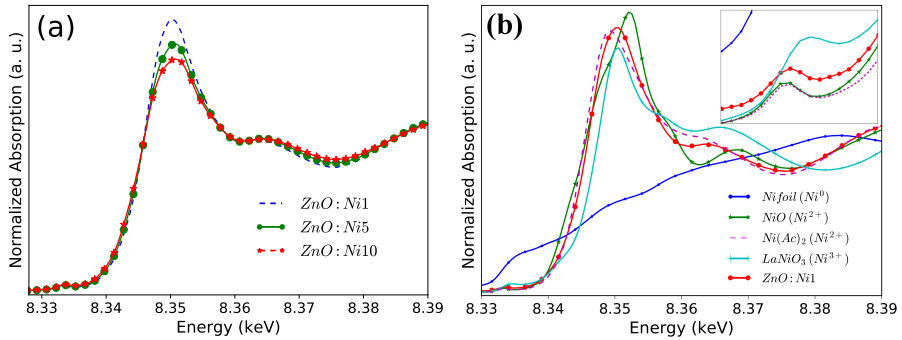


Fig. 5.12 (a) Ni K-edge XANES spectra of Ni-doped ZnO NCs and, (b) Ni K-edge XANES spectra of ZnO:Ni1 sample and some reference compounds.

5.2.3 Tb L3-edge Results

Fig. 5.13 shows the XANES spectra at the Tb L3-edge of the Tb-doped ZnO samples and some reference compounds. In Fig. 5.13(a) one can note that there is a variation in the absorption edge intensity (denoted as peak A) and intensity of peak B. There is a huge drop in the intensity of peak A when compared with the Ni and Co XANES spectra (see Fig. 5.10 and 5.12). The variation in the absorption edge intensity suggests that there is an important change in the number of vacancies/holes around the dopant ions due to the increasing content of terbium and this number must be larger than that of samples containing Ni and Co. An important fact to determine the oxidation state of the Tb ions in our samples is that the rare earths have a characteristic XANES spectra for 3+ and 4+ oxidation states. In Fig. 5.13(b), we had shown two reference compounds with different oxidation state. The Tb_2O_3 compound with the trivalent state shows only a high absorption peak. The electronic configuration of Tb^{3+} is $[\text{Xe}]4f^8$ and it changes its valence state to tetravalent by losing one 4f electron. The binding energy of the 2p electrons in the trivalent state differs by 8–10 eV from the tetravalent state in rare earth elements because of the difference in the number of 4f electrons. As a result, two absorption peaks near the L3 edge of Tb appear for Tb^{4+} ions. The Tb_4O_7 XANES spectrum show this behavior. The energy difference between the two absorption peaks is about 8.4 eV which correspond to the transition from the 2p to the 5d level in the Tb ion [54].

The XANES spectra for ZnO:Tb samples cannot be reproduced without considering both characteristic peaks of Tb^{3+} and Tb^{4+} (features A and B, respectively). Then, the

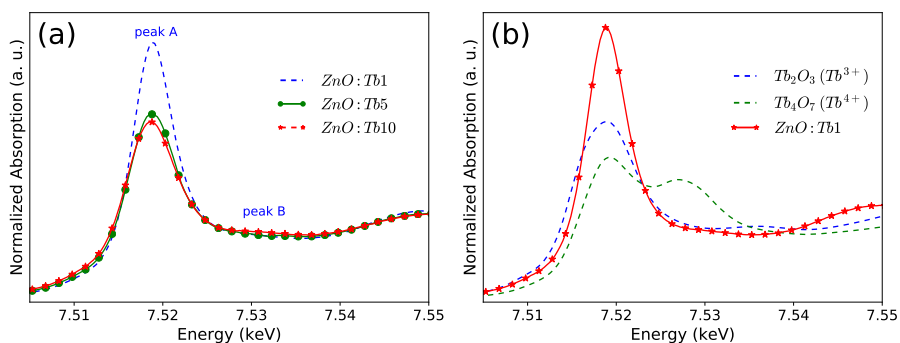


Fig. 5.13 (a) Tb L3-edge XANES spectra of Tb-doped ZnO NCs and, (b) Tb L3-edge XANES spectra of ZnO:Tb1 sample and some reference compounds.

recorded XANES spectra for Tb L3-edge were modeled by the sum of two Lorentzian functions [peak A: 7518.6 eV for Tb³⁺ (4f⁸) and peak B: 7531.9 eV for Tb⁴⁺ (4f⁷)] and one arctangent function representing the step-like edge of continuum excitations, see Fig. 5.14. For simplicity, the peak related to the ligand hole state (small hump close to 7510 eV) was omitted because of its unresolved intensity. The curve fittings were performed in the energy range from 7481 to 7554 eV using ATHENA software.

The spectrum at 300 K is characteristic for the Tb³⁺ (4f⁸) valence, contributing to the main peak A. There is a small drop of the intensity of peak A barely perceptible, which is a fingerprint of Tb³⁺, and at the same time, peak B increases slightly. The peak B is a manifestation of Tb⁴⁺ states, namely, of the configuration 4f⁷. The observed behavior thus suggests 3+/4+ mixed valence state in our samples without any tendency as the dopant content is increased.

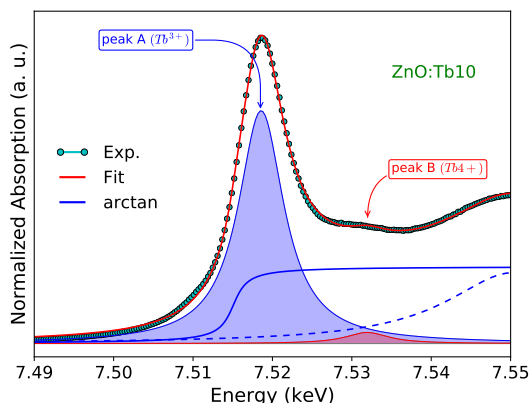


Fig. 5.14 The fit of the Tb L3-edge XANES spectrum of the ZnO:Tb10 sample. For the fit, one arctangent function and two Lorentzian functions (A and B) were used.

References

1. NH Al-Hardan, Azman Jalar, MA Abdul Hamid, Lim Kar Keng, Roslinda Shamsudin, and Burhanuddin Yeop Majlis. The room-temperature sensing performance of ZnO nanorods for 2-methoxyethanol solvent. *Sensor Actuat B Chem*, 203:223–228, 2014.
2. S Hüfner and GK Wertheim. X-ray photoelectron band structure of some transition-metal compounds. *Phys. Rev. B*, 8(10):4857, 1973.
3. Zhigang Yin, Nuofu Chen, Fei Yang, Shulin Song, Chunlin Chai, Jun Zhong, Haijie Qian, and Kurash Ibrahim. Structural, magnetic properties and photoemission study of Ni-doped ZnO. *Solid State Commun.*, 135(7):430–433, 2005.
4. Hao Wang, Y Chen, HB Wang, C Zhang, FJ Yang, JX Duan, CP Yang, YM Xu, MJ Zhou, and Q Li. High resolution transmission electron microscopy and Raman scattering studies of room temperature ferromagnetic Ni-doped ZnO nanocrystals. *Appl. Phys. Lett.*, 90(5):052505, 2007.
5. NS McIntyre and MG Cook. X-ray photoelectron studies on some oxides and hydroxides of cobalt, nickel, and copper. *Anal. Chem.*, 47(13):2208–2213, 1975.
6. CD Wanger, WM Riggs, LE Davis, JF Moulder, and GE Muilenberg. Handbook of X-ray photoelectron spectroscopy. *Perkin-Elmer Corporation, Physical Electronics Division Press, Eden Prairie*, pages 38–81, 1979.
7. JF Moulder, WF Stickle, PE Sobol, and KD Bomben. *Handbook of X-ray photoelectron spectroscopy, Physical Electronics Division, Perkin-Elmer Corporation*. PerkinElmer Corporation, Eden Prairie, 1992.
8. Hongjing Wu, Liuding Wang, Yiming Wang, Shaoli Guo, and Zhongyuan Shen. Enhanced microwave performance of highly ordered mesoporous carbon coated by Ni₂O₃ nanoparticles. *J. Alloys Compd.*, 525:82–86, 2012.
9. SA Chambers, S Thevuthasan, RFC Farrow, RF Marks, JU Thiele, L Folks, MG Samant, AJ Kellock, N Ruzycski, DL Ederer, et al. Epitaxial growth and properties of ferromagnetic Co-doped TiO₂ anatase. *Appl. Phys. Lett.*, 79(21):3467–3469, 2001.
10. TJ Chuang, CR Brundle, and DW Rice. Interpretation of the x-ray photoemission spectra of cobalt oxides and cobalt oxide surfaces. *Surf. Sci.*, 59(2):413–429, 1976.
11. Sasanka Deka and PA Joy. Electronic structure and ferromagnetism of polycrystalline Zn_{1-x}Co_xO (0 ≤ x ≤ 0.15). *Solid State Commun.*, 134(10):665–669, 2005.
12. Petra Lommens, Frank Loncke, Philippe F Smet, Freddy Callens, Dirk Poelman, Henk Vrielinck, and Zeger Hens. Dopant incorporation in colloidal quantum dots: a case study on Co²⁺ doped ZnO. *Chem. Mater.*, 19(23):5576–5583, 2007.
13. Sha Wang, Ping Li, Hui Liu, Jibiao Li, and Yu Wei. The structure and optical properties of ZnO nanocrystals dependence on Co-doping levels. *J. Alloys Compd.*, 505(1):362–366, 2010.
14. NL Tarwal, KV Gurav, T Prem Kumar, YK Jeong, HS Shim, IY Kim, JH Kim, JH Jang, and PS Patil. Structure, X-ray photoelectron spectroscopy and photoluminescence investigations of the spray deposited cobalt doped ZnO thin films. *J. Anal. Appl. Pyrolysis*, 106:26–32, 2014.
15. Weichang Hao, Jianjun Li, Huaizhe Xu, Jiaou Wang, and Tianmin Wang. Evidence of surface-preferential Co distribution in ZnO nanocrystal and its effects on the ferromagnetic property. *ACS Appl. Mater. Interfaces*, 2(7):2053–2059, 2010.
16. Masaoki Oku and Kichinosuke Hirokawa. X-ray photoelectron spectroscopy of Co₃O₄, Fe₃O₄, Mn₃O₄, and related compounds. *J. Electron Spectrosc. Relat. Phenom.*, 8(5):475–481, 1976.
17. M Hassel and H-J Freund. NO on CoO (111) Co (0001): hydroxyl assisted adsorption. *Surf. Sci.*, 325(1-2):163–168, 1995.
18. CV Schenck, JG Dillard, and JW Murray. Surface analysis and the adsorption of Co(II) on goethite. *J. Colloid Interface Sci.*, 95(2):398–409, 1983.
19. PMA Sherwood, D Briggs, and MP Seah. Practical surface analysis. *Auger and X-ray Photoelectron Spectroscopy*, 1:555, 1990.
20. WT Geng and Kwang S Kim. Structural, electronic, and magnetic properties of a ferromagnetic semiconductor: Co-doped TiO₂ rutile. *Phys. Rev. B*, 68(12):125203, 2003.

21. JW Quilty, A Shibata, J-Y Son, K Takubo, T Mizokawa, H Toyosaki, T Fukumura, and M Kawasaki. Signature of carrier-induced ferromagnetism in $Ti_{1-x}Co_xO_2 - \delta$: exchange interaction between high-spin Co^{2+} and the $Ti3d$ conduction band. *Phys. Rev. Lett.*, 96(2):027202, 2006.
22. KS Kim, WE Baitinger, JW Amy, and N Winograd. ESCA studies of metal-oxygen surfaces using argon and oxygen ion-bombardment. *J. Electron Spectrosc. Relat. Phenom.*, 5(1):351–367, 1974.
23. Kung T Ng and David M Hercules. Studies of nickel-tungsten-alumina catalysts by X-ray photoelectron spectroscopy. *J. Phys. Chem.*, 80(19):2094–2102, 1976.
24. KS Kim and RE Davis. Electron spectroscopy of the nickel-oxygen system. *J. Electron Spectrosc. Relat. Phenom.*, 1(3):251–258, 1972.
25. J Matienzo, Lo I Yin, Samue O Grim, and William E Swartz Jr. X-ray photoelectron spectroscopy of nickel compounds. *Inorg. Chem.*, 12(12):2762–2769, 1973.
26. A Davidson, JF Tempere, M Che, H Roulet, and G Dufour. Spectroscopic studies of nickel (II) and nickel (III) species generated upon thermal treatments of nickel/ceria-supported materials. *J. Phys. Chem.*, 100(12):4919–4929, 1996.
27. NS McIntyre, TE Rummery, MG Cook, and D Owen. X-ray photoelectron spectroscopic study of the aqueous oxidation of Monel-400. *J. Electrochem. Soc.*, 123(8):1164–1170, 1976.
28. Cedric J Powell. Recommended auger parameters for 42 elemental solids. *Journal of Electron Spectroscopy and Related Phenomena*, 185(1-2):1–3, 2012.
29. VM Jimenez, A Fernandez, JP Espinos, and AR González-Elipse. The state of the oxygen at the surface of polycrystalline cobalt oxide. *J. Electron Spectrosc. Relat. Phenom.*, 71(1):61–71, 1995.
30. Mitsunobu Sato, Hiroki Hara, Hiroyuki Kuritani, and Toshikazu Nishide. Novel route to Co_3O_4 thin films on glass substrates via N-alkyl substituted amine salt of Co (III)-EDTA complex. *Solar energy materials and solar cells*, 45(1):43–49, 1997.
31. S Lars T Andersson and Russell F Howe. An x-ray photoelectron study of metal clusters in zeolites. *The Journal of Physical Chemistry*, 93(12):4913–4920, 1989.
32. NS McIntyre, DD Johnston, LL Coatsworth, RD Davidson, and JR Brown. X-ray photoelectron spectroscopic studies of thin film oxides of cobalt and molybdenum. *Surf. Interface Anal.*, 15(4):265–272, 1990.
33. CA Strydom and HJ Strydom. X-ray photoelectron spectroscopy studies of some cobalt (II) nitrate complexes. *Inorg. Chim. Acta*, 159(2):191–195, 1989.
34. BD Padalia, William C Lang, PR Norris, LM Watson, and DJ Fabian. X-ray photoelectron core-level studies of the heavy rare-earth metals and their oxides. *Proc. R. Soc. Lond. A*, 354(1678):269–290, 1977.
35. GLP Berning and HC Swart. A study of the oxide grown on Tb and terbium silicide by XPS, AES and XRD. *Appl. Surf. Sci.*, 78(4):339–343, 1994.
36. María Balaguer, Chung-Yul Yoo, Henny JM Bouwmeester, and Jose M Serra. Bulk transport and oxygen surface exchange of the mixed ionic–electronic conductor $Ce_{1-x}Tb_xO_{2-\delta}$ ($x = 0.1, 0.2, 0.5$). *J. Mater. Chem. A.*, 1(35):10234–10242, 2013.
37. Shreyas S Pitale, Vinay Kumar, IM Nagpure, OM Ntwaeaborwa, E Coetsee, and HC Swart. Cathodoluminescent properties and surface characterization of bluish-white $LiAl_5O_8$: Tb phosphor. *J. Appl. Phys.*, 109(1):013105, 2011.
38. G Blanco, JM Pintado, S Bernal, MA Cauqui, MP Corchado, A Galtayries, J Ghijssen, R Sporcken, T Eickhoff, and W Drube. Influence of the nature of the noble metal (Rh, Pt) on the low-temperature reducibility of a Ce/Tb mixed oxide with application as TWC component. *Surf. Interface Anal.*, 34(1):120–124, 2002.
39. Yushuang Zhao, Ji-Guang Li, Mengxi Guo, and Xiaojing Yang. Structural and photoluminescent investigation of $LTbH/LEuH$ nanosheets and their color-tunable colloidal hybrids. *J. Mater. Chem. C*, 1(22):3584–3592, 2013.
40. Benjaram M Reddy, Pranjali Saikia, Pankaj Bharali, Yusuke Yamada, Tetsuhiko Kobayashi, Martin Muhler, and Wolfgang Grünert. Structural characterization and catalytic activity of nanosized ceria-terbia solid solutions. *J. Phys. Chem. C*, 112(42):16393–16399, 2008.

41. Yasemin Caglar. Sol-gel derived nanostructure undoped and cobalt doped ZnO: Structural, optical and electrical studies. *J. Alloys Compd.*, 560:181–188, 2013.
42. Ganesh Kumar Mani and John Bosco Balaguru Rayappan. A highly selective and wide range ammonia sensor—Nanostructured ZnO: Co thin film. *Materials Science and Engineering: B*, 191:41–50, 2015.
43. Lee M Moroney, Roger St C Smart, and M Wyn Roberts. Studies of the thermal decomposition of β NiO(OH) and nickel peroxide by X-ray photoelectron spectroscopy. *Journal of the Chemical Society, Faraday Transactions 1: Physical Chemistry in Condensed Phases*, 79(8):1769–1778, 1983.
44. Christoskova St G, M Stoyanova, M Georgieva, and D Mehandjiev. Preparation and characterization of a higher cobalt oxide. *Mater. Chem. Phys.*, 60(1):39–43, 1999.
45. Daniela Bekermann, Alberto Gasparotto, Davide Barreca, Anjana Devi, and Roland A Fischer. p-Co₃O₄/n-ZnO, Obtained by PECVD, Analyzed by X-ray Photoelectron Spectroscopy. *Surface Science Spectra*, 18(1):36–45, 2011.
46. Ping Li, Sha Wang, Jibiao Li, and Yu Wei. Structural and optical properties of Co-doped ZnO nanocrystallites prepared by a one-step solution route. *J. Lumin.*, 132(1):220–225, 2012.
47. G Vijayaprasath, R Murugan, J Shankara Narayanan, V Dharuman, G Ravi, and Y Hayakawa. Glucose sensing behavior of cobalt doped ZnO nanoparticles synthesized by co-precipitation method. *J. Mater. Sci-Mater. El.*, 26(7):4988–4996, 2015.
48. JJ Belrán, CA Barrero, and A Punnoose. Identifying the sources of ferromagnetism in sol-gel synthesized Zn_{1-x}Co_xO ($0 \leq x \leq 0.10$) nanoparticles. *J. Solid State Chem.*, 240:30–42, 2016.
49. Yanmei Liu, Tao Wang, Xia Sun, Qingqing Fang, Qingrong Lv, Xueping Song, and Zaoqi Sun. Structural and photoluminescent properties of Ni-doped ZnO nanorod arrays prepared by hydrothermal method. *Appl. Surf. Sci.*, 257(15):6540–6545, 2011.
50. Aditi S Risbud, Lauren P Snedeker, Margaret M Elcombe, Anthony K Cheetham, and Ram Seshadri. Wurtzite CoO. *Chem. Mater.*, 17(4):834–838, 2005.
51. DC Koningsberger, BL Mojet, GE Van Dorssen, and DE Ramaker. XAFS spectroscopy; fundamental principles and data analysis. *Top. Catal.*, 10(3-4):143–155, 2000.
52. Matthea A Peck and Marjorie A Langell. Metal Structural Environment in Zn_xNi_{1-x}O Macroscale and Nanoscale Solid Solutions. *J. Phys. Chem. C*, 118(22):12050–12060, 2014.
53. Takashi Yamamoto. Assignment of pre-edge peaks in K-edge x-ray absorption spectra of 3d transition metal compounds: electric dipole or quadrupole? *X-Ray Spectrometry: An International Journal*, 37(6):572–584, 2008.
54. H Fujishiro, T Naito, D Takeda, N Yoshida, T Watanabe, K Nitta, J Hejtmánek, K Knížek, and Z Jiráček. Simultaneous valence shift of Pr and Tb ions at the spin-state transition in (Pr_{1-y}Tb_y)_{0.7}Ca_{0.3}CoO₃. *Phys. Rev. B*, 87(15):155153, 2013.

Chapter 6

Point Defects and Emission Properties of Doped ZnO Nanocrystals

Electron paramagnetic resonance (EPR) and photoluminescence (PL) spectroscopies are two of the most powerful tools that can be used to study the point defects of the materials. Correlation of results obtained from these techniques allows yielding a more complete insight into defect structures in ZnO compounds. In this section, we present the experimental results of pure and doped ZnO NCs. We consider the study of mechanisms by which the different EPR oscillations and emission bands occur: a short-wavelength band near the fundamental absorption edge (NBE), a broad long-wavelength band—the maximum of which usually lies in the green spectral range, a red emission and bands related to dopant ions.

6.1 EPR study of the defects-related region

In order to investigate the intrinsic defect centers and the effects of the doping—which will be described in the next chapter, X-band EPR measurements were carried out. Contaminations of the samples from either metal ions, such as Mn^{2+} , Fe^{3+} , or Cr^{3+} which can in principle be easily detected by EPR even at extremely low concentrations, are not observed and can, therefore, be excluded. Fig. 6.1 shows the 100K X-band EPR signal (9.45 GHz) of pure ZnO NCs. As observed, mainly two predominant paramagnetic signals were observed. It is worth mentioning that these signals were also observed for all doped samples. They are spectrally close to each other and correspond to a strong broad resonance with $g = 2.005$ and one weaker and narrower line with $g = 1.961$. The predominant paramagnetic band with a g -factor close to the free-electron value ($g \sim 2.0023$) is commonly observed in bulk ZnO and it is controversially discussed in the literature. It could be assigned to a singly ionized Zn vacancy [1, 2], or to an unpaired electron trapped on an oxygen vacancy site ($g = 1.9965$, 1.9948 [3], 2.0190 [4], 2.0106) [5] (i.e., an F+ center) [3]. The former assignment was only observed when ZnO was irradiated with UV light [6] and the authors related to the resolved hyperfine interaction with the four neighboring Zn nuclei. This finding is also consistent with results obtained from density functional theory calculations [7],

which indicate that a certain excitation is required to generate the paramagnetic +1 state Zn vacancy. On the other hand, the oxygen vacancies generated in the surface region of ZnO nanostructures [8] are stable and could trap electrons to form paramagnetic centers (F+ centers). This could also account for the stable EPR signal at $g \sim 2.005$ detected in our samples. The spectrum of pure ZnO sample shows also an additional EPR line at $g = 1.961$ that has already been reported in the literature [9–11]. However, the origin of this signal is controversial in the literature. Assignments to shallow donors, singly ionized oxygen vacancies, Zn vacancies, or oxygen and zinc interstitials are found in the literature [12, 13].

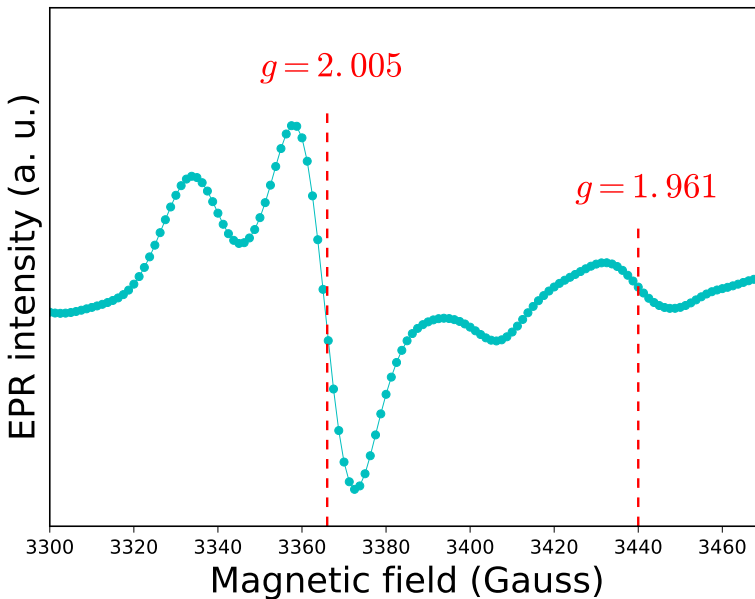


Fig. 6.1 100 K EPR spectrum of pure ZnO NCs.

For the doped ZnO NCs, the region of nickel-related defects could not be well analyzed because of the overlapping with the mean signal of Ni oscillation, so the analysis will be focused on the region of Co- and Tb-related defects. In Fig. 6.2(a) is shown for comparison the X-band EPR signal of pure ZnO and; Co and Tb-doped ZnO NCs with 1 and 10 mol% of concentration. As can be observed, the $g = 2.005$ signal is the predominant one in all samples. This signal was assigned to the superficial defects as proposed by Kaftelen et. al., [14] in the framework of the core-shell model where the core-defects are related with the $g = 1.961$ signal and the shell with the $g = 2.005$ signal which contain high concentration of defect complexes, in particular positively charged oxygen vacancies. It reveals that the superficial defects are present in all samples, as expected due to the NCs size. However, the $g = 1.961$ signal is presented in the pure ZnO and Tb-doped ZnO and it does not appear (or is unresolved) in the Co-doped ZnO samples. To get a better understanding of this signal, in Fig. 6.2(b) are shown the

EPR spectra of 10 mol% Co and Tb-doped ZnO. The $g = 2.005$ decrease slightly in the Tb-doped ZnO and decrease very much, almost to disappear in the Co-doped samples. This g -factor is usually associated with oxygen vacancies located at the surface of the ZnO NCs which could trap electrons to form F⁺ centers. In addition, the $g = 1.961$ signal becomes significantly stronger with the increase of Tb content, meanwhile, it remains unresolved for the samples with 10 mol% Co. The $g = 1.961$ signal has been attributed to core-related defects. Due to the differences between the oxidation states and ionic sizes of Tb³⁺ and Zn²⁺ ions, the insertion of Tb in the ZnO matrix gives rise to problems related to the miscibility of Tb in the oxide matrix, lattice distortion, and disorder. Those contributions as expected to have major effects on the EPR signal and optical emission of Tb as quoted in the literature [15].

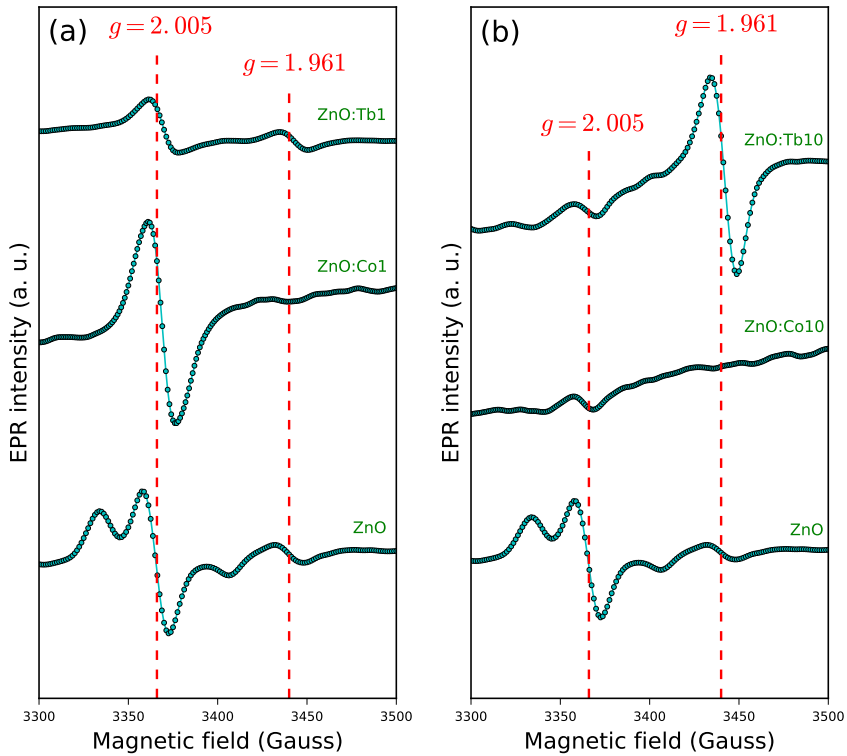


Fig. 6.2 100 K EPR spectra of the defects-related region of ZnO NCs: (a) Pure and 1 mol% Co and Tb-doped samples and, (b) pure and 10 mol% Co and Tb-doped samples.

This finding is in accordance with the proposed model to explain the decrease of lattice constant “c” value with dopant increase (see Chap. 4). The incorporation of Tb ions in the ZnO matrix results in the formation of oxygen vacancies, which are responsible for the decreasing trend of the c-lattice parameter. It must be pointed out

Table 6.1 List of g -factors determined from the EPR spectra in the defects-related region for pure and doped ZnO NCs.

Sample	ν (MHz)	B (Gauss)	g
ZnO	9441.767	3370	2.0046
		3440	1.9612
ZnO:Co1	9448.475	3370	2.0030
ZnO:Co3	9442.356	3370	2.0039
ZnO:Co5	9440.516	3370	2.0036
ZnO:Co10	9437.226	3360	2.0051
ZnO:Tb1	9450.175	3370	2.0039
		3440	1.9613
ZnO:Tb3	9451.665	3370	2.0037
		3440	1.9607
ZnO:Tb5	9446.496	3370	2.0036
		3450	1.9588
ZnO:Tb10	9444.744	3360	2.0059
		3440	1.9607

that single oxygen vacancies are not EPR active, because they need to have trapped electrons to be detected.

6.2 Photoluminescence Results

The photoluminescence (PL) measurements were carried out for pure and doped-ZnO NCs covering the wavelength range from 330 nm to 900 nm. In Fig. 6.3(a) is presented the PL spectrum of pure ZnO NCs at room temperature. The different peaks that appeared in the PL spectrum were well-fitted with Gaussian functions. We identify four PL emission bands which are centered at 353.9 nm (3.50 eV), 373.0 nm (3.33 eV), 525.3 nm (2.36 eV) and 730.3 nm (1.70 eV). The UV emission bands observed at 353.9 nm and 373.0 nm were assigned to the near-band emissions (NBE's), attributed to the photo-stimulated creation of excitons having energies just below the ZnO band-edge and their subsequent recombination [16]. Generally, the NBE in ZnO is observed in the range of 360 to 420 nm at room temperature [17]. However, the appearance of the NBE at 353.9 nm is due to the fact that the optical band gap in the present samples is found to be 3.50 eV (calculated using the $E = h\nu$ relation), as compared to the bulk value of around 3.37 eV [18]. The higher band gap value of our samples could be related to the NCs size which leads to the appearance of quantum confinement effects. Native defects have been suggested as potential sources of broadband emissions in the visible region, which extends over the range of 420–680 nm. Those emissions are related to Zn vacancies (V_O), interstitial Zn (Zn_i), interstitial O (O_i), and substitution of O at a Zn position (O_{Zn}) (see Chap. 2 for more details). We analyze the broad green band emission further in this section. The origin of the well-defined red emission band cen-

tered at 730.3 nm is more controversial. Some authors have attributed it to interstitial Zn in the ZnO structure; meanwhile, some other authors have suggested that emission as a second-order feature of the UV emission [19, 20]. Based on size considerations, it is therefore expected that the Zn interstitial will be more stable at the octahedral site where the geometrical constraints are less severe. Indeed, it has been found that the octahedral site is the stable site for Zn_i , whereas the Zn_i at the tetrahedral site is 0.9 eV higher in energy and unstable as it spontaneously relaxes to the octahedral site [12, 13]. In Fig. 6.3(b) are shown the temperature-dependent PL spectra of pure ZnO NCs in the range of 140–300K. As observed, the 525.3 and 730.3 nm peaks become more intense with the temperature decrease. This tendency is assigned to the freeze-out of phonons and quenching of non-radiative recombination processes. A blue shift of the band-edge emission over this temperature range is caused by the thermal contraction of the lattice and the changing strength of the electron-phonon interactions [21].

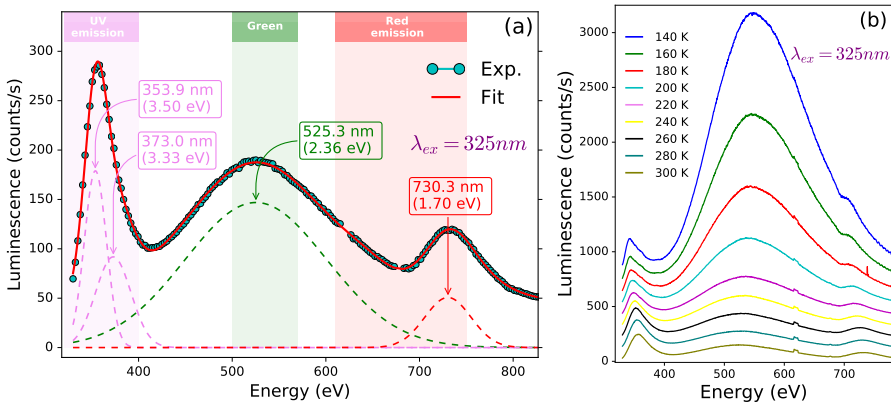


Fig. 6.3 (a) Room temperature PL spectra of pure ZnO NCs and, (b) PL spectra of pure ZnO NCs obtained at different temperatures. The curves have been displaced on the y-axis for better visualization.

In Fig. 6.4 is shown the PL spectra of 1 and 10 mol% Ni-doped ZnO NCs. As observed, the spectra basically exhibit similar emission features when compared to the pure ZnO NCs. The deconvolution of the room temperature emission spectra is well resolved by four peaks centered at 349.1 (349.0) nm, 365.1 (—) nm, 534.9 (543.0) nm and 728.2 (722.4) nm for the 1 mol% (10 mol%) Ni-doped sample. The green emission stays as the predominant contribution and; the NBE and red emission show notoriously diminished intensity as the dopant concentration increases. The nickel cations can provide competitive pathways for recombination, which results in quenching of the broad green emission. A similar fluorescent quenching behavior has also been previously reported in ZnO NCs and it is commonly attributed to the non-radiative process or charge transfer process [22, 23]. A well-defined red emission band centered at 728.2 nm in sample ZnO:Ni1 corresponds to the 730.3 nm emission band of pure ZnO NCs and, it seems to involve interstitial Zn [12, 13].

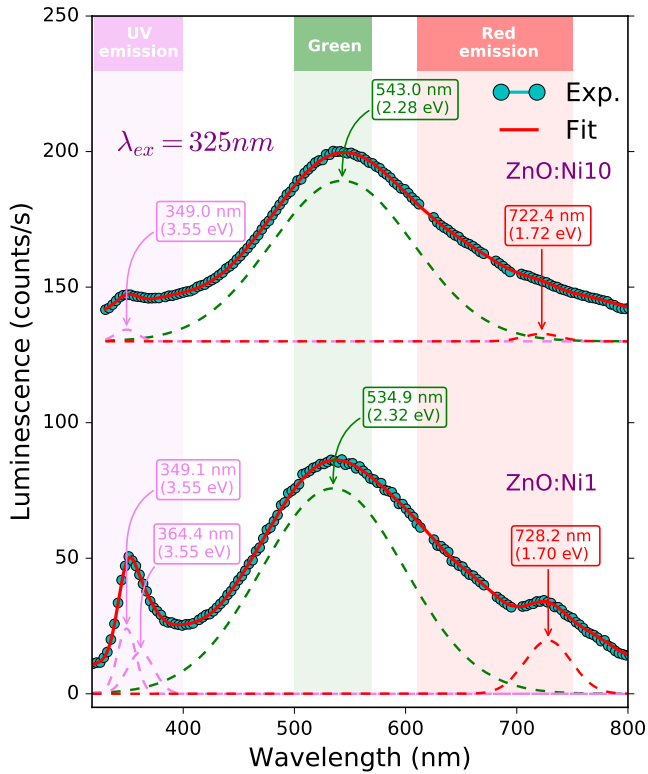


Fig. 6.4 Room temperature PL spectra of 1 and 10 mol% Ni-doped ZnO NCs.

In Fig. 6.5 is shown the room temperature photoluminescence spectra of Co-doped ZnO NCs. The spectra show deconvoluted peaks which correspond to the NBE UV emission band at 344.2 (346.6) nm and visible emission bands centered at 522.5 (533.6) nm, 661.9 (661.4) nm and 718.5 (720.9) nm for the 1 mol% (10 mol%) Co-doped sample. The UV emission corresponds to the excitonic emission, that is to the recombination of an electron in the conduction band and a hole in the valence band across the gap of the sample [24]. While increasing the doping concentration, the UV near band emission is blue-shifted—which was assigned to the quantum confinement effects, and the visible emission peaks reduce considerably after the doping in comparison to the pure ZnO NCs (see Fig. 6.5(b)).

Recently, T. J. Penfold et. al., [25] attempted to fit time-resolved EXAFS spectrum using the 2% V_O^\bullet and 23% $V_O^{\bullet\bullet}$ bond length elongations and the Zn vacancy (V_{Zn}) reported by Janotti and de Walle [7, 12, 13] and they obtained unsatisfactory agreement with the experimental data. The simulated EXAFS spectra considering the different defects' structure showed that the best results are achieved for the $V_O^{\bullet\bullet}$ defect with a 15% outward distortion. Thus, they conclude that the long-lived trapped state and the source of the green luminescence is the $V_O^{\bullet\bullet}$ defect in agreement with Ref. [22, 26]

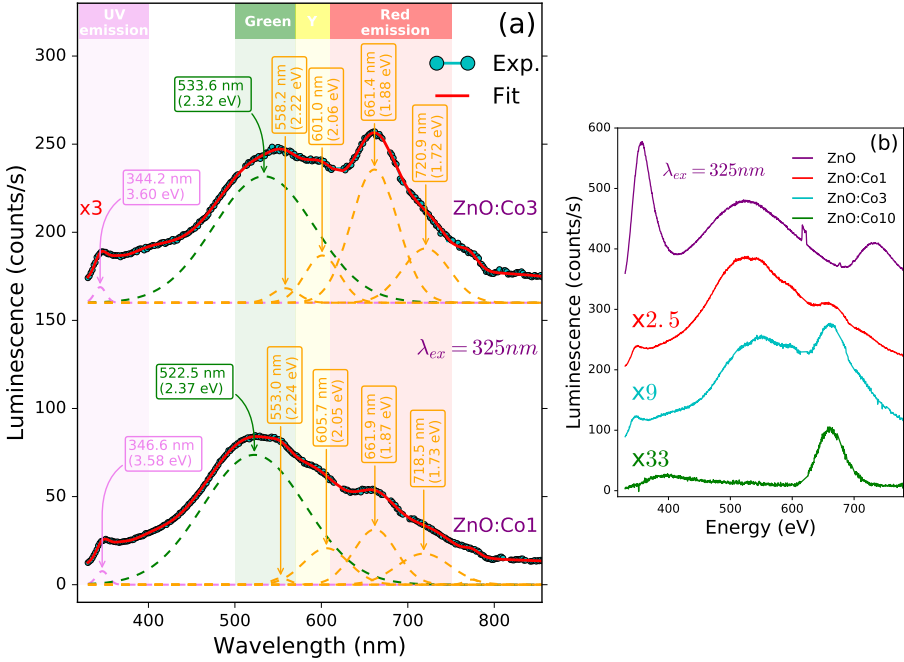


Fig. 6.5 (a) Room temperature PL spectra of Co-doped ZnO NCs (1 and 10 mol%) and, (b) PL spectra of the pure and Co-doped ZnO NCs—for comparison.

where the formation of $V_O^{\bullet\bullet}$ was hypothesized as a result of the trapping of a photogenerated hole at a pre-existing V_O^\bullet defect. According to our previous analysis, the EPR spectra of Co-doped ZnO samples show a decreasing trend in the intensity of the band corresponding to $g = 2.005$ as the Co content increase. We associated this g -factor to oxygen vacancies located at the surface of the ZnO NCs which could trap electrons to form F^+ centers. If the green emission depends on the pre-existing V_O^\bullet sites; then, the absence or presence of this sites may result in the absence or presence of green luminescence. When Co content reaches 10 mol% the green emission is suppressed, as can be inferred from Fig. 6.5, in agreement with the absence of the EPR oscillation at $g = 2.005$. We must remember that the $V_O^{\bullet\bullet}$ sites cannot be detected directly by EPR measurements (as indicated in Chap. 2), but the initial V_O^\bullet site does. Then, we believe that through a photogenerated process a surface-trapped hole could recombine with an electron trapped in an oxygen vacancy (V_O^\bullet) resulting in the creation of a $V_O^{\bullet\bullet}$ center, the recombination centers for green emission of ZnO as proposed by the Ref. [22, 25, 26]. In addition, the dopant cations can provide competitive pathways for recombination, which results in quenching of the broad green emission. A similar fluorescent quenching behavior has also been previously observed in doped ZnO NCs. That quenching is also observed in Ni-doped samples as previously discussed, and it is commonly attributed to the non-radiative process or charge transfer process [27]. Otherwise, the dopant ions can decrease the concentration of surface defects in ZnO NCs, driving to

the visible emissions become weak [24, 27]. It is worth to mention that in the EPR analysis it was observed the decreasing of the $g = 2.005$ signal when increasing the Co content. It suggests that the density of surface defects is reduced after doping, which is in agreement with the PL results.

Some authors have reported UV-Vis absorption band edges at 565, 610, and 653 nm, which mainly arises from the spin-orbit splitting of the ${}^4T_1(P)$ state and to a minor extent from the mixing of this ${}^4T_1(P)$ state with nearby spin forbidden doublet states (${}^2E(G)$, ${}^2T_1(G)$, ${}^2A_1(G)$ and ${}^2T_2(G)$), which correspond to the $d-d$ transition of high-spin state Co^{2+} ($3d^7$) in the tetrahedral sites of ZnO [28–32]. We believe that the three additional absorption peaks, in comparison with pure ZnO, located at approximately 553.0 (558.2) nm, 605.7 (601.0) nm and 661.9 (661.4) nm for the 1 mol% (10 mol%) Co-doped ZnO sample, are related to those reported UV-Vis transitions. However, the emission band at around 661 nm has been identified in PL measurements and assigned to the characteristic ${}^4T_1(P) \rightarrow {}^4A_2(F)$ $d-d^*$ internal transition between localized Co^{2+} ions in a tetrahedral crystal field [32–34]. Generally, the red emission (661 nm) for the Co-doped ZnO NCs is considered as a further support that Co^{2+} ions are substituting the tetrahedrally coordinated Zn^{2+} ions in the ZnO matrix [25, 35–37]. Therefore, the red emission could involve Co-related impurities and intrinsic defect levels inside the bandgap. Co centers can bind to electrons as an isoelectronic trap and then trap holes in the valence band via the long-range Coulomb attractive potential. It causes Co-doped ZnO NCs to have donor-type ionization states slightly below the conduction band. When Co-doped ZnO NCs is excited by UV light, photogenerated electrons and holes transfer non-radiatively into the manifold of the ligand field levels of Co centers, producing efficient Co-related emissions. For excitation energies below the bandgap, trapped electrons are transferred non-radiatively to extended defect states, resulting in a red emission [28, 30, 38]. Finally, the red emission band centered at 718.5 nm and 720.9 for ZnO:Co1 and ZnO:Co10 samples, respectively—only resolved through peak deconvolution—has been attributed to the same emission process of the 730.3 nm band of pure ZnO NCs which is also resolved in Ni-doped samples. This band was associated with Zn interstitial [18].

The PL emission spectra of Tb-doped ZnO NCs are shown in Fig. 6.6. The Tb^{3+} ions have an important effect on the UV emission of ZnO NCs when compared with the cobalt and nickel doping. The spectrum obtained for sample ZnO:Tb1 (ZnO:Tb3) show a high UV emission at 350.3 (350.6) nm related to excitonic recombination, an emission at 364.0 (364.4) nm (blue), a broad deep-level-emission at 527.0 (535.3) nm (green) and 727.5 (733.9) nm (red). The green emission was attributed to the formation of $\text{V}_\text{O}^{\bullet\bullet}$ as a result of the trapping of a photogenerated hole at a pre-existing $\text{V}_\text{O}^\bullet$ site, similar to that discussed for the Co-doped ZnO samples. Well-defined peaks are observed for all Tb-doped samples. The carrier relaxation from the excited states of the ZnO hosts to the dopant, resulting in the characteristic emission peaks of Tb^{3+} ions. A major narrow band green emission at 516.1 (516.1) nm and minor emissions at 460.8 (461.0), 556.1 (556.6) and (592.1) 591.9 nm are determined for sample ZnO:Tb1 (ZnO:Tb3); and attributed to the Tb intraionic transitions ${}^5D_4 \rightarrow {}^7F_5$, ${}^5D_4 \rightarrow {}^7F_6$, ${}^5D_4 \rightarrow {}^7F_4$, ${}^5D_4 \rightarrow {}^7F_3$ of Tb^{3+} ions, respectively [39].

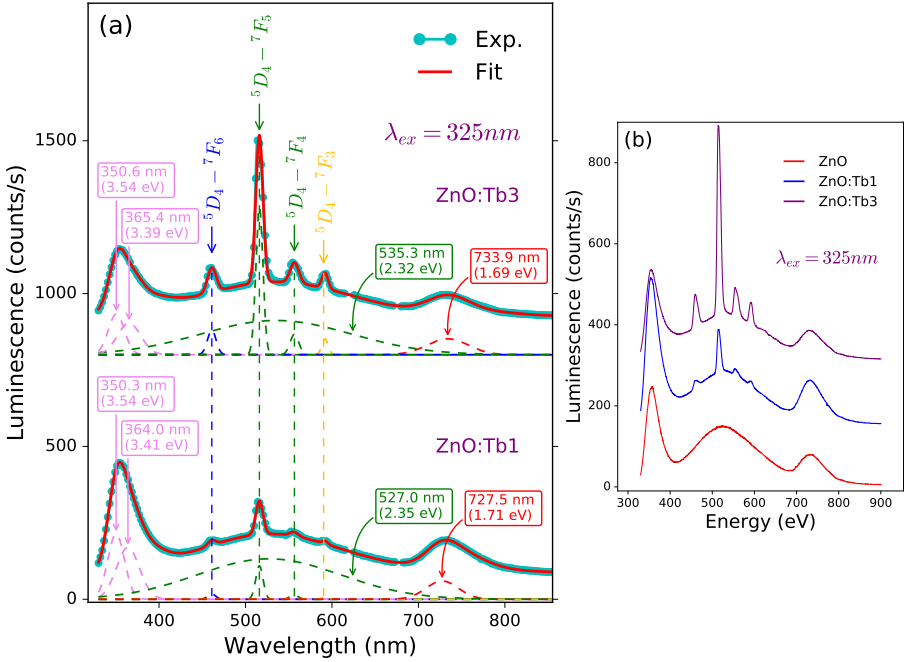


Fig. 6.6 (a) Room temperature PL spectra of Tb-doped ZnO NCs (1 and 10 mol%) and, (b) PL spectra of the pure and Co-doped ZnO NCs—for comparison.

Table 6.2 List of photoluminescence emissions determined from the deconvolution of PL spectra of pure and doped ZnO NCs.

Sample	NBE (nm)	Blue emission (nm)	Green emission (nm)	Yellow-orange emission (nm)	Red emission (nm)
ZnO	353.9/373.0	—	525.3	—	730.3
ZnO:Ni1	349.1/364.4	—	534.9	—	728.2
ZnO:Ni10	349.0	—	543.0	—	722.4
ZnO:Co1	346.6	—	522.5/553.0	605.7	661.9/718.5
ZnO:Co3	344.2	—	533.6/558.2	601.0	661.4/720.9
ZnO:Co10	—/392.2	—	—	—	662.6/—
ZnO:Tb1	350.3/364.0/382.9	460.8	516.1/556.1/527.0	592.1	—/727.5
ZnO:Tb10	350.6/365.4/388.9	461.0	516.1/535.3/556.6	591.9	—/733.9

References

1. D Galland and A Herve. ESR spectra of the zinc vacancy in ZnO. *Phys. Lett. A*, 33(1):1–2, 1970.
2. AL Taylor, G Filipovich, and GK Lindeberg. Electron paramagnetic resonance associated with Zn vacancies in neutron-irradiated ZnO. *Solid State Communications*, 8(17):1359–1361, 1970.
3. NG Kakazey, TV Sreckovic, and MM Ristic. Electronic paramagnetic resonance investigation of the evolution of defects in zinc oxide during tribophysical activation. *J. Mater. Sci.*, 32(17):4619–4622, 1997.
4. Baolong Yu, Congshan Zhu, Fuxi Gan, and Yabin Huang. Electron spin resonance properties of ZnO microcrystallites. *Mater. Lett.*, 33(5-6):247–250, 1998.
5. Vladislav Ischenko, Sebastian Polarz, Dirk Grote, Victorina Stavarache, Karin Fink, and Matthias Driess. Zinc oxide nanoparticles with defects. *Adv. Funct. Mater.*, 15(12):1945–1954, 2005.
6. A Pöpl and G Völkel. ESR and Photo-ESR Investigations of Zinc Vacancies and Interstitial Oxygen Ions in Undoped ZnO Ceramics. *physica status solidi (a)*, 125(2):571–581, 1991.
7. Anderson Janotti and Chris G Van de Walle. Oxygen vacancies in ZnO. *Appl. Phys. Lett.*, 87(12):122102, 2005.
8. M Kakazey, M Vlasova, M Dominguez-Patino, G Dominguez-Patiño, T Srećković, and Natalija Nikolić. Electron paramagnetic resonance in the research of defect formation and thermal processes during grinding of ZnO powders. *Science of Sintering*, 36(2):65–72, 2004.
9. KM Sancier. Temperature dependence of the electron spin resonance spectra of zinc oxide powder. *J. Phys. Chem.*, 76(18):2527–2529, 1972.
10. SM Evans, NC Giles, LE Halliburton, and LA Kappers. Further characterization of oxygen vacancies and zinc vacancies in electron-irradiated ZnO. *J. Appl. Phys.*, 103(4):043710, 2008.
11. Yi Hu and Hung-Jiun Chen. Preparation and characterization of nanocrystalline ZnO particles from a hydrothermal process. *J. Nanopart. Res.*, 10(3):401–407, 2008.
12. Anderson Janotti and Chris G Van de Walle. Native point defects in ZnO. *Phys. Rev. B*, 76(16):165202, 2007.
13. Anderson Janotti and Chris G Van de Walle. Fundamentals of zinc oxide as a semiconductor. *Reports on progress in physics*, 72(12):126501, 2009.
14. Hülya Kaftelen, Kasim Ocakoglu, Ralf Thomann, Suyan Tu, Stefan Weber, and Emre Erdem. EPR and photoluminescence spectroscopy studies on the defect structure of ZnO nanocrystals. *Phys. Rev. B*, 86(1):014113, 2012.
15. Rafael Pérez-Casero, Araceli Gutiérrez-Llorente, Olivier Pons-Y-Moll, Wilfrid Seiler, Reine Marie Defourneau, Daniel Defourneau, Eric Millon, Jacques Perriere, Philippe Goldner, and Bruno Viana. Er-doped ZnO thin films grown by pulsed-laser deposition. *J. Appl. Phys.*, 97(5):054905, 2005.
16. EJ Guidelli, O Baffa, and DR Clarke. Enhanced UV emission from silver/ZnO and gold/ZnO core-shell nanoparticles: photoluminescence, radioluminescence, and optically stimulated luminescence. *Scientific reports*, 5:14004, 2015.
17. Zhe Chuan Feng. *Handbook of zinc oxide and related materials: volume two, devices and nano-engineering*, volume 2. CRC press, 2012.
18. Hadis Morkoç and Ümit Özgür. *Zinc oxide: fundamentals, materials and device technology*. John Wiley & Sons, 2008.
19. RBM Cross, MM De Souza, and EM Sankara Narayanan. A low temperature combination method for the production of ZnO nanowires. *Nanotechnology*, 16(10):2188, 2005.
20. T Mahalingam, Kyung Moon Lee, Kyung Ho Park, Soonil Lee, Yeonghwan Ahn, Ji-Yong Park, and Ken Ha Koh. Low temperature wet chemical synthesis of good optical quality vertically aligned crystalline ZnO nanorods. *Nanotechnology*, 18(3):035606, 2007.
21. Lori E Greene, Matt Law, Joshua Goldberger, Franklin Kim, Justin C Johnson, Yanfeng Zhang, Richard J Saykally, and Peidong Yang. Low-temperature wafer-scale production of ZnO nanowire arrays. *Angew. Chem.*, 115(26):3139–3142, 2003.
22. A Van Dijken, EA Meulenkaamp, D Vanmaekelbergh, and A Meijerink. Identification of the transition responsible for the visible emission in ZnO using quantum size effects. *J. Lumin.*, 90(3-4):123–128, 2000.

23. D Scott Bohle and Carla J Spina. Controlled Co (II) doping of zinc oxide nanocrystals. *J. Phys. Chem. C*, 114(42):18139–18145, 2010.
24. Shaobo Shi, Yu Yang, Jianping Xu, Lan Li, Xiaosong Zhang, Guo-Hua Hu, and Zhi-Min Dang. Structural, optical and magnetic properties of Co-doped ZnO nanorods prepared by hydrothermal method. *J. Alloys Compd.*, 576:59–65, 2013.
25. Thomas J Penfold, Jakub Szlachetko, Fabio G Santomauro, Alexander Britz, Wojciech Gawelda, Gilles Doumy, Anne Marie March, Stephen H Southworth, Jochen Rittmann, Rafael Abela, et al. Revealing hole trapping in zinc oxide nanoparticles by time-resolved X-ray spectroscopy. *Nature communications*, 9(1):478, 2018.
26. Addy van Dijken, Eric A Meulenkamp, Daniel Vanmaekelbergh, and Andries Meijerink. Identification of the transition responsible for the visible emission in ZnO using quantum size effects. *J. Lumin.*, 90:123–128, 2000.
27. Bharati Panigrahy, M Aslam, and D Bahadur. Aqueous synthesis of Mn-and Co-doped ZnO nanorods. *J. Phys. Chem. C*, 114(27):11758–11763, 2010.
28. Kevin R Kittilstved, William K Liu, and Daniel R Gamelin. Electronic structure origins of polarity-dependent high-TC ferromagnetism in oxide-diluted magnetic semiconductors. *Nature materials*, 5(4):291, 2006.
29. Sha Wang, Ping Li, Hui Liu, Jibiao Li, and Yu Wei. The structure and optical properties of ZnO nanocrystals dependence on Co-doping levels. *J. Alloys Compd.*, 505(1):362–366, 2010.
30. Jianping Xu, Shaobo Shi, Lan Li, Xiaosong Zhang, Youwei Wang, Qingliang Shi, Shubin Li, and Hao Wang. Luminescence properties of cobalt-doped ZnO films prepared by sol-gel method. *Journal of electronic materials*, 42(12):3438–3444, 2013.
31. R Baghdad, N Lemée, G Lamura, A Zeinert, N Hadj-Zoubir, M Bousmaha, MA Bezzerrouk, H Bouyanfif, B Allouche, and K Zellama. Structural and magnetic properties of Co-doped ZnO thin films grown by ultrasonic spray pyrolysis method. *Superlattices and Microstructures*, 104:553–569, 2017.
32. P Koidl. Optical absorption of Co²⁺ in ZnO. *Phys. Rev. B*, 15(5):2493, 1977.
33. Xuefeng Wang, JB Xu, Ning Ke, Jiaguo Yu, Juan Wang, Quan Li, HC Ong, and R Zhang. Imperfect oriented attachment: Direct activation of high-temperature ferromagnetism in diluted magnetic semiconductor nanocrystals. *Appl. Phys. Lett.*, 88(22):223108, 2006.
34. Petra Lommens, Frank Loncke, Philippe F Smet, Freddy Callens, Dirk Poelman, Henk Vrielinck, and Zeger Hens. Dopant incorporation in colloidal quantum dots: a case study on Co²⁺ doped ZnO. *Chem. Mater.*, 19(23):5576–5583, 2007.
35. Petra Lommens, Philippe F Smet, Celso de Mello Donega, Andries Meijerink, Luc Piraux, Sebastien Michotte, Stefan Mátéfi-Tempfli, Dirk Poelman, and Zeger Hens. Photoluminescence properties of Co²⁺-doped ZnO nanocrystals. *J. Lumin.*, 118(2):245–250, 2006.
36. Benjamin D Yuhas, David O Zitoun, Peter J Pauzaskie, Rongrui He, and Peidong Yang. Transition-metal doped zinc oxide nanowires. *Angew. Chem. Int. Ed.*, 45(3):420–423, 2006.
37. Xuefeng Wang, Rongkun Zheng, Zongwen Liu, Ho-pui Ho, Jianbin Xu, and Simon P Ringer. Structural, optical and magnetic properties of Co-doped ZnO nanorods with hidden secondary phases. *Nanotechnology*, 19(45):455702, 2008.
38. Trinh Thi Loan, Nguyen Ngoc Long, et al. Photoluminescence properties of Co-doped ZnO nanorods synthesized by hydrothermal method. *Journal of Physics D: Applied Physics*, 42(6):065412, 2009.
39. Vinod Kumar, OM Ntwaeaborwa, T Soga, Viresh Dutta, and HC Swart. Rare earth doped zinc oxide nanophosphor powder: a future material for solid state lighting and solar cells. *ACS Photonics*, 4(11):2613–2637, 2017.

Chapter 7

Magnetic Properties of Doped ZnO Nanocrystals

This section is dedicated to studying the magnetic response of the synthesized nanocrystals. Firstly, EPR measurements of ZnO NCs doped with Co and Ni are presented, and then we show the SQUID-based magnetometry results in order to evidence the magnetic response of all samples.

7.1 Doping effects on EPR response

Fig. 7.1 shows the 100K X-band EPR signal of the Co-doped ZnO samples with different Co concentrations. As observed, a pattern typical of centers with $g_{\perp} > g_{\parallel}$, resulting in the first-derivative spectrum characterized by intense and broad g_{\perp} ($g_x = g_y$) features with mainly positive signal intensity and weak and narrower g_{\parallel} (g_z) features with negative signal intensity. The intense and broad resonance is located at around $g_{\perp} = 4.35$ ($H = 1550G$) and the weaker band at $g_{\parallel} = 2.29$ ($H = 3000G$) (see Table 7.1 for details). A deep analysis of the EPR data relies on the assignment of each resonance to the cobalt local environment. Firstly, the presence of molecular clusters was ruled out. There are few examples in the literature on the use of EPR to fully characterize cobalt based molecular clusters [1–3].

It is well established that the ground state of Co^{2+} at a tetrahedral site in the ZnO host lattice is described by a $S = 3/2$ spin Hamiltonian containing the Zeeman and zero-field splitting terms. As the latter term is stronger than the former (the zero-field splitting constant $D = 2.76 \text{ cm}^{-1}$) [4, 5], there will be a splitting of the ground state on two doublets. In consequence, a low-frequency EPR study ($\nu \sim 9.45 \text{ GHz}$) will only observe transitions in the low lying doublet: $S_z = \pm 1/2$. The extracted values, $g_{\parallel} = 2.29$ and $g_{\perp} = 4.35$, as can be seen in Fig. 7.1 and Table 7.1, are very close to those obtained for single crystals and thin films of ZnO:Co ($g_{\parallel} = 2.24$, $g_{\perp} = 4.55$ [4, 5]). For nanoparticles, the value of g_{\perp} has been found in the range of 4.30 to 4.43 [6].

The presence of other phases such as metallic Co, CoO, or Co_3O_4 , cannot be used to explain this feature. Given the synthesis conditions, the XPS and XANES results (see Chap. 5) the presence of metallic cobalt is very unlikely. Moreover, it should give an

additional contribution to the XPS spectrum with a binding energy ~ 2 eV lower than that of Co^{2+} [6] and additional oscillations in the XAFS spectra (see Chap. 4). The cobalt oxides CoO and Co_3O_4 have markedly different EPR spectra: Co_3O_4 has only a broad signal at $g \sim 2$ [7], while CoO should yield an isotropic EPR signal at $g \sim 4.33$. Therefore, the features of the EPR spectrum of Co-doped ZnO NCs are likely due to the Co^{2+} ions substituting Zn^{2+} ions in the wurtzite structure in consistency with XPS and XANES results. A more detailed inspection of Fig. 7.1 reveals that samples exhibit a resonance at $g = 2.005$, which was previously analyzed in Chap. 5.

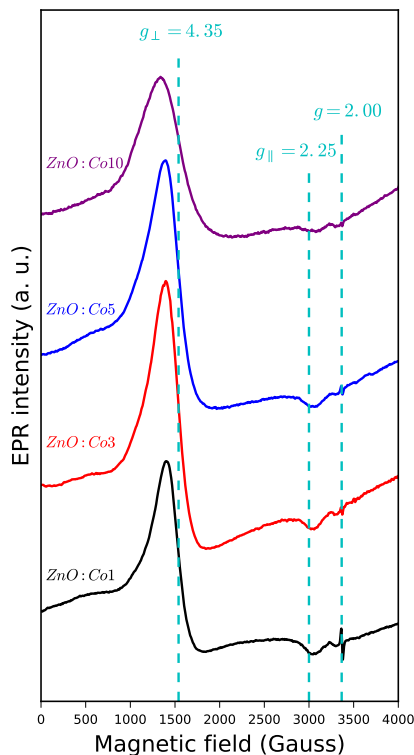


Fig. 7.1 100K EPR spectra of Co-doped ZnO NCs.

In Fig. 7.2 is shown the EPR spectra obtained at 100 K for Ni-doped ZnO NCs. It is observed a symmetric and broad resonance signals centered at around 3140 G ($g = 2.149$) and 3250 G ($g = 2.078$) for the ZnO:Ni1 and ZnO:Ni10 samples, respectively. It is clear that the amplitude of the EPR signals and the value of the resonant field increases while increasing the Ni concentration. When the nickel content increases, the average distance between Ni-Ni ions decreases and the super-exchange interactions between them change [4]. The EPR signal of the ZnO:Ni10 sample exhibits an intense resonance with $g = 2.078$. A broad signal due to long-range exchange

interactions of Ni^{2+} ions with g -values in the range of 2.2 to 2.57 were reported for Ni-doped ZnO nanoparticles [8, 9]. Considering the XANES results and reports in the literature [10–12], we suggest that the Ni^{2+} ions inside of the ZnO NCs occupy octahedrally-coordinated sites. It is known that in octahedrally-coordinated sites, Ni^{2+} ions show a spin configuration of $t_{2g}^{(\uparrow\uparrow\downarrow\downarrow\downarrow)} e_g^{(\uparrow\uparrow)}$. Assuming a low spin state, the spin configurations of Ni^{3+} ($3d^7$) and Ni^{4+} ($3d^6$) are $t_{2g}^{(\uparrow\uparrow\downarrow\downarrow\downarrow)} e_g^{(\uparrow)}$ and $t_{2g}^{(\uparrow\uparrow\downarrow\downarrow\downarrow)}$, respectively. Thus, Ni^{2+} and Ni^{3+} are magnetic but Ni^{4+} is a non-magnetic [13]. As the Ni^{2+} ions belong to $d^8(t_{2g}^6 e_g^2)$ configuration, the degenerate free ion ground state (3F) of Ni^{2+} splits as a consequence of the crystal field. In an octahedral environment, the orbital singlet $3A_{2g}$ has the lowest energy level. Using the spin-Hamiltonian: $H = g\beta HS$ with $S = 1$ and an isotropic g -factor, an isotropic line is obtained which corresponds to the $|0 \rightarrow -1 \pm 1 \rangle$ magnetic dipole transitions [11, 14].

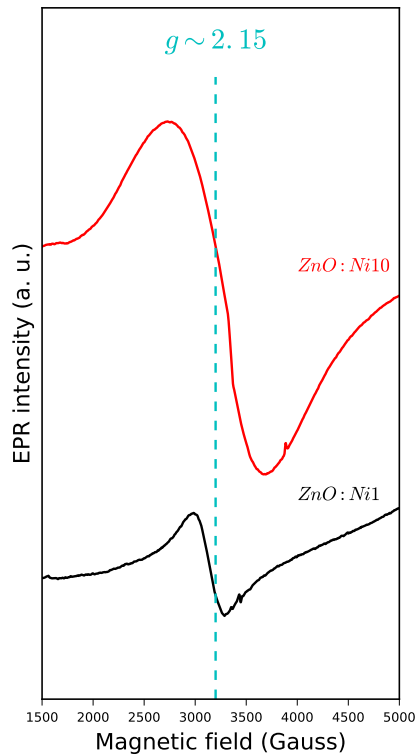


Fig. 7.2 100K EPR spectra of Ni-doped ZnO NCs.

It may be noted that EPR signal of most bulk antiferromagnetic materials disappears below its transition temperature due to the effect of very strong exchange fields, which require resonance frequencies higher than GHz region; then, the observed oscillations are not likely to be related with antiferromagnetic compounds. The bulk NiO is antifer-

romagnetic with a Néel temperature (T_N) of 520K [15], and non-stoichiometric NiO shows weak ferromagnetic [16] or super-paramagnetic (SPM) behavior at low temperatures due to the presence of Ni^{3+} ions in the sample [17, 18]. This could account for the obtained EPR spectra but we must consider that in the XPS and XANES analysis the main Ni oxidation state detected was the 2+. We will return to this discussion in the next section.

Table 7.1 List of calculated g-factors of the different EPR lines in doped ZnO NCs.

Sample	ν (MHz)	B (Gauss)	g
ZnO:Ni1	9436.409	3140	2.1489
ZnO:Ni3	9436.026	3210	2.0973
ZnO:Ni10	9439.623	3250	2.0784
ZnO:Co1	9448.475	1550	4.3554 (g_{\perp})
		2950	2.2864 (g_{\parallel})
ZnO:Co3	9442.356	1555	4.3386 (g_{\perp})
		2950	2.2845 (g_{\parallel})
ZnO:Co5	9440.516	1550	4.3518 (g_{\perp})
		2940	2.2929 (g_{\parallel})
ZnO:Co10	9437.226	1550	4.3503 (g_{\perp})
		2950	2.2896 (g_{\parallel})

7.2 Magnetization as a Function of the Temperature

In Fig. 7.3, 7.4 and 7.5 are shown DC susceptibility (χ_{DC}) curves as a function of temperature (T) for the Co-, Ni-, and Tb-doped ZnO NCs, respectively. As observed, the curves for all dopants show a paramagnetic behavior in agreement with results obtained from other experimental techniques. It is known that the paramagnetic behavior follows the Curie-Weiss law:

$$\chi = \chi_0 + C/(T - \theta), \quad (7.1)$$

Where χ_0 represents weak nonparamagnetic contributions, C is the Curie constant defined as:

$$C = N\mu_{eff}^2/3k_B, \quad (7.2)$$

N is the number of magnetic ions, μ_{eff} is the effective magnetic moment of the ion and θ is the Curie-Weiss temperature. The positive and negative values of θ correspond to ferromagnetic (FM) and antiferromagnetic (AFM) interactions, respectively [19]. No features indicating a phase transition was determined in the entire temperature range. All these parameters were determined by fitting the experimental data to the paramagnetic Curie-Weiss model.

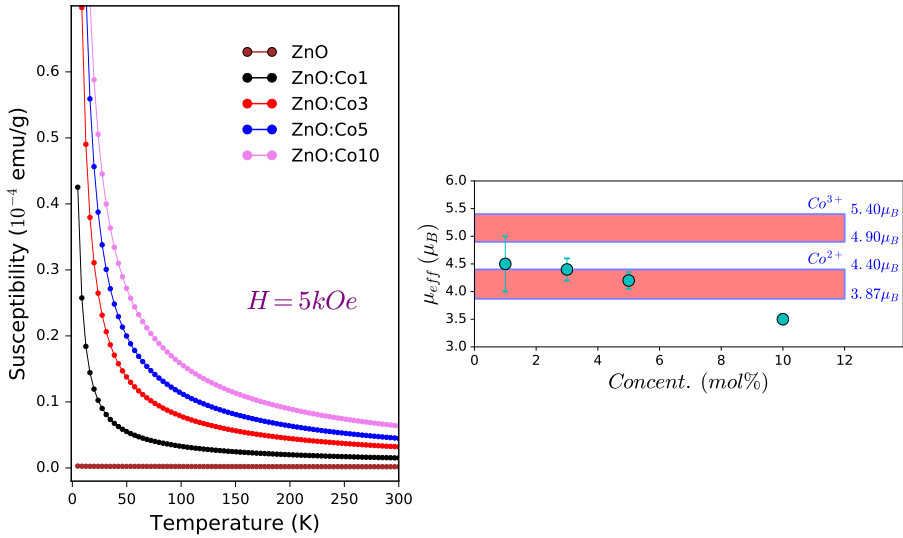


Fig. 7.3 (Left) DC susceptibility (χ_{DC}) curves as a function of temperature (T) obtained by applying a constant magnetic field of $H = 5$ kOe for the Co-doped ZnO NCs and, (right) Graphical result of the calculated effective magnetic moments.

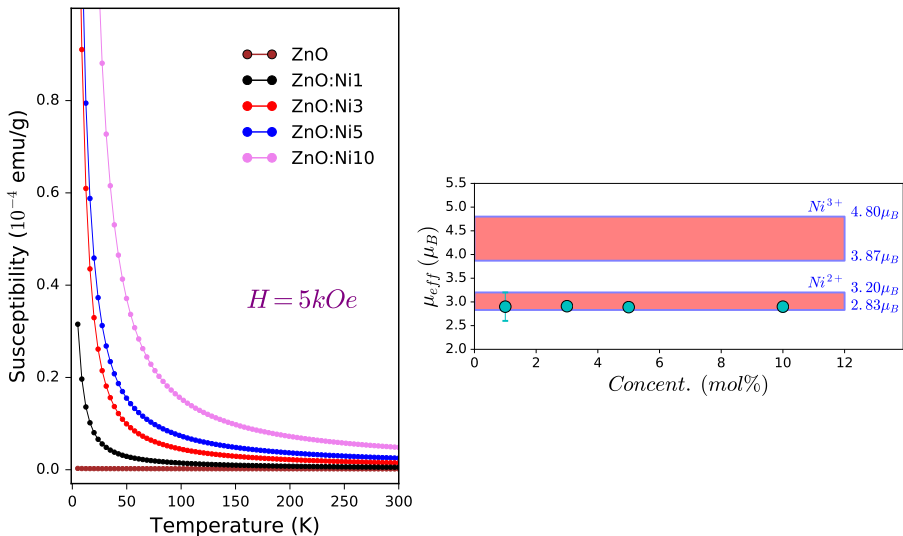


Fig. 7.4 (Left) DC susceptibility (χ_{DC}) curves as a function of temperature (T) obtained by applying a constant magnetic field of $H = 5$ kOe for the Ni-doped ZnO NCs and, (right) Graphical result of the calculated effective magnetic moments.

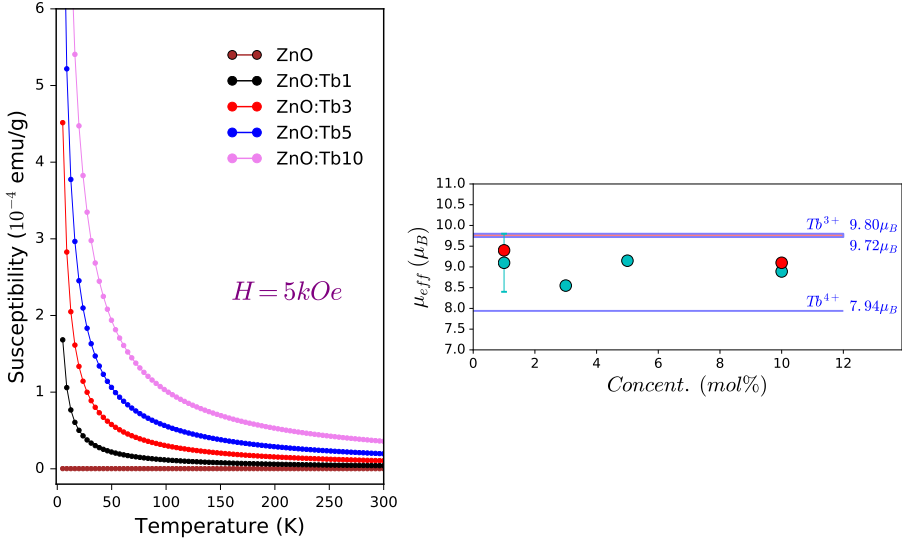


Fig. 7.5 (Left) DC susceptibility (χ_{DC}) curves as a function of temperature (T) obtained by applying a constant magnetic field of $H = 5$ kOe for the Tb-doped ZnO NCs and, (right) Graphical result of the calculated effective magnetic moments.

It is determined that the fitted parameters (C , θ , and χ_0) are very sensitive to the temperature range considered for the fit. Then, the analysis was done by considering different temperature ranges in order to establish acceptable criteria. The parameters' values versus the number of data points were plotted to identify the most suitable ranges with little variation of these parameters. Finally, the mean value and its standard deviation were calculated for each parameter. The obtained results showed an increase in C with the dopant content (x), as shown in Table 7.2, confirming the success in the progressive doping with Co, Ni, and Tb ions.

The theoretical effective magnetic moment is calculated using the equation:

$$\mu_{eff} = g\sqrt{J(J+1)}\mu_B, \quad (7.3)$$

where g is the Landé factor (usually $g = 2.0023$ for transition metals) and J the total magnetic moment ($J = S$ for transition metals due to the quenching of the orbit contribution [20]). Replacing the value of $S = 3/2$, the magnetic moment is $3.87\mu_B$ for a free Co^{2+} ion. On the other hand, we can estimate the isotropic value of $g = (2g_{\perp} + g_{\parallel})/3$ [5] using the g_{\perp} and g_{\parallel} values determined from EPR measurements (as shown in Sec. 7.1), we obtained a $g = 2.264$ for Co^{2+} ions. g values in the range of 2.24–2.31 were reported for Co in different dilute magnetic semiconductors (DMSs) [21], which is in accordance with our results.

In Table 7.2 we show the experimentally determined effective magnetic moment (μ_{eff}) calculated from the χ versus T curve shown in Fig. 7.3, 7.4 and 7.5. The experimental effective magnetic moments obtained for the Co-doped ZnO NCs, μ_{eff} , are 4.5,

4.4, 4.2, 3.5 μ_B for $x = 1, 3, 5$ and 10 mol%, respectively. These values are in line with the literature data of polycrystalline and single-crystal Co:ZnO [22]. Despite the values obtained in this work are slightly larger than the spin-only value of $3.87 \mu_B/Co^{2+}$, they are in agreement with the value estimated from EPR data ($4.4 \mu_B/Co^{2+}$). The value of $3.5 \mu_B/Co^{2+}$ for the sample with 10 mol% Co show an effective magnetic moment lower than the expected one and it was related to the compensating effect of the antiparallel alignment of spins which is enhanced due to the Co concentration in Co-doped ZnO samples. The antiparallel alignment is evidenced by the negative values of θ , which is driven by the super-exchange coupling between Co^{2+} ions occupying tetrahedral sites as will be discussed below.

A similar analysis was carried out for the Ni-doped ZnO NCs. In this case, the experiential magnetic moments were 2.9, 2.91, 2.89, 2.9 μ_B for Ni-doped samples with 1, 3, 5, 10 mol%, respectively (see Fig. 7.4). These values are consistent with the spin-only effective magnetic moment of free Ni^{2+} ions ($2.83 \mu_B$). The positive values of θ obtained for all Ni-doped samples indicate the occurrence of FM coupling between Ni^{2+} ions, opposite to that observed in the Co-doped ZnO NCs, where AFM coupling between Co^{2+} ions was determined. Considering the results presented so far, our analyses confirm the presence of Ni^{2+} ions in the Ni-doped ZnO NCs and excludes the presence of Ni^{3+} ions, which could account for the obtained EPR spectra of Ni-doped ZnO samples. Then, the observed EPR oscillations presented in Sec. 7.1 for Ni-doped ZnO samples could not be associated to the presence of Ni^{3+} ions on the surface of the NCs.

Table 7.2 List of parameters obtained from the fits of the susceptibility (χ_{DC}) vs. temperature (T) curves to the Curie-Weiss law. C is the Curie constant, μ_{eff} is the effective magnetic moment per dopant ion, θ is the Curie-Weiss temperature, and χ_0 is the temperature-independent susceptibility. The numbers in parentheses represent the estimated uncertainties.

Sample	C ($\times 10^{-4} \text{emuK/gOe}$)	θ (K)	χ_0 ($\times 10^{-7} \text{emu/gOe}$)	μ_{eff} (μ_B/Co)
ZnO:Co1	3.51(8)	-24 (2)	4.3 (2)	4.5 (5)
ZnO:Co3	8.8 (2)	-19 (2)	4.4 (3)	4.4 (2)
ZnO:Co5	13.6(3)	-24 (3)	3.0 (7)	4.20(15)
ZnO:Co10	18.3(2)	-22 (2)	6.6 (5)	3.50(9)
ZnO:Ni1	1.34(2)	2 (2)	8.9 (6)	2.9 (3)
ZnO:Ni3	3.92(6)	9.0(1.4)	1.3 (2)	2.91(2)
ZnO:Ni5	6.43(7)	8.3(9)	3.1 (2)	2.89(2)
ZnO:Ni10	12.2(4)	19 (2)	5 (1)	2.9 (1)

Sample	C ($\times 10^{-4} \text{emuK/gOe}$)	θ (K)	χ_0 ($\times 10^{-7} \text{emu/gOe}$)	μ_{eff} (μ_B/Co)	μ_{eff} (μ_B/Tb) (theoretical)
ZnO:Tb1	12.74(0.14)	-12(3)	0	9.1 (7)	9.4
ZnO:Tb3	32.6 (5)	-11(4)	0	8.55 (7)	-
ZnO:Tb5	60.8 (6)	-11(2)	0	9.15 (4)	-
ZnO:Tb10	111.2(8)	-10(2)	0	8.98 (3)	9.1

The magnetic moments obtained for Tb ions were 9.1, 8.55, 9.15, 8.98 μ_B , which are lower and higher than expected for Tb³⁺ ions (9.72 μ_B) and Tb⁴⁺ ions (7.94 μ_B), respectively (see Fig. 7.5). This is due to the fact that not only Tb³⁺ ions were found in Tb-doped ZnO NCs. In the XPS and XANES analysis, we concluded that the presence of Tb⁴⁺ ions cannot be excluded. Then, we calculate the fraction of each Tb ions using the XPS results to calculate the theoretical μ_{eff} expected for mixed magnetic moments. The experimental magnetic moments are compared in Table 7.2 to a theoretical value obtained from the expression;

$$\mu_{theoret}^2 = x\mu_1^2 + (1-x)\mu_2^2, \quad (7.4)$$

Here x refers to the fraction of Tb³⁺ and $1-x$ to that of Tb⁴⁺. μ_1 (9.72 μ_B) and μ_2 (7.94 μ_B) are the respective theoretical moments for these ions [23]. The experimental magnetic moment values obtained from magnetic measurements are similar to those expected theoretically—as depicted with the red data points observed in Fig. 7.5, which reinforces our hypothesis of mixing valence states in Tb-doped ZnO NCs.

The negative values of Curie temperature (θ) in samples doped with Co and Tb indicate local AFM interactions. In this scenario, we must consider the AFM behavior of the spinel Co₃O₄ and cubic CoO which have a Néel temperature of 40 K and 294 K, respectively [24, 25]. In the susceptibility versus temperature curves, we do not observe any evidence of magnetic transitions near to those temperatures. Therefore, we believe that the AFM behavior is not due to cobalt oxides but to the Co²⁺ ions dispersed in the ZnO matrix. According to Duan et al. [26] the Co²⁺ ions in ZnO matrix can be divided into three classes: (I) isolated Co²⁺ ions, which behave paramagnetically and contribute with the full spin-only moment m to the magnetization at low enough temperature and/or high enough applied field; (II) the Co²⁺ ions with at least one nearest-neighboring Co²⁺, which couple locally with the nearest Co²⁺ ions via AFM superexchange interaction. Pairs and most groups of four make no net contribution, while triplets contribute $m/3$ and large AFM coupled clusters of N atoms will make a contribution of $m/N^{1/2}$ [27]; and (III) the Co 2+ ions within the bound magnetic polarons (BMPs) model, which couple ferromagnetically within a BMP via the donor electron associated with defects and they also make a contribution to the magnetization. As we do not observe ferromagnetic coupling in our samples then BMP model does not apply here. A fact that can be used in favor of AFM superexchange interaction is the decreasing trend of the magnetic moment obtained for Co-doped samples (see Table 7.2 and Fig. 7.3). The μ_{eff} value for ZnO:Co1 was 4.5 μ_B and 3.5 μ_B for ZnO:Co10 sample showing a significant decrease. Based on a statistical dopant distribution, such a reduction stems from the antiferromagnetic coupling of Co–O–Co pairs in those samples and it is known to depend on the Co concentration [28].

Assuming a statistical dopant distribution in the wurtzite structure, different arrangements of the magnetic dopants are possible, some of which will be frustrated because the antiferromagnetic coupling cannot be satisfied for all atoms in tetrahedrally coordinated systems. For example, one can find different types of configurations; isolated Co dopant atoms (singles), Co–O–Co pairs, and open and closed Co–O–Co–O–Co triples. An open Co–O–Co–O–Co triple has one uncompensated spin.

It drives to a reduced effective magnetic moment of $1/3\mu(\text{Co})$, whereas frustrated spins occur in closed triples or tetrahedral quadruples. While a closed triple also drives to a reduced magnetic moment, the quadruple is magnetically fully compensated. At higher dopant concentrations larger Co–O–Co... configurations become increasingly important [29]. However, with the increase of the doping level, larger configurations cannot be neglected. The resulting total effective moment for low Co concentrations is thus dominated by the contribution of singles, whereas with increasing Co content the effective moment is strongly reduced due to the vanishing abundance of all small configurations. Obviously, the more atoms we include in the possible configurations, the lower the effective moment per Co will be [24]. By increasing the doping concentration the probability of creating antiferromagnetic pairs increases as well; therefore, reducing the amount of isolated Co ions. For higher doping concentrations the agreement becomes worse which is not surprising because the formation of antiferromagnetically coupled clusters may become more probable [30]. The antiferromagnetic coupling between Co nearest-neighbor has already been reported for bulk Co:ZnO crystals as well as for epitaxial films [9, 21, 24, 29–35]. We believe that this behavior also accounts for the interaction between Tb–Tb ions in the Tb-doped ZnO samples.

As mentioned above, the positive Curie temperature (θ) obtained in the Curie-Weiss analyses suggests that the interactions between Ni ions are of ferromagnetic nature in Ni-doped ZnO samples; then, we need to use an alternative explanation as compare with the Co-doped ZnO samples. The origin of the ferromagnetic interactions in ZnO-based DMSs is still in debate and has a number of possibilities. First, the presence of Ni metallic phase is an unlikely source of these ferromagnetic interactions because the synthesis of Ni-doped ZnO NCs is performed in an oxygen atmosphere where metallic Ni is unable to form [36]. Besides, the XPS, XANES and EPR analyses exclude the presence of metallic Ni. According to early results not reported here when metallic Ni was segregated and confirmed by XRD measurements, the ferromagnetism related to metallic Ni was very strong. The possibility that ferromagnetic interactions can originate from the NiO secondary phase formed in Ni-doped ZnO NCs have been considered previously in this chapter due that bulk NiO exhibits antiferromagnetism with a Néel temperature (T_N) of 520K [15, 37] and, in the nanocrystalline form it shows weak ferromagnetic [16] or super-paramagnetic (SPM) behavior at low temperature [17]. Some authors evidently confirm the existence of AFM nature in the pure NiO powder associated with $\text{Ni}^{2+}-\text{O}^{2-}-\text{Ni}^{2+}$ super-exchange interactions [38]. Although we do not observe a ferromagnetism or superparamagnetism indication in the M vs. H and M vs. T curves, the origin of the ferromagnetic interactions owing to NiO could not be excluded in our samples. However, an important aspect to be considered in favor that the ferromagnetic interactions come from the structural results. XRD and XAFS analyses showed a variation of the structural parameters when the dopant concentration was increased. As was suggested in the XANES and EPR analyses, the Ni^{2+} ions mainly occupy six-fold coordination octahedral sites. Taking a closer look at the ZnO wurtzite crystal structure, one sees that it contains large octahedral holes enclosed by oxygen atoms (see Fig. 2.2). The maximum radius of these unoccupied crystallographic positions is 0.88 Å, which is the theoretical upper limit size to accommodate an ion. Considering the ionic radii of Ni^{2+} (0.55 Å) it seems easy its incorporation

in the crystalline lattice. In addition, in ZnO the octahedrally coordinated interstitials (i.e., Zn_i and O_i) have lower defect formation energies than the tetrahedrally coordinated interstitials. Since these empty places can hold interstitial Zn ions—a widespread defect in ZnO, it is not unlikely that the observed EPR spectra correspond to octahedrally coordinated interstitial Ni^{2+} ions and that the ferromagnetic interactions result from the interaction of this Ni^{2+} ions. This type of defect has already been reported for other transition metals [39, 40]. Of course, we can not ignore the possibility to find Ni^{2+} ions in tetrahedral sites substituting Zn^{2+} ions. Furthermore, as the superexchange interaction is sensitive to bond angles and bond lengths, the position of Ni^{2+} in octahedral coordination along with the possibility to find Ni^{2+} in tetrahedral coordination, the ferromagnetic interaction can happen due to the different angles and bond length possibilities. These possibilities include the competition between AFM superexchange interaction (favored by 180° bond angles), FM superexchange interaction (favored by 90° Ni–O–Ni bond angles), and AFM direct exchange interaction (favored by short Ni–Ni distances) [41, 42]. AFM direct exchange is more favorable for configurations where Ni and Ni align directly with each other which not account for the proposed configuration (see 2.2). We believe that the FM interactions between Ni^{2+} ions determined for Ni-doped ZnO NCs are owing to the $\sim 90^\circ$ Ni–O–Ni bond angles.

7.3 Magnetization as a Function of the Applied Magnetic Field

The pure ZnO sample deserves more attention before to analyze the doped samples. In Fig. 7.6 we show an enlargement of the M versus H curve in which it is possible clearly observe an open hysteresis loop near the origin attributed to the uncompensated spins which are present due to the finite size effect, exhibiting a weak FM component. This experimental result is not surprising because we have obtained similar results in a previous work for the ZnO nanoparticles synthesized via different methods [43]. It is worth mentioning that we used high purity reagents and many precautions were taken in order to avoid contamination. This FM behavior is lost when doping is achieved. Some authors have attributed the ferromagnetism observed in ZnO NPs to oxygen-related defects, as shown in experimental and theoretical investigations [43–45]. However, some controversies remain respect to the origin of the ferromagnetism in non-doped ZnO, so some questions are opened and, therefore, more studies are needed.

In Fig. 7.7, 7.8, 7.9 and 7.10 the field-dependent magnetization curves are shown for all the studied ZnO samples, measured at 300 K and 5 K. The magnetization curves show no hysteresis, no remanence and no saturation up to 7 T, which is an indication of a paramagnetic behavior [46].

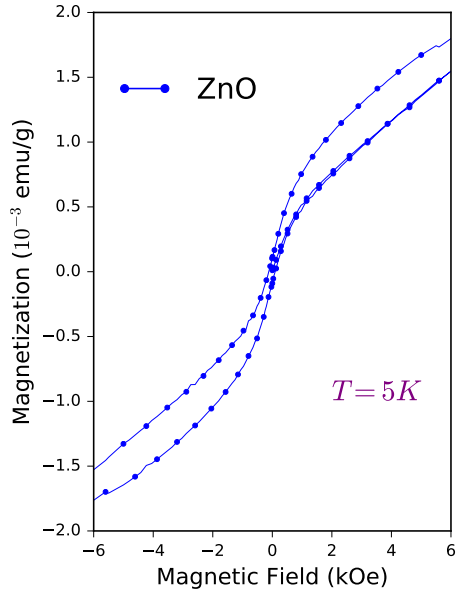


Fig. 7.6 Enlargement of magnetization (M) versus applied magnetic field (H) curve of pure ZnO NCs obtained at 5K.

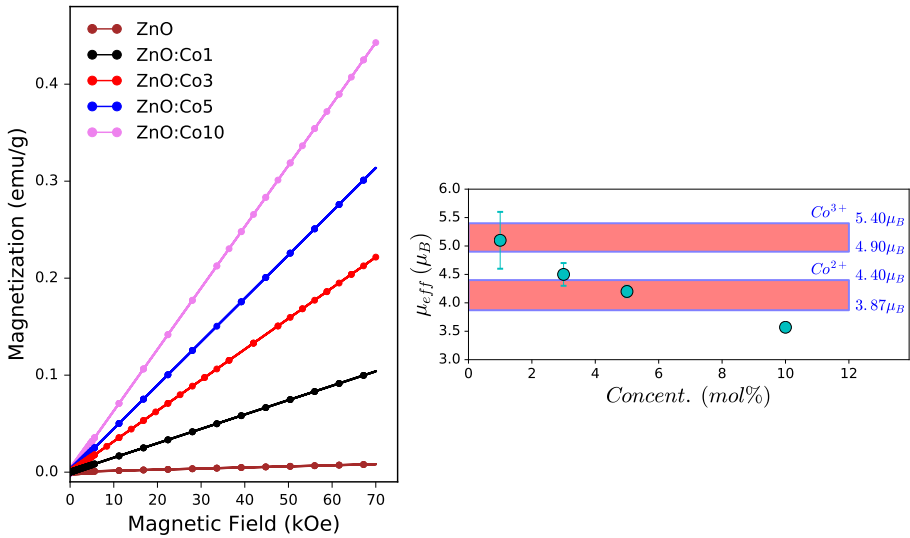


Fig. 7.7 (Left) Magnetization (M) versus applied magnetic field (H) curve obtained at 300 K for the Co-doped ZnO NCs and, (right) Graphical result of the calculated effective magnetic moments.

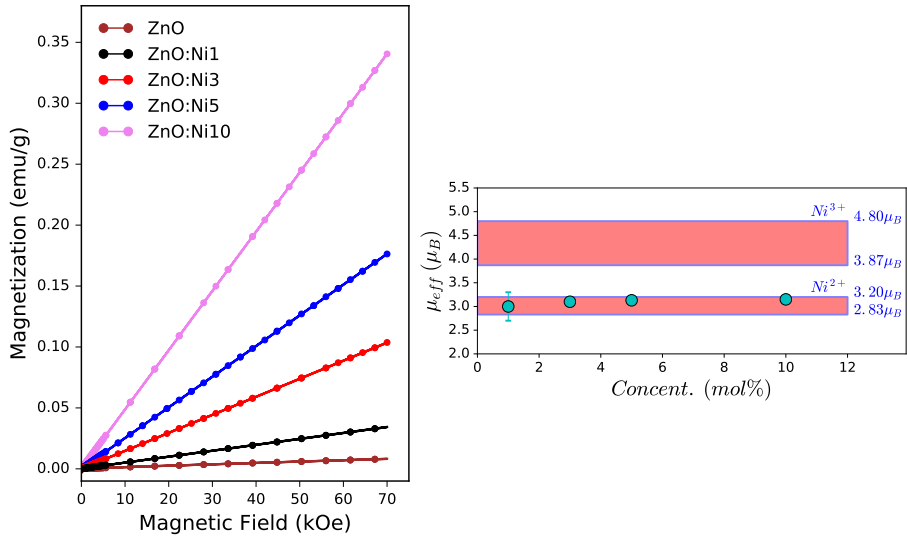


Fig. 7.8 (Left) Magnetization (M) versus applied magnetic field (H) curve obtained at 300 K for the Ni-doped ZnO NCs and, (right) Graphical result of the calculated effective magnetic moments.

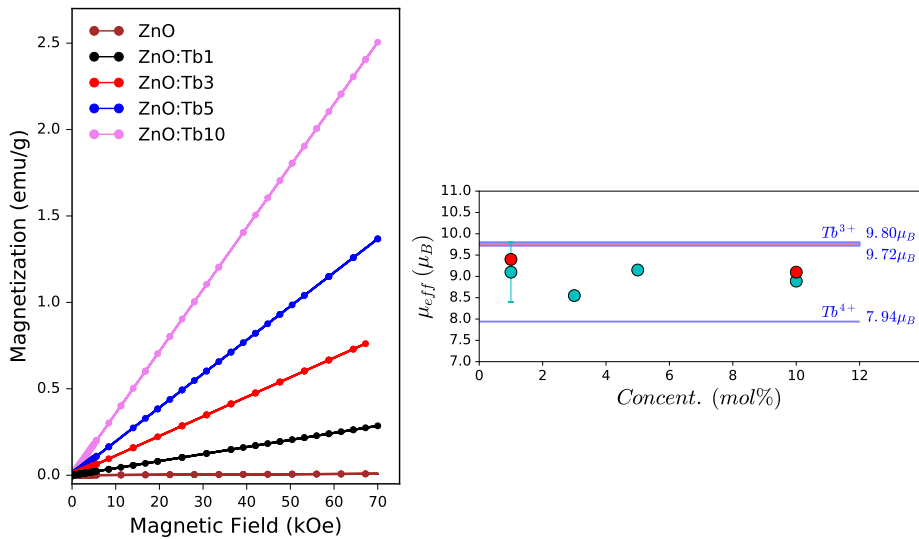


Fig. 7.9 (Left) Magnetization (M) versus applied magnetic field (H) curve obtained at 300 K for the Tb-doped ZnO NCs and, (right) Graphical result of the calculated effective magnetic moments.

From the experimental data at 300 K it is possible to observe a linear behavior, which indicates a paramagnetic behavior. The magnetization at high temperatures is then given by:

$$M = \frac{Ng^2J(J+1)\mu_B^2H}{3k_B T} = \frac{C}{T}H, \quad (7.5)$$

where the curie constant, C is:

$$C = \frac{Ng^2J(J+1)\mu_B^2}{3k_B} = \frac{\mu_{eff}^2}{3k_B}, \quad (7.6)$$

and the effective magnetic moment, μ_{eff} :

$$\mu_{eff} = g\sqrt{J(J+1)}\mu_B \quad (7.7)$$

Then, from the slope of the M vs. H curves, one can determine the effective magnetic moment. The obtained values are reported in Table 7.3 and are consistent with those ones obtained from the temperature dependence of the DC susceptibility.

Table 7.3 List of parameters obtained from the fits of the magnetization(M) vs. applied magnetic field (H) measured at 300K. C is the Curie constant, μ_{eff} is the effective magnetic moment per dopant ion. The numbers in parentheses represent the uncertainties.

Sample	C ($\times 10^{-4} emuK/gOe$)	μ_{eff} (μ_B/Co)
ZnO:Co1	4.4600 (5)	5.1 (5)
ZnO:Co3	9.5000 (7)	4.5 (2)
ZnO:Co5	13.4000(9)	4.2 (1)
ZnO:Co10	19.000 (1)	3.57(7)
ZnO:Ni1	1.480 (1)	3.0 (3)
ZnO:Ni3	4.4400(3)	3.1 (1)
ZnO:Ni5	7.5600(8)	3.13(7)
ZnO:Ni10	14.600(1)	3.15(6)
ZnO:Tb1	12.2000(8)	8.9 (7)
ZnO:Tb3	34.000 (2)	8.7 (2)
ZnO:Tb5	58.700 (4)	9.0 (2)
ZnO:Tb10	107.400(7)	8.83(8)

From curves shown in Fig. 7.10, it is possible to note that the slope of the curves, as well as the respective saturation magnetization (M_s) values increase as the dopant concentration is increased. As a result, the magnetization curves tend to a single curve indicating the existence of a normal paramagnetism behavior in these NCs. Zero remanent magnetization and zero coercive fields were observed here for all the doped ZnO samples.

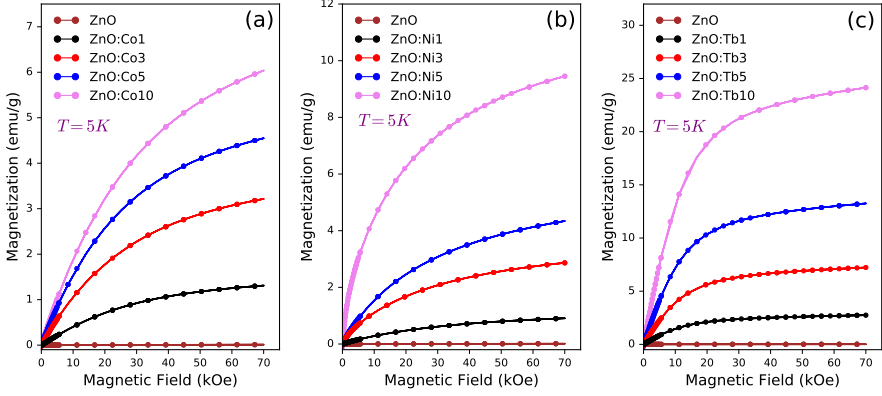


Fig. 7.10 Magnetization (M) versus applied magnetic field (H) curves obtained at 5K for the doped ZnO NCs.

M vs H curves at 5K (see Fig. 7.10) were fitted with the expression:

$$M = M_s B_s(g\mu_B SH/k_B T), \quad (7.8)$$

where M_s ($M_s = Ng\mu_B S/V$) is the saturation magnetization, $g = 2.0023$ is the spectroscopic splitting factor, μ_B is the Bohr magneton, k_B is the Boltzmann constant and B_s is the Brillouin-function-based form for a paramagnetic system, given by [20]:

$$B_s(x) = \frac{2S+1}{2S} \coth\left\{\frac{(2S+1)x}{2S}\right\} - \frac{1}{2S} \coth\left(\frac{x}{2S}\right) \quad (7.9)$$

The experimental value of the spin obtained from the fit of data (see Fig. 7.11) for the 1 mol% Co-doped sample was $S = 1.88$, which is very close to the spin of Co^{2+} ions ($S = 1.5$) and confirms that in the paramagnetic regime the magnetic moments of the Co^{2+} ions behave as isolated. This result confirms the hypothesis that for low Co concentrations the resulting total effective moment is dominated by the contribution of singles, and thus Co^{2+} ions behave as isolated. Whereas with the increase of Co content, the effective moment is strongly reduced due to the vanishing of the small configurations. The same procedure using the Brillouin function was attempted for the other samples obtained unsatisfactory results. It seems that the FM interactions determined for the Ni-doped ZnO samples affect the ideal paramagnet behavior and the mixed valence $\text{Tb}^{3+}/\text{Tb}^{4+}$ in the Tb doped samples drives to mixing paramagnetic behavior.

It is clear that sample ZnO:Co3 do not show any evidence of ferromagnetic order at room temperature and down to 5 K, as shown in Fig. 7.7 and 7.10(a), respectively.

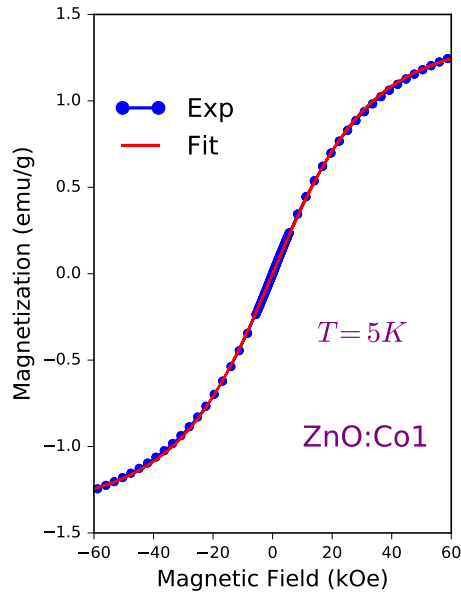


Fig. 7.11 Magnetization (M) versus applied magnetic field (H) curve fitted using the Brillouin function. Dots represent experimental data and straight line the fit result.

Surprisingly, after a thermal treatment of sample ZnO:Co3 at 400 °C during 4 hours in a hydrogen atmosphere (sample ZnO:Co3H), it shows open hysteresis loop near the origin indicating a weak FM contribution, which coexists with a non-saturated contribution coming from the remaining paramagnetic behavior. That is, the mean contribution continues to be due to the paramagnetic behavior. The XRD and HRTEM data analyses for sample ZnO:Co3H indicated that not additional secondary phases are presented and that the wurtzite crystalline structure remains after the thermal treatment in a hydrogen atmosphere. The d -spacing fingerprints were associated with the (002) plane of the ZnO structure (see Fig. 7.12). Besides, the EPR data analysis indicates that the spectrum is the same as that obtained for the not thermally-treated sample. We can conclude that the Co^{2+} ions remain in the tetrahedral site of the ZnO matrix as previously pointed out. It indicates the possibility to improve the magnetic response by subjecting the doped ZnO NCs to thermal treatment under controlled atmosphere. Some reports indicate that the ferromagnetic properties have a strong correlation with oxygen vacancies [47]. Of course, convincing explanation for the origin of RTFM is our further work.

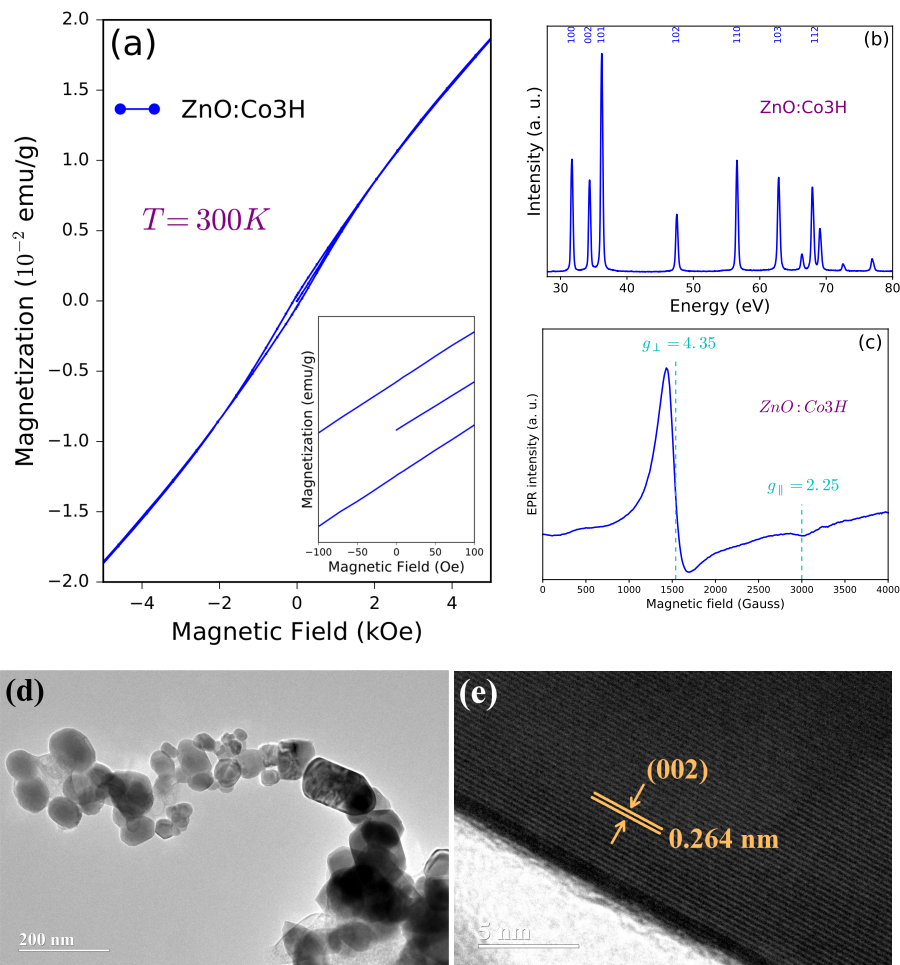


Fig. 7.12 Results obtained for ZnO:Co₃ sample thermal-treated at 400 °C in hydrogen atmosphere: (a) Magnetization versus magnetic applied field curve measured at 300 K, (b) X-ray diffraction patterns, (c) 100 K EPR measurements, and (d, e) HRTEM results.

References

1. Guylhaine Clavel, M-G Willinger, David Zitoun, and Nicola Pinna. Solvent dependent shape and magnetic properties of doped ZnO nanostructures. *Adv. Funct. Mater.*, 17(16):3159–3169, 2007.
2. Alessandro Bencini, Carlo A Ghilardi, Annabella Orlandini, Stefano Midollini, and Claudia Zanchini. Electronic structure of paramagnetic clusters of transition metal ions. 2. Crystal and molecular structure, single crystal EPR spectra, and magnetic properties of $[Co_6(\mu_3 - S)_8(PEt_3)_6](PF_6)$. *J. Am. Chem. Soc.*, 114(25):9898–9908, 1992.
3. Roberto Della Pergola, Alessandro Fumagalli, Fabrizia Fabrizi de Biani, Luigi Garlaschelli, Franco Laschi, Maria Carlotta Malatesta, Mario Manassero, Elena Roda, Mirella Sansoni, and

- Piero Zanello. Carbonyl-Nitrido Mixed-Metal Clusters: Synthesis, Reactivity, Electrochemical Behavior and Solid-State Structure of [Co₅MoN (CO) 14] 2- and [Co₅MoN (CO) 14AuPPh₃]-. *Eur. J. Inorg. Chem.*, 2004(19):3901–3906, 2004.
- Nathalie Jedrecy, HJ Von Bardeleben, Y Zheng, and JL Cantin. Electron paramagnetic resonance study of Zn_{1-x}CoxO: A predicted high-temperature ferromagnetic semiconductor. *Phys. Rev. B*, 69(4):041308, 2004.
 - P Sati, R Hayn, R Kuzian, S Régnier, S Schäfer, A Stepanov, C Morhain, C Deparis, M Läugt, M Goiran, et al. Magnetic anisotropy of Co²⁺ as signature of intrinsic ferromagnetism in ZnO:Co. *Phys. Rev. Lett.*, 96(1):017203, 2006.
 - TJ Chuang, CR Brundle, and DW Rice. Interpretation of the x-ray photoemission spectra of cobalt oxides and cobalt oxide surfaces. *Surf. Sci.*, 59(2):413–429, 1976.
 - C Oliva, S Cappelli, A Kryukov, GL Chiarello, AV Vishniakov, and L Forni. Effect of preparation parameters on the properties of La_{0.9}Ce_{0.1}CoO₃ catalysts: An EMR investigation. *J. Mol. Catal. A: Chem.*, 255(1-2):36–40, 2006.
 - Rosari Saleh, Nadia Febiana Djaja, and Suhendro Purbo Prakoso. The correlation between magnetic and structural properties of nanocrystalline transition metal-doped ZnO particles prepared by the co-precipitation method. *J. Alloys Compd.*, 546:48–56, 2013.
 - P Sati, A Stepanov, and V Pashchenko. Exchange broadening of EPR line in ZnO:Co. *J. Low Temp. Phys.*, 33(11):927–930, 2007.
 - B Babu, G Rama Sundari, K Ravindranadh, M Rajesh Yadav, and RVSSN Ravikumar. Structural, spectroscopic and magnetic characterization of undoped, Ni²⁺-doped ZnO nanopowders. *J. Magn. Magn. Mater.*, 372:79–85, 2014.
 - RVSSN Ravikumar, J Yamauchi, AV Chandrasekhar, YP Reddy, and P Sambasiva Rao. Identification of chromium and nickel sites in zinc phosphate glasses. *J. Mol. Struct.*, 740(1-3):169–173, 2005.
 - B Sreedhar, CH Sumalatha, and K Kojima. ESR and optical absorption spectra of Ni (II) ions in lithium fluoroborate glasses. *J. Mater. Sci.*, 31(6):1445–1448, 1996.
 - Duong Van Thiet, Duc Cuong Do, Luong Huu Bac, Viet Cuong Le, Ha Dang Khoa, Sunglae Cho, Nguyen Hoang Tuan, and Dang Duc Dung. Room-temperature ferromagnetism in Nickel-doped wide band gap ferroelectric Bi_{0.5}K_{0.5}TiO₃ nanocrystals. *Mater. Trans.*, 56(9):1339–1343, 2015.
 - John Wertz. *Electron spin resonance: elementary theory and practical applications*. Springer Science & Business Media, 2012.
 - Javed Iqbal, Baiqi Wang, Xiaofang Liu, Dapeng Yu, B He, and Ronghai Yu. Oxygen-vacancy-induced green emission and room-temperature ferromagnetism in Ni-doped ZnO nanorods. *New journal of physics*, 11(6):063009, 2009.
 - Issei Sugiyama, Naoya Shibata, Zhongchang Wang, Shunsuke Kobayashi, Takahisa Yamamoto, and Yuichi Ikuhara. Ferromagnetic dislocations in antiferromagnetic NiO. *Nature nanotechnology*, 8(4):nnano–2013, 2013.
 - Rezaq Naji Aljawfi and S Mollah. Properties of Co/Ni codoped ZnO based nanocrystalline DMS. *J. Magn. Magn. Mater.*, 323(23):3126–3132, 2011.
 - M Kakazey, M Vlasova, Y Vorobiev, I Leon, M Cabecera Gonzalez, and Edgar Arturo Chávez Urbiola. Processes of microstructural evolution during high-energy mechanical treatment of ZnO and black NiO powder mixture. *Physica B: Condensed Matter*, 453:116–122, 2014.
 - A Manivannan, MS Seehra, SB Majumder, and RS Katiyar. Magnetism of Co-doped titania thin films prepared by spray pyrolysis. *Appl. Phys. Lett.*, 83(1):111–113, 2003.
 - Nicola A Spaldin. *Magnetic materials: fundamentals and applications*. Cambridge University Press, 2010.
 - S Kolesnik, B Dabrowski, and J Mais. Structural and magnetic properties of transition metal substituted ZnO. *J. Appl. Phys.*, 95(5):2582–2586, 2004.
 - Wei Li, Qingqing Kang, Zhang Lin, Wangsheng Chu, Dongliang Chen, Ziyu Wu, Yu Yan, Dagui Chen, and Feng Huang. Paramagnetic anisotropy of Co-doped ZnO single crystal. *Appl. Phys. Lett.*, 89(11):112507, 2006.
 - JB MacChesney, HJ Williams, RC Sherwood, and JF Potter. Preparation and Low-Temperature Magnetic Properties of the Terbium Oxides. *J. Chem. Phys.*, 44(2):596–601, 1966.

24. V Ney, B Henne, J Lumetzberger, F Wilhelm, K Ollefs, A Rogalev, A Kovacs, M Kieschnick, and A Ney. Coalescence-driven magnetic order of the uncompensated antiferromagnetic Co doped ZnO. *Phys. Rev. B*, 94(22):224405, 2016.
25. A Ney, András Kovács, V Ney, S Ye, K Ollefs, T Kammermeier, F Wilhelm, A Rogalev, and Rafal E Dunin-Borkowski. Structural, chemical and magnetic properties of secondary phases in Co-doped ZnO. *New Journal of Physics*, 13(10):103001, 2011.
26. LB Duan, WG Chu, J Yu, YC Wang, LN Zhang, GY Liu, JK Liang, and GH Rao. Structural and magnetic properties of $Zn_{1-x}Co_xO$ ($0 \leq x \leq 0.30$) nanoparticles. *J. Magn. Magn. Mater.*, 320(8):1573–1581, 2008.
27. M Venkatesan, CB Fitzgerald, JG Lunney, and JMD Coey. Anisotropic ferromagnetism in substituted zinc oxide. *Physical review letters*, 93(17):177206, 2004.
28. Jason Hays, KM Reddy, NY Graces, Mark H Engelhard, V Shutthanandan, M Luo, Changqing Xu, NC Giles, C Wang, Suntharampillai Thevuthasan, et al. Effect of Co doping on the structural, optical and magnetic properties of ZnO nanoparticles. *J. Phys.: Condens. Matter*, 19(26):266203, 2007.
29. Bastian Henne, Verena Ney, Mariano de Souza, and Andreas Ney. Exchange-bias-like effect of an uncompensated antiferromagnet. *Phys. Rev. B*, 93(14):144406, 2016.
30. M Bouloudenine, N Viart, S Colis, J Kortus, and A Dinia. Antiferromagnetism in bulk Zn 1- x Co x O magnetic semiconductors prepared by the coprecipitation technique. *Appl. Phys. Lett.*, 87(5):052501, 2005.
31. A Ney, K Ollefs, S Ye, T Kammermeier, V Ney, Tiffany C Kaspar, Scott A Chambers, F Wilhelm, and A Rogalev. Absence of intrinsic ferromagnetic interactions of isolated and paired Co dopant atoms in Zn1- xCoxO with high structural perfection. *Phys. Rev. Lett.*, 100(15):157201, 2008.
32. Martin Buchner, Bastian Henne, Verena Ney, Julia Lumetzberger, Fabrice Wilhelm, Andrei Rogalev, Amir Hen, and Andreas Ney. Pinned orbital moments in uncompensated antiferromagnetic Co-doped ZnO. *J. Appl. Phys.*, 123(20):203905, 2018.
33. P Sati, C Deparis, C Morhain, S Schäfer, and A Stepanov. Antiferromagnetic interactions in single crystalline Zn 1- xCoxO thin films. *Phys. Rev. Lett.*, 98(13):137204, 2007.
34. V Ney, K Lenz, K Ollefs, F Wilhelm, A Rogalev, and A Ney. Role of preparation and implantation-related defects for the magnetic properties of $Zn_{0.9}Co_{0.1}O$ epitaxial films. *J. Appl. Phys.*, 116(4):043912, 2014.
35. SW Yoon, S-B Cho, SC We, S Yoon, BJ Suh, HK Song, and YJ Shin. Magnetic properties of ZnO-based diluted magnetic semiconductors. *J. Appl. Phys.*, 93(10):7879–7881, 2003.
36. A Sayari and L El Mir. Annealing and Ni content effects on EPR and structural properties of Zn1-xNi xO aerogel nanoparticles. *Materials Science-Poland*, 35(3):454–462, 2017.
37. Xiaoxue Liu, Fangting Lin, Linlin Sun, Wenjuan Cheng, Xueming Ma, and Wangzhou Shi. Doping concentration dependence of room-temperature ferromagnetism for Ni-doped ZnO thin films prepared by pulsed-laser deposition. *Appl. Phys. Lett.*, 88(6):062508, 2006.
38. Patta Ravikumar, Bhagaban Kisan, and A Perumal. Enhanced room temperature ferromagnetism in antiferromagnetic NiO nanoparticles. *Aip Advances*, 5(8):087116, 2015.
39. Petra Lommens, Frank Loncke, Philippe F Smet, Freddy Callens, Dirk Poelman, Henk Vrielinck, and Zeger Hens. Dopant incorporation in colloidal quantum dots: a case study on Co²⁺ doped ZnO. *Chem. Mater.*, 19(23):5576–5583, 2007.
40. A Fouchet, W Prellier, P Padhan, Ch Simon, B Mercey, VN Kulkarni, and T Venkatesan. Structural and magnetic properties of a series of low-doped $Zn_{1-x}Co_xO$ thin films deposited from Zn and Co metal targets on (0001) Al₂O₃ substrates. *Journal of applied physics*, 95(11):7187–7189, 2004.
41. Guangqing Pei, Changtai Xia, Bo Wu, Tao Wang, Lili Zhang, Yongjun Dong, and Jun Xu. Studies of magnetic interactions in Ni-doped ZnO from first-principles calculations. *Computational Materials Science*, 43(3):489–494, 2008.
42. David Jiles. *Introduction to magnetism and magnetic materials*. CRC press, 2015.
43. A Sundaresan, R Bhargavi, N Rangarajan, U Siddesh, and CNR Rao. Ferromagnetism as a universal feature of nanoparticles of the otherwise nonmagnetic oxides. *Physical Review B*, 74(16):161306, 2006.

44. Peng Zhan, Zheng Xie, Zhengcao Li, Weipeng Wang, Zhengjun Zhang, Zhuoxin Li, Guodong Cheng, Peng Zhang, Baoyi Wang, and Xingzhong Cao. Origin of the defects-induced ferromagnetism in un-doped ZnO single crystals. *Applied Physics Letters*, 102(7):071914, 2013.
45. IS Elfimov, S Yunoki, and GA Sawatzky. Possible path to a new class of ferromagnetic and half-metallic ferromagnetic materials. *Physical review letters*, 89(21):216403, 2002.
46. SM Yusuf, M Sahana, K Dörr, UK Röbller, and K-H Müller. Effect of Ga doping for Mn on the magnetic properties of La_{0.67}Ca_{0.33}MnO₃. *Phys. Rev. B*, 66(6):064414, 2002.
47. Zhou ShaoMin, Yuan HongLei, Liu LiSheng, Chen XiLiang, Lou ShiYun, Hao YaoMing, Yuan RuiJian, and Li Ning. Magnetic properties of Ni-doped ZnO nanocombs by CVD approach. *Nanoscale research letters*, 5(8):1284, 2010.

Chapter 8

Conclusions and Future Work

8.1 Conclusions

In this thesis, we have performed an extensive study of the structural, electronic, optical and magnetic properties of pure and doped ZnO NCs that was elaborated by the correlation of results obtained from diverse experimental techniques. Conventional macroscopic techniques, among those, XRD, HRTEM, XPS, PL, EPR and SQUID-based magnetometry; and element-specific advanced tools (i.e. XANES and XAFS) were used. The main findings for the pure and doped ZnO NCs studied here are summarized as follows:

- We have synthesized successfully Ni-, Co-, and Tb-doped ZnO compounds with nanocrystal sizes via a sol-gel method. The XRD and HRTEM measurements confirmed the formation of the wurtzite ZnO structure with mean sizes of 7.3, 7.3, 6.5 nm for Ni, Co, and Tb-doped ZnO NCs, showing mostly circular and elliptical shapes. The no detection of secondary phases containing nickel, cobalt, and terbium within the limit of the detection technique strongly shows that the synthesis method is much efficient to obtain pure and doped ZnO NCs. Moreover, a decreasing tendency in the a-lattice parameter and an increase in the c-lattice parameter for the Ni- and Co-doping are found to be related to the incorporation of dopant ions into the ZnO matrix. However, both a and c lattice parameters showed an unexpected decreasing tendency for terbium doping, which was related to the formation of Tb-related defect complexes in the ZnO matrix.
- The Zn K-edge EXAFS spectrum oscillations of pure ZnO matched-well with those related to bulk ZnO, suggesting minor structural differences. The decrease in the peak intensity related to Zn–Zn contributions evidences a decrease in the coordination number around the zinc ions when dopant content is increased and; therefore, it was attributed to the arising of zinc vacancies. In addition, the EXAFS results at the Co K-edge showed similar features to those of the Zn K-edge for the pure ZnO NCs, which evidence that Co ions substitute Zn ions in the tetrahedral sites of the host lattice. The EXAFS results at the Ni K-edge and Tb L3-edge showed marked differ-

ences in comparison to those obtained at the Zn K-edge suggesting modifications in the Ni and Tb local environment. On the other hand, XPS and XANES results at the Co K-edge indicated that Co ions assume predominantly the 2+ valence state and are mostly located in tetrahedral sites, which is consistent with the Co K-edge EXAFS results. The results obtained at the Ni K-edge indicated the presence of Ni²⁺ but located mainly at octahedral sites of the ZnO wurtzite structure. A similar analysis suggested that Tb ions are established in a mixed valence state (3+/4+).

- From EPR data analysis, mainly two predominant paramagnetic defects were observed in all set of samples. The intensity of the $g = 2.005$ signal reduces almost until disappearing with the increase of the Co in Co-doped ZnO NCs, revealing a decrease in the number of superficial defects. That tendency was lower for Tb doped samples. Besides, the line shape of the $g = 1.961$ signal increases significantly with the increase of the dopant concentration in the Tb-doped samples, behavior that was not detected for the other dopants. The appearance of this signal was assigned to the formation of EPR-detected oxygen vacancies due to the difference in ionic sizes of Tb³⁺ and Zn²⁺, which are the responsible for the lattice parameters decrease determined from XRD and XAFS data analysis.
- All the studied samples showed photoluminescence spectra with some specific features. UV emission bands centered in the range between 350–450 nm, which correspond to the near-band emission attributed to the photo-stimulated creation of excitons having energies just below the ZnO band-edge. Besides, a broad green emission band (450–650 nm) related to oxygen vacancies ($V_O^{\bullet\bullet}$). It is determined that as the Co content is increased, the intensity of this green emission decreases and to a lesser extent for Ni and Tb doping. This decreasing trend was assigned to the density reduction of the V_O^{\bullet} defects, in agreement with the similar trend determined for the EPR signal of the $g = 2.005$ region. A red emission band was also observed in all the samples in the region 700–800 nm, which are ascribed to the interstitial Zn ions in the NCs. In the Co-doped ZnO NCs, it was observed an additional red emission band at around 661 nm which has been assigned to the characteristic transition of the Co²⁺ ions occupying tetrahedral sites (i.e., ${}^4T_1(P) \rightarrow {}^4A_2(F)$ $d-d^*$ internal transitions). When the terbium ions are introduced into the ZnO matrix, it was determined a carrier relaxation from the excited states of the ZnO host to the Tb ions, which results in characteristic emissions (intra-ions transitions) of Tb³⁺ ions in the ZnO matrix.
- An intense and broad EPR resonance located at $g_{\perp} = 4.35$ and a weaker band at $g_{\parallel} = 2.29$ corroborate the presence of Co²⁺ (with $S = 3/2$) in agreement with the optical and magnetic results. The EPR resonance located at $g \sim 2.11$ observed in the Ni-doped ZnO NCs confirms the presence of Ni²⁺ occupying octahedrally-coordinated sites.
- Magnetic measurements revealed a paramagnetic behavior for the doped ZnO NCs, with the exception of pure ZnO NCs, which show a weak ferromagnetic behavior.

The data analysis revealed the presence of Co^{2+} ($3.87 \mu_B$), Ni^{2+} ($2.83 \mu_B$) and the coexistence of $\text{Tb}^{3+}/\text{Tb}^{4+}$ ($9.72 \mu_B/7.94 \mu_B$) in the Co-, Ni-, and Tb-doped ZnO samples, respectively, in agreement with results obtained from other techniques. Besides, Co and Tb dopant ions show local AFM correlations favored by the statistical distribution of the dopant ions in the ZnO semiconducting matrix and the Ni–Ni interactions were determined as FM in Ni-doped ZnO NCs.

8.2 Future Work

We consider important to mention that there are still some open questions regarding the study of the pure and doped ZnO NCs systems that we describe in this work.

- For determining the different type of defects in the ZnO matrix and the role of them in the emission process and other properties, our investigation has to be continued by including electron paramagnetic resonance measurements under UV irradiation. Some of the defects can behave actively when irradiated and this could lead to the identification of point defects when combined with PL and PL with applied magnetic field measurements. Raman measurements varying the temperature and applied magnetic field could be an interesting tool to decipher the nature of the defects.
- Thermal treatment of the NCs under different atmospheres (i.e., O_2 , N_2 , H_2 or Ar) to study the suppressing of some EPR signals and get a better understanding about the nature of the defects and the photoluminescence emission process. This thermal process in a controlled atmosphere could lead to the desired p-type ferromagnetic behavior.
- Simulations of the XANES and EXAFS spectra with the FEFF code in order to include a more detailed description of the behavior of oxygen and zinc vacancies when increasing the dopant concentration of doped ZnO NCs.
- Studies with time-resolved XAS could be used to probe changes in the unoccupied density of states (DOS), which includes the conduction band of semiconductors; these studies are sensitive to the excitation and trapping of the electrons. Due to the fact that the valence band is dominated by the oxygen 2p orbitals the hole cannot be observed in transition metal oxides making it almost impossible to detect by X-ray or optical absorption. To address this, XAS can be complemented by X-ray emission spectroscopy (XES) to provide information about the time evolution of the occupied DOS, which corresponds to the semiconductor valence band.

Appendix A

A.1 A Brief Theory and Analysis of EXAFS

For the analysis of the EXAFS data presented in this thesis, the Athena and Artemis software of the Demeter package ¹, have been used. These programs include AUTOBK [1] for background removal, FEFF [2] for generation of the theoretical EXAFS models, and FEFFIT [3] for parameter optimization of the model.

A typical XAFS spectrum of powder ZnO (recorded in the transmission geometry at the XAFS1 beamline at LNLS) is shown in Fig. A.1. The sharp rise in $\mu(E)$ due to the Zn1s electron level (at 9659.0 eV) is clearly visible in the spectra and the XAFS oscillations. As mentioned in the Chap. 2, the XAFS is generally thought of in two different regions: the near-edge spectra (XANES) and the extended fine-structure (EXAFS). The basic physical description of these two regimes is the same, but some important approximations and limits allow us to interpret the extended spectra in a more quantitative way than is currently possible for the near-edge spectra [4].

For the EXAFS, we are interested in the oscillations well above the absorption edge, and define the EXAFS fine-structure function $\chi(E)$, as a change to $\mu(E)$ [5].

$$\mu(E) = \mu_0(E)[1 - \chi(E)] \quad (\text{A.1})$$

where $\mu(E)$ is the measured absorption coefficient, $\mu_0(E)$ is a smooth background function representing the absorption of an isolated atom. The isolated XAFS is usually written as:

$$\chi(E) = \frac{\mu(E) - \mu_0(E)}{\Delta\mu_0(E)} \quad (\text{A.2})$$

where $\Delta\mu_0$ is the measured jump in the absorption $\mu(E)$ at the threshold energy (see Fig. A.1). χ forms the oscillatory part of the total absorption, describing the scattering of the outgoing electron against the neighboring atoms. Since the oscillatory part is created by the interference between the outgoing and backscattered waves, it contains information about the local structure around the absorber atom.

¹ <https://github.com/bruceravel/demeter>

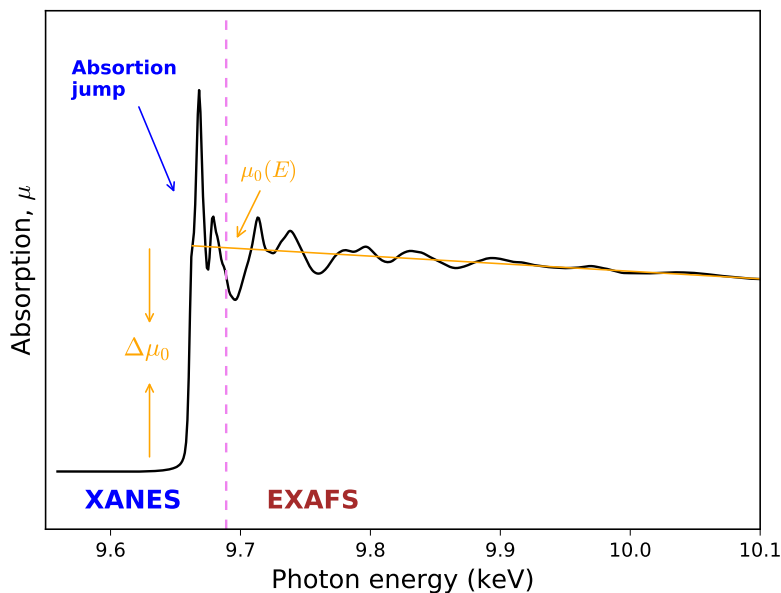


Fig. A.1 XANES and EXAFS regions identified. $\mu(E)$ is shown with smooth background function ($\mu_0(E)$) and the edge-step ($\Delta\mu_0(E_0)$).

A.1.1 Edge Energy - E_0

The edge energy represents the energy required to excite a core electron into an unoccupied state or into the continuum within the sample matrix, creating a photoelectron. The edge energy reference parameter, E_0 , is used to align the experimental spectrum to the theoretically calculated spectrum. A systematic definition of E_0 for all EXAFS spectra from the same adsorption edge is desirable since a shift in E_0 is determined in the fit of theoretical spectra to the experimental spectra. If all data sets have the same E_0 , then all data sets will have the same energy shift. The inflection point, i.e., the maximum in the first derivative of the absorption edge, is generally considered as a systematic choice [6]. Hence, the edge position is typically chosen at the inflection point with the help of the XANES and first derivative XANES (E) spectra [7].

A.1.2 Pre-Edge Subtraction and Determination of Edge Step

Before $\mu_0(E)$ can be determined, the pre-edge—X-ray absorption before the actual absorption edge occurs—has to be subtracted (Fig. A.2). The pre-edge is normally approximated by a modified Victoreen [$\mu_{pre-edge}(\lambda) = C\lambda^3 - D\lambda^4$] and calculated by extrapolation of the pre-edge region in the data. Similarly, a linear or quadratic function

is regressed to the post-edge region (Fig. A.2(a)). These lines are extrapolated to the absorption edge, E_0 , and the difference in absorption between these projected lines at E_0 is called the edge step.

A.1.3 Post-edge Background Removal

The atomic background $\mu_0(E)$ after the absorption edge has to be determined, normally using a cubic spline:

$$\sum_{j=1}^{NTPS} \frac{(\mu x_j - BCK_j)^2}{e^{-WEk_j^2}} \leq SM \quad (\text{A.3})$$

The cubic spline consists of four parameters that define the spline function: SM (smoothing parameters), W (weighting factor) and the start and end energy that determine the number of points [8]. The more data points available, the better the spline will be defined. The background is optimized using several criteria, of which the most important is not to remove any of the oscillating information from our data.

A.1.4 Normalizing $\mu(E)$

Before $\chi(k)$ can be obtained, the total absorption as obtained from experiment has to be normalized per absorber atom. Normalization is done by subtracting a regressed line determined by the pre-edge region from the entire spectra and dividing the measured spectra by the absorption step height at E_0 . The normalized K absorption spectra of ZnO is shown in Fig. A.2(b). The step height determines the amplitude of the EXAFS oscillations and; therefore, it's correlated to the EXAFS parameters such as the amplitude reduction factor (S_0^2), and the coordination number (N). That is, the step height, S_0^2 , and N are all components of one multiplicative amplitude term in the EXAFS equation (Eq. A.5).

A.1.5 Extraction of $\chi(k)$

The extraction of $\chi(k)$ from the experimentally obtained $\mu(E)$ (Fig. A.1) follows several consecutive steps, some that are visualized in Fig. A.2. χ can be obtained once the atomic absorption is known, by calculating the Eq. A.2

The value of the edge energy is used to calculate $k(\text{\AA}^{-1})$ as given by the following equation.

$$k = \sqrt{\frac{2m(E - E_0)}{\hbar^2}} = 0.263\sqrt{(E - E_0)} \quad (\text{A.4})$$

where E_0 is the absorption edge energy and m is the electron mass. The primary quantity for EXAFS is then $\chi(k)$, the oscillations as a function of photo-electron wavenumber, and $\chi(k)$ is often referred to simply as "the EXAFS". $\chi(k)$ is calculated according to Eq. A.4 and is shown in Fig. A.2(c).

Hence, the pre-edge, post-edge, and resulting step height should always be checked before the $\chi(k)$ spectrum is further processed. Normalized XANES spectra can be used in EXAFS analysis to visually check the alignment of the spectra and to look for spectral changes between successive scans from the same sample.

A.1.6 Fourier Transform k -Weights

The amplitude of EXAFS oscillations diminishes with increasing energy above the absorption edge (Fig. A.2(c)). Therefore, EXAFS spectra are usually multiplied by k raised to the power of 1, 2, or 3 before the Fourier transform is performed. This is called k -weighting and results in a plot with more uniform amplitude. By increasing the k weight, the data at higher k are given relatively more importance, and the Fourier transform will have larger amplitude for the Fourier components that have a larger contribution at higher k values as seen in Fig. A.2(d).

A.2 EXAFS Fitting Parameters

All photoelectron scattering configurations that start at the absorber atom, go to one or more neighbouring atoms, and then return to the absorber atom contribute to the EXAFS signal. These configurations are called scattering paths. Single-scattering paths are from one shell of atoms. The degeneracy of a single-scattering path is the coordination number of that shell. The degeneracy of a multiple scattering path is the number of equivalent paths. Once a path has been selected for possible inclusion in a structural model, mathematical expressions for the EXAFS parameters are defined [4, 5].

The EXAFS equation can be written in terms of a sum of the contribution from all scattering paths of the photoelectron [9]:

$$\chi(k) = S_0^2 \sum_i N_i \frac{f_i(k)}{kR_i^2} e^{-2R_i/\lambda(k)} e^{-2k^2\sigma_i^2} \sin(2kR_i + \phi_{ij}(k)) \quad (\text{A.5})$$

$$R_i = R_0 + \Delta R$$

$$k^2 = 2m(E - E_0)/\hbar^2$$

Starting Values:

- R_0 : half-path length from the input configuration

Theoretically calculated values:

- $F_i(k)$: effective scattering amplitude of the backscattering wave from the neighbour of type i
- $\phi_{ij}(k)$: effective scattering phase shift between the central ion j and its neighbours i
- $\lambda(k)$: mean free path of the photoelectron and is a phenomenological term that accounts for inelastic losses

Parameters determined in fit:

- N_i : is the number of neighbours of type i at and average distance R_i
- S_0^2 : passive electron reduction factor, an amplitude reduction term that is due to multi-electronic effects
- σ_i^2 : is the Debye-Waller factor that describes both the static and dynamic (thermal agitation) disorder in a Gaussian distribution approximation
- E_0 : energy shift
- ΔR : change in path length

The parameters that are often determined from a fit to the EXAFS spectrum affect either the amplitude of the EXAFS oscillations (N , S_0^2 , σ^2) or the phase of the oscillations ΔE_0 and ΔR , all of which can be calculated by a computer program such as FEFF [10].

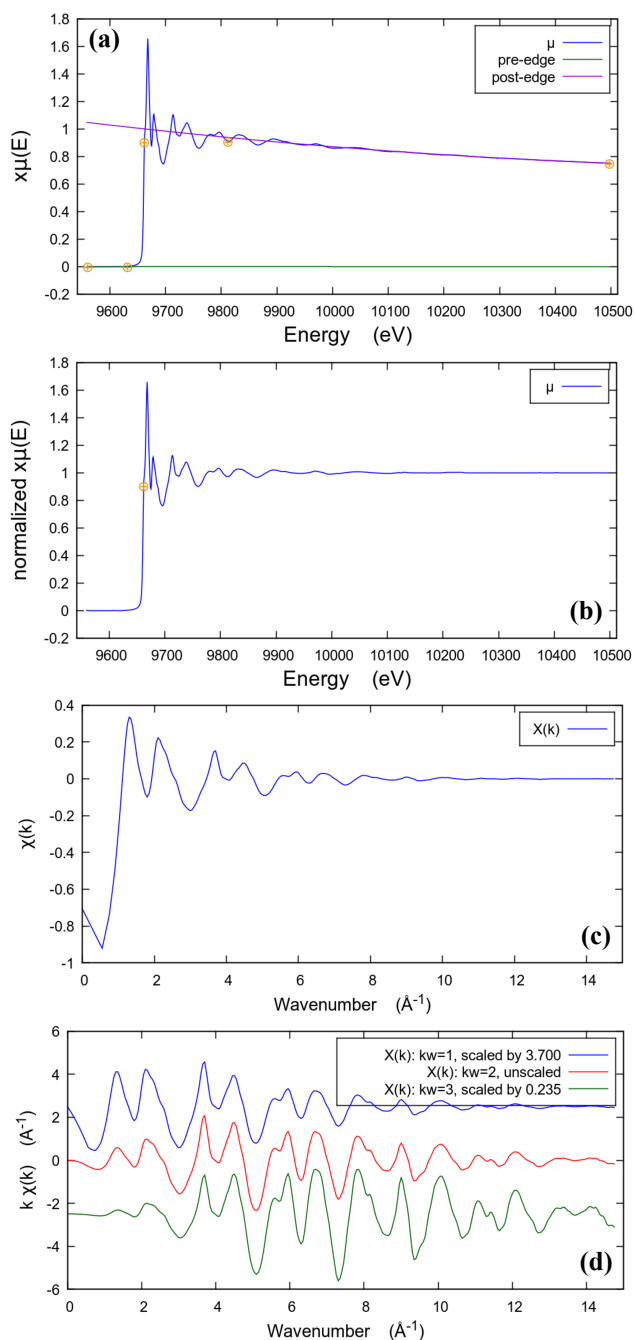


Fig. A.2 The different steps for extraction of the oscillatory part from the K absorption spectrum of powder ZnO recorded at XAFS1 beamline at LNLs, (a) raw X-ray absorption data and pre-edge and post edge lines, (b) normalized X-ray absorption data, (c) $\chi(k)$ vs. k data (k -weight = 0) and, (d) EXAFS $\chi(k)$ vs. k data (k -weight = 1, 2 and 3).

References

1. Matthew Newville. IFEFFIT: interactive XAFS analysis and FEFF fitting. *Journal of synchrotron radiation*, 8(2):322–324, 2001.
2. SI Zabinsky, JJ Rehr, A Ankudinov, RC Albers, and MJ Eller. FEFF code for ab initio calculations of XAFS. *Phys. Rev. B*, 52(4):2995–3009, 1995.
3. M Newville. FEFFIT-Using FEFF to model XAFS data. *Department of Physics, FM-15, University of Washington, Seattle, WA*, 1995.
4. Matthew Newville. Fundamentals of XAFS. *Reviews in Mineralogy and Geochemistry*, 78(1):33–74, 2014.
5. Grant Henderson, Daniel Neuville, and Robert Downs. *Spectroscopic methods in mineralogy and material sciences*, volume 78. Walter de Gruyter GmbH & Co KG, 2014.
6. SD Kelly, D Hesterberg, and B Ravel. *Analysis of soils and minerals using X-ray absorption spectroscopy*, volume 5. Soil Science Society of America: Madison, WI, 2008.
7. Abhijeet Gaur, Basant Deo Shrivastava, and HL Nigam. X-ray absorption fine structure (XAFS) spectroscopy—A review. *Proceedings of the Indian National Science Academy*, 79(Part B):921–966, 2013.
8. DC Koningsberger, BL Mojet, GE Van Dorssen, and DE Ramaker. XAFS spectroscopy; fundamental principles and data analysis. *Top. Catal.*, 10(3-4):143–155, 2000.
9. EA Stern and SM Heald. Basic principles and applications of exafs. *Handbook on synchrotron radiation*, 1:955–1014, 1983.
10. John J Rehr and Robert C Albers. Theoretical approaches to x-ray absorption fine structure. *Reviews of modern physics*, 72(3):621, 2000.

